UCLA

UCLA Electronic Theses and Dissertations

Title

Hazard mitigation and earthquake physics investigation with local array back-projection, tsunami source inversion and rupture simulation

Permalink

https://escholarship.org/uc/item/0dr378v2

Author

Xie, Yuqing

Publication Date

2022

Peer reviewed|Thesis/dissertation

UNIVERSITY OF CALIFORNIA

Los Angeles

Hazard mitigation and earthquake physics
investigation with local array back-projection,
tsunami source inversion and rupture simulation

A dissertation submitted in partial satisfaction
of the requirements for the degree
Doctor of Philosophy in Geophysics & Space Physics

by

Yuqing Xie

2022

ABSTRACT OF THE DISSERTATION

Hazard mitigation and earthquake physics
investigation with local array back-projection,
tsunami source inversion and rupture simulation

by

Yuqing Xie

Doctor of Philosophy in Geophysics & Space Physics

University of California, Los Angeles, 2022

Professor Lingsen Meng, Chair

Investigating the characteristic of earthquake source more accurately and faster is required to mitigate earthquake hazard and improve the understanding of the mechanism of earthquake source. In this work, I develop a new method:multi-array local back-projection (MLBP).

Local back-projection potentially resolve the rupture process of large earthquakes faster and more accurately. Multiple arrays are combined to increase the stability and accuracy of back-projection results.

The method are successfully applied to large earthquakes from M 6 to M 9 using the existing seismic stations in California and Japan. We also propose a tsunami early warning approach based on the muti-array local back-projection method.

The dissertation of Yuqing Xie is approved.

Paul M Davis

Carolina Lithgow-Bertelloni

Gilles Peltzer

Lingsen Meng, Committee Chair

University of California, Los Angeles

2022

To My Family

TABLE OF CONTENTS

LIST OF FIGURES

LIST OF TABLES

ACKNOWLEDGMENTS

Foremost, I would like to express my sincere gratitude to my advisor Prof. Lingsen Meng. He always provides inspring thoughts for solving problems we encountered. He is also very kind and supportive. He gave me a lot of freedom to do things in my style and at my own pace.

Besides my advisor, I would like to thank the rest of my thesis committee: I'm impressed by Prof. Carolina Lithgow-Bertelloni's attitude toward science. I am so surprised when she found an equation from her notes she wrote during her PhD's study in less than 1 minute. She encourages me to accumulate more knowledge, which finally lead toward intuition.

My sincere thanks also goes to Prof. Gilles Peltzer. He gave me a lot of suggestions about my research based on his experience about earthquakes and faults in the real world. The filed trip he lead is interesting and meaningful. The spaghetti he cooked for us is incredible.

I also would like to thank Professor Paul Davis. His optimistic and humorous mood is contagious. His passion for science and the breadth of his knowledge also infected me.

Besides, I want to thank Professor Jean-Paul Ampuero, Professor Kato Naoyuki, Professor Chao An, Professor Huihui Weng, Dr. Hui Huang, Dr. Yindi Luo, and Dr. Tong Zhou. They provide great helps during my study.

I also would like to thank Shuyu Chen, Zheng Xing, Ailin Zhang, Haotian Xu, Tian Feng, Han Bao, Liuwei Xu and Saeed Mohanna. We share a lot of happiness and sorrows in LA. Last but not least, I would thank my parents and grandparents. They always understand me and give me a lot of supports in all aspects.

2011–2013   B.E. (Hydraulic Engineering), Tsinghua University, Beijing, China.

2013–2016   M.A. (Geophysics), Peking University, Beijing, China

2016–present Ph.D. student(Geophysics), UCLA.

PUBLICATIONS

Xie, Y., Kato, N. (2017). Fracture energies at the rupture nucleation points of large strike-slip earthquakes on the Xianshuihe fault, southwestern China. Journal of Asian Earth Sciences, 134, 55-62.

Zhou, T., Meng, L.,**Xie, Y.**, & Han, J. (2019). An Adjoint-State Full-Waveform Tsunami Source Inversion Method and Its Application to the 2014 Chile-Iquique Tsunami Event. Journal of Geophysical Research: Solid Earth, 124(7), 6737-6750.

Xie, Y., & Meng, L. (2020). A multi-array back-projection approach for tsunami warning. Geophysical Research Letters, 47(14), e2019GL085763.

Meng, L., Huang, H., **Xie, Y.**, Bao, H., & Dominguez, L. A. (2019). Nucleation and kinematic rupture of the 2017 Mw 8.2 Tehuantepec earthquake. Geophysical Research Letters, 46(7), 3745-3754.

Xie, Y., Bao, H., & Meng, (2021). Source imaging with a multi-array local back-projection and its application on the 2019 Mw 6.4 and Mw 7.1 Ridgecrest earthquakes, JGR.

Martin Vallée, **Xie, Y.**, Raphael Grandin, Juan Carlos Villegas, Jean-Mathieu Nocquet, Sandro Vaca, Lingsen Meng, Jean Paul Ampuero, Patricia Mothes, Paul Jarrin. Self-reactivated

rupture during the 2019 Mw=8 northern Peru intraslab earthquake. (In review)

Xie, Y., & Meng, L., Zhou, T., Xu L., Bao, H., Chu, R., The 2021 Mw 7.3 East Cape earthquake: Triggered Rupture in Complex Faulting Revealed by Multi-Array Back-projection. (In review)

CHAPTER 1

Introduction

Fast and accurate characterization of earthquake source is important for mitigating earthquake hazard of earthquakes and improving the understanding of the mechanism of earthquake source. The advances in observation studies of large earthquakes, based on space-geodesy (Ozawa et al., 2011; Simons et al., 2011) and waveform inversions (Ide, Baltay, & Beroza, 2011; Wei, Helmberger, & Avouac, 2013) provide source parameters including the source location, focal mechanism, rupture size and slip distribution, which are important for estimating potential disasters and rapid rescue response, as well as revealing numerous underlying earthquake physics.

Over the last two decades, the development of large-scale dense seismic networks, such as USArray, ORFEUS array (European network), China National Seismic Network, and Hi-net (Japanese network) has enabled rapid progresses in many fields in seismology. Array data set has high signal to noise ratio even in high frequency band (about 2 Hz) after stacked due to their similar ray path effect, which enables it to resolve earth structure and the rupture process of large earthquakes in great detail. Various techniques utilizing array data set are developed, including beam-forming method, slant stacking techniques, and frequency-wave number analysis (Rost & Thomas, 2002).

Back-projection is a method based on seismic arrays, which was proposed by Ishii, Shearer, Houston, and Vidale (2005) and become one of the most essential and widely used techniques to resolve rupture processes of large earthquakes (Walker, Ishii, & Shearer, 2005; Y. Xu, Koper, Sufri, Zhu, & Hutko, 2009; D'Amico, Koper, Herrmann, Akinci, & Malagnini,

2010; D. Wang & Mori, 2011; Kiser, Ishii, Langmuir, Shearer, & Hirose, 2011; Ishii et al., 2005; Meng, Inbal, & Ampuero, 2011; Koper, Hutko, & Lay, 2011; Yagi, Nakao, & Kasahara, 2012; Fukahata, Yagi, & Rivera, 2014; D. Wang, Takeuchi, Kawakatsu, & Mori, 2016; Meng, Zhang, & Yagi, 2016; Yin & Denolle, 2019; Meng, Huang, Xie, Bao, & Dominguez, 2019). Back-projection stacks coherent signals recorded by station arrays to measure where the signals come from to locate sub-sources of large earthquakes. Compared to waveform inversion method, back-projections are simpler and more robust, because it does not depend on the prior constraints such as rupture speed, fault geometry etc. Besides, back-projection can resolve the rupture process of earthquake with higher spatial and temporal resolution because its high signal-to-noise ratio in high-frequency band after stacking.

Back-projections are commonly applied to seismic waves recorded at teleseismic distances (30 to 90°) because of their waveform simplicity and high interstation coherence. Stations at local and regional distances can potentially provide a higher spatial resolution because of the higher aperture-to-distance ratio (Meng, Ampuero, Sladen, & Rendon, 2012; Maercklin, Festa, Colombelli, & Zollo, 2012; Roten, Miyake, & Koketsu, 2012; Evangelidis & Kao, 2014; Mesimeri, Zhang, & Pankow, 2021), but are more challenging for array analysis because of multiple phases, low waveform coherence due to reflection and scattering in the crust, as well as the location bias caused by travel-time deviations due to velocity heterogeneities in the shallow crust.

Most of the studies (Table. 1.1) utilizing local array back-projection focus on small-aperture (kilometer-scale) arrays close to the faults (Spudich & Cranswick, 1984; Fletcher, Spudich, & Baker, 2007; Allmann & Shearer, 2007). The arrival time difference at different stations in an array are used to determine the back-azimuth of the sub-sources, which can be used to track the propagation of rupture fronts along fault. Back-projection results with high quality are achieved using these close small-aperture arrays. One reason is that these arrays have relatively high waveform coherence in high frequency band (2 to 25 Hz) because of small interstation distances (0.04 to 3 km). Another reason is that these arrays are close

to the source (5 to 20 km), so the change of source back-azimuths during the earthquake is large compared to the uncertainty (e.g. 137 degree in the application of Spudich and Cranswick (1984)). However, these arrays are designed to target particular fault segments and are only available in a few locations (e.g. Parkfield).

To apply local back-projection (epicentral distance about 2 degree) to the existing distributed stations, more advanced method is needed. Because the waveform coherence is relatively lower due to a larger interstation distance (e.g. about 20 to 30 km for Southern California and Hi-net). Besides, due to a larger epicentral distance, the change of back-azimuth during the earthquake rupture is smaller (about 2 degree for the application of the Ridgecrest earthquake sequence), which is comparable to the uncertainty of the back-azimuth (see section 2.6 for more details). Yang et al. (2020) developed a multi-azimuth back-projection using the dense local seismic networks in Southern California and apply it to the 2019 Ridgecrest earthquake sequence. They use a 3D velocity model to correct for the travel time error. However, such an approach is sensitive to the fine-scale tomography model of southern California (e.g. The California Statewide Three-Dimensional Seismic Velocity model (G. Lin et al., 2010)), which is not readily available in most other regions.

The observation studies of large earthquakes have also facilitated numerous efforts to understand the underlying earthquake physics through earthquake cycle and dynamic simulations, assessing the role of a variety of ingredients, including depth-dependent heterogeneities (Y. Huang, Meng, & Ampuero, 2012; N. Kato & Yoshida, 2011), plastic dissipation and poroelasticity (Ma, 2012; Zhu, Allison, Dunham, & Yang, 2020), subducting seamounts (Duan, 2012; Yu, Liu, Yang, & Ning, 2018) and shallow velocity-strengthening (Kozdon, Dunham, & Nordström, 2012). In the 2019 Ridgecrest earthquake sequence, which occurred on an orthogonal strike-slip fault system, an Mw 7.1 earthquake is triggered 1 day after the first Mw 6.4 earthquake. The largest strike-slip and intraplate earthquake recorded to date, the 2012 off-Sumatra event, also rupture multiple faults on an orthogonal fault system and shows unusual complexity including two delayed dilatational branching. To understand the

Table 1.1: A summary of applications of local arary back-projection for imaging large earthquakes

Author	Earthquake	Epicentral distance (km)	Frequency band (and window)	Array aperture (km)	Station (km)	gap	Component	Change of back-azimuth(°)
Spudich and Cranswick (1984)	M 6.9 Imperial Valley	5.6	25 Hz, 0.6-1.2 s	0.2	0.04		P and S	137
Allmann and Shearer (2007)	M6 Parkfield	10 to 20	2-8 Hz	20	0.2-5		S(North component)	distributed station
Fletcher et al. (2007)	M6 Parkfield	12	0.5-15 Hz, 0.5 s	0.6	0.2		S(Fault parallel component)	100
Honda, Aoi, Sekiguchi, and Fujiwara (2008)	M 8 Tokachi	100	0.02-0.25 Hz,10 s	30	20		3 components	30
Honda and Aoi (2009)	M 6.5 Chuetsu-oki	20	1-20 Hz,1 s	3	0.1		Horizontal(ridial and transverse)	100
Honda et al. (2011)	M9.0 Tohoku	50-500	0.05-0.5 Hz, 10s	100	2		Horizontal(ridial and transverse)	40
Maercklin et al. (2012)	M9.0 Tohoku	100-400	0.05-0.4 Hz, 20s	500	20		P (vertical)	distributed station
Meng, Allen, and Ampuero (2014)	M6 Parkfield	12	0.5-8 Hz, 1 s	0.6	0.2		S	100
Meng et al. (2014)	M7.2 EI Mayor-Cucapah	100	0.2-1 Hz, 10 s	30	3		S	15
Meng et al. (2014)	M9.0 Tohoku	800-1000	0.1-0.25 Hz	300	20		S	15
Yang, Zhu, and Lumley (2020)	M 6.4 and 7.1 Ridgecrest	100-200	0.2-5 Hz, 3 s	50	20		P	2

mechanism of the observed branching behavior and the delayed triggering of the earthquakes, we run earthquake cycle and dynamic simulation to investigate the parameters and the rupture pattern on orthogonal fault system. The simulation helps to understand the physics behind the phenomenon and mitigate potential hazard by predicting possible extreme event on a fault system.

The motivation of my PhD research is to develop a method using local to regional stations to resolve the characteristics of large earthquake timely and accurately. During my PhD, we solve the key problems of local back-projection and build a new method: multi-array local back-projection (MLBP). We show that the MLBP method achieves results with higher resolution in shorter time compared to traditional teleseismic back-projection in our applications. The structure of the dissertation is briefly explained as follows:

In chapter 2 we describe the details of our new local back-projection method (MLBP)((Fig. 1.1)). We will first discuss the theory of local back-projection and the improvements including (1) merging the results of multiple arrays to improve the accuracy, reliability and stability; (2) applying grouping method based on waveform coherence automatically to increase the BP quality of individual arrays; (3) applying an empirical travel time correction when an accurate 3D velocity model is not available. We will discuss how to apply these strategies, evaluate the uncertainty of the result and the automatization of the method. This chapter is incorporated from two manuscripts: Xie, Y., Bao, H., & Meng, L. (2021). Source Imaging with a Multi-Array Local Back-Projection and Its Application to the 2019 Mw 6.4 and Mw 7.1 Ridgecrest Earthquakes. Journal of Geophysical Research: Solid Earth, 126(10), e2020JB021396. Xie, Y., & Meng, L. (2020). A multi-array back-projection approach for tsunami warning. Geophysical Research Letters, 47(14), e2019GL085763. I lead the study and discussion in both papers.

In chapter 3, we construct a tsunami warning system based on the MLBP and apply it to the Mw 8.1 Tokachi and Mw 9.1 Tohoku earthquakes, which takes advantage of the short data collecting time of local arrays. We show the efficiency of this method and the stability
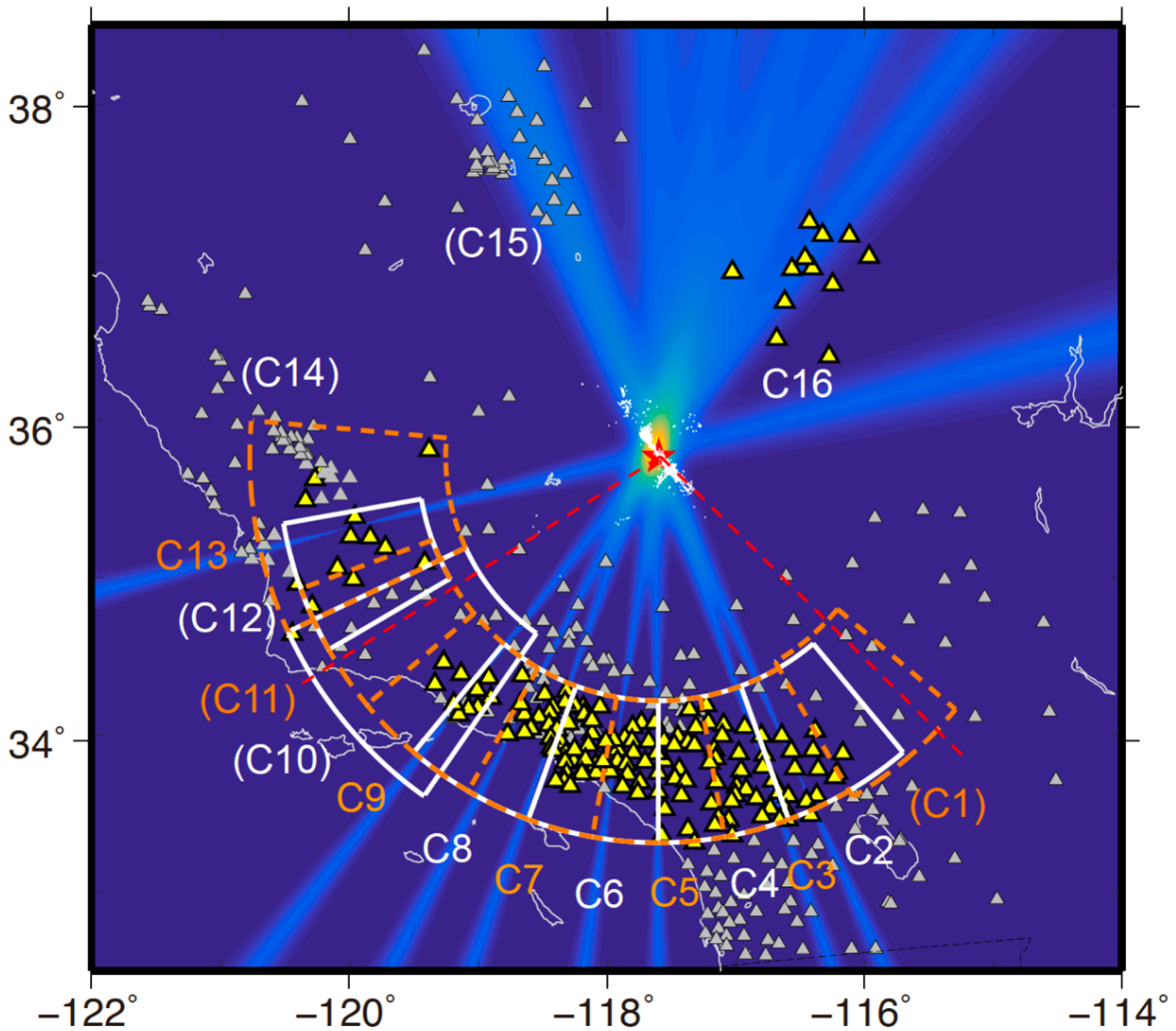
Figure 1.1: Concept, array configuration, and waveform-coherence-based station grouping strategy of the MLBP method (the Mw 7.1 Ridgecrest earthquake). (a) The background color indicates the distribution of joint spatial probability of the source location at the origin time of the Mw 7.1 Ridgecrest earthquake determined with MLBP using C2 - C9, C13, and C16. The red star is the epicenter. The red dashed lines are the nodal planes of the Mw 7.1 event. The orange dashed lines and the white lines delineate the fan-shaped sub-arrays. The grey triangles are the available stations. The yellow triangles are final stations chosen for MLBP. The texts in parenthesis denote sub-arrays that are not used.

of the result in low frequency band. We then discuss the generalization of this method to the major subduction zone. This chapter is modified from "A multi-array back-projection approach for tsunami warning. Geophysical Research Letters, 47(14), e2019GL085763." My contribution is to develop the tsunami approach, conduct back projection and tsunami simulation.

In chapter 4, we show the MLBP results of two smaller earthquakes, the 2019 Mw 6.4 and Mw 7.1 Ridgecrest earthquakes, which require higher resolution and higher frequency band. To increase the objectivity of stations selection criteria and to be prepared for future real-time BP implementations, we apply an automatic procedure to group stations based on waveform coherence. Our MLBP highlights the rupture complexity in a multi-fault system and demonstrates the effectiveness of MLBP for earthquake source imaging of M 6 earthquake, which is useful for rapid hazard assessment. This chapter is modified from "Xie, Y., Bao, H., & Meng, L. (2021). Source Imaging With a Multi-Array Local Back-Projection and Its Application to the 2019 Mw 6.4 and Mw 7.1 Ridgecrest Earthquakes. Journal of Geophysical Research: Solid Earth, 126(10), e2020JB021396. " I am the first author to conduct back projection and write the paper, Han Bao conducted teleseismic back-projection.

In chapter 5, we extend the multiple array method to teleseismic back-projection and apply it to the 2021 Mw 7.3 East Cape, New Zealand earthquake. For individual teleseismic arrays, there is a strong trade-off between depth and horizontal direction. The combination of the BPs of multiple arrays improves both depth and horizontal resolution. Our back-projection results reveal the rupture of multiple faults at different depths, which is linked by static or dynamic stress transfer. This is an collaborative work. I am the first author to conduction 3D back-projection, calculate the static and dynamic stress and write the paper. The manuscript is in review. Tong Zhou contributes the discussion about the delamination. Han Bao and Liuwei Xu provide the preliminary results of the back-projections using individual arrays.

In chapter 6, we demonstrate the results of the earthquake cycle and dynamic simulations

on an orthogonal strike-slip fault system, which is motivated by the complexity of the 2012 Mw 8.6 off-Sumatra earthquake and the 2019 Ridgecrest earthquake sequence. Both earthquakes occur on orthogonal strike-slip fault system and rupture multiple faults, with delayed rupture on dilatational branch. By conducting 3D earthquake cycle and dynamic rupture simulations, we explore the mechanism of the delayed rupture and the rupture pattern on the orthogonal strike-slip fault system. This is an independent work by myself. The manuscript is in preparation. We will collaborate with Huihui Weng, Yindi Luo and Jean-Paul Ampuero in the paper.

In chapter 7, we present another tsunami early warning approach, which is based on tsunami recordings and is potential to be more accuate than the methods based on seismic recordings. We apply the adjoint-state full waveform tsunami inversion method to the S-net stations and build a workflow for tsunami early warning. We show that this method is as fast as the tsunami warning approach based on MLBP method for earthquake in Japan, but is more accurate since it is an inversion method based on tsunami recordings without the assumptions used in the MLBP-based method (such as scaling law). This method is complementary to other methods when a dense array of near-field stations as S-net is available. This is a collaborative work of Saeed Yahya Mohanna, Tong Zhou and me. The manuscript is in preparation. I am the first author to conduct most of the calculations and write the major part of the paper. Saeed's main contribution is the writing of the introduction and discussion. Tong Zhou mainly provided the idea about inverting the coseismic deformation iteratively.

CHAPTER 2

MLBP method

Abstract

In this chapter, we first discuss the challenges of local back-projection and how MLBP method solves these problems. Then we discuss the details of the MLBP method. We will introduce the theory of the MLBP method, the grouping method, the data and parameter selection, and the calibration and evaluation of the result. Finally, we will discuss how to determine the termination of an earthquake, which is useful for automatic application of the MLBP method.

This chapter is modified from the method part and supplemental materials of the following two papers:

Xie, Y., Bao, H., & Meng, L. (2021). Source Imaging with a Multi-Array Local Back-Projection and Its Application to the 2019 Mw 6.4 and Mw 7.1 Ridgecrest Earthquakes. Journal of Geophysical Research: Solid Earth, 126(10), e2020JB021396.

Xie, Y., & Meng, L. (2020). A multi-array back-projection approach for tsunami warning. Geophysical Research Letters, 47(14), e2019GL085763.

I am the first author of the two papers to perform the local back-projection, write the papers.

2.1 Introduction

Back-projections using local array potentially have higher resolution and need shorter data collection time but are more challenging for array analysis mainly because of low waveform coherence due to simultaneous arrival of multiple phases, wave reflections and scattering in the crust. These problems are potentially to be solved by merging the BP results of multiple arrays and only using the data with relatively high waveform coherence.

Another challenge for local back-projection is the location bias caused by travel-time deviations due to velocity heterogeneities in the shallow crust. For traditional teleseismic BP, the bias is caused by the error of the travel time predicted by a 1D velocity model. For local back projection, the bias is mainly caused by the deviation of the raypath between the sources and the array from the great circle due to lateral heterogeneities of wave speeds. Therefore, travel time calibration is important for accurate local BP imaging. One straightforward method is using predicted travel time by high resolution 3D velocity model. Yang et al. (2020) performed a multi-azimuth back-projection using a 3D velocity model with distributed stations to image the Ridgecrest earthquake sequence. However, such an approach is sensitive to the fine-scale tomography model of southern California (e.g. The California Statewide Three-Dimensional Seismic Velocity model (G. Lin et al., 2010)), which is not readily available in most other regions.

Our aim is to explore the potential of using the existing distributed station to resolve large earthquake in local distance (about 2° away). We develop a method, MLBP, which effectively solve the problems of local back-projection and resolve earthquakes from Mw 6.4 to 9.1 accurately by applying the following strategies: (1) Merging the results of multiple arrays to improve the accuracy, reliability and stability. Compared with single-array BPs, multi-array BPs enable higher spatiotemporal resolution and reduce false alarms in earthquake detection and location problems (Fan, de Groot-Hedlin, Hedlin, & Ma, 2018). The multi-array approach also improves stability of the BPs at local distance because BPs of

10

individual arrays may suffer great uncertainties due to crustal heterogeneities and simultaneous arrivals of multiple phases. (2) Improved grouping strategies. We propose and run tests for multiple grouping methods including K-means clustering, non-overlapping rectangular clustering with uniform interval, overlapping circular clustering with uniform interval, and fan-shape clustering with uniform azimuthal interval. We discuss the most suitable condition for different these methods. We also test different sizes of the arrays. We estimate uncertainties of each test. The conclusion from the tests can help us to choose the best grouping method thus achieve more stable and accurate BP result. We also check the mutual coherence of waveforms to search for the best combination of station and remove the incoherence stations. (3) Applying the empirical travel time correction to remove travel time error caused by the horizontal velocity variation. To reduce the travel time errors, we apply a static correction of the resolved back-azimuth. The correction ranges from -5 to 10° so that the first radiator is located at the epicenter. We validate that this correction is applicable to the whole source region by examining the deviations of the MLBP-measured back-azimuths from the reference values of aftershocks from the relocated catalog. (4) Check and mitigate the impact of the simultaneous arrivals of multiple phases. For local arrays with an epicentral distance of about 2 degree, different phases arrivals very closely, which contaminate the waveforms. But different phases separate clearly in the slowness domain. By carefully checking the slowness diagram, we can choose the waveforms corresponding to the phases that last the longest as the input for back-projection and synchronize the arrivals at different sub-arrays. We will discuss these points in the later sections and show more details in the examples in later chapters.

2.2   Theory of MLBP

The MLBP method determines the centroid locations of strong seismic radiations by analyzing the P or S-wave trains recorded by multiple local clusters of stations. Based on

the principles of array back-projection (BP), we propose an algorithm to locate the sub-sources by intersecting back-azimuths of multiple arrays. First the source back-azimuths with respect to each cluster are calculated assuming plane wave arrivals. For a selected time window, we determine the source slowness vector using a correlation stacking approach. This method beamforms the cross-correlation coefficients of all station pairs to improve the robustness against scattering, multipathing and contamination of coda waves (Frankel, 1991; Borcea, Papanicolaou, Tsogka, & Berryman, 2002; Fletcher, Spudich, & Baker, 2006; Meng et al., 2014). The coherence function C_m for the m-th cluster and time t_0 is defined as:

$$C_m(t_0, \theta) = \sum_{i,j} \text{cc}_{ij}(t_0, \theta) = \sum_{i,j} \left(\frac{\sum_{t=t_0-t_1/2}^{t=t_0+t_1/2} x_i(t - \tau_i(\theta)) x_j(t - \tau_j(\theta))}{\sqrt{\sum_{t=t_0-t_1/2}^{t=t_0+t_1/2} x_i(t)^2 x_j(t)^2}} \right), \qquad (2.1)$$

where i and j are the station indices. cc_{ij} is the correlation coefficient between two stations. x_i is the seismogram. t_0 is the time after the origin time. $\tau_i(\theta)$ is the time delay compared to a reference station assuming the slowness vector is θ. The sums in the equations are computed in a running time window of length t_1 centered at t_0. We perform a grid search of the slowness vector and identify the back-azimuth corresponding to the peak stacked coherence.

The second step is to locate the seismic radiators by intersecting the back-azimuths in the source area (Fig. 1.1). For each cluster, the possible source locations are along a vector pointing from the center of the cluster towards the back-azimuth. We apply a Gaussian smoothing to this source location vector accounting for the uncertainty of the back-azimuths. The joint spatial probability distribution of the source location determined with multiple arrays is given by:

$$p(i, j, t) = \sum_{k=1}^{n} exp \left(\frac{\theta_{t_k}(i, j) - \theta_{m_k}(t + t_{0_k})^2}{2\sigma_k} \right), \qquad (2.2)$$

where i and j are the grid indices and k is the cluster index. t is the time after the origin time. p is the probability of the existence of a seismic radiator. n is the number of clusters.

σ_k is the Gaussian smoothing factor, which can be estimated from the uncertainties of the back-azimuths. In the application of the Mw 8.1 Tokachi and the Mw 9.1 Tohoku earthquake, the waveforms of the mainshock and aftershocks are filtered to about 0.06 Hz. The value of σ_k is estimated to be $10°$ after examining the bias of the back-azimuths of 87 M 5-6 relocated reference earthquakes, which corresponds to location errors on the order of 20 km. In the application of the Ridgecrest earthquake sequence, the value of σ_k is estimated to be $2°$ from 14 relocated aftershocks (M 4 to 5.5) when the frequency is around 1 Hz. θ_{t_k} and θ_{m_k} are the theoretical and measured back-azimuths, respectively. t_{0_k} is the arrival time of dominating phase that are used for back-projection at the reference station of the k-th cluster. In the application of the Mw 8.1 Tokachi and the Mw 9.1 Tohoku earthquakes, we use the theoretical arrivals of S-wave at the reference station based on the PREM model [Dziewonski and Anderson, 1981]. For the Ridgecrest earthquakes, we use a higher frequency band, so multiple phases separate clearly in the slowness domain, which allows us to measure the arrival times accurately by hand picking the arrivals(see later chapters for more details). The source grid with the highest probability is considered as the location of the radiator at a time step.

2.3 Cluster grouping strategies

To group station clusters, we need to choose suitable grouping algorithm, size, shape and the number of clusters, which needs to balance (1) the coverage of the back-azimuths, (2) the waveform coherence, (3) the resolution of the back-projection, (4) the satisfaction of the plane wave assumption. Generally, an array with larger size has higher resolution and stability for BP imaging but affects plane wave assumption and has lower coherence (Xie & Meng, 2020).

In the applications of the Mw 8.1 2003 Tokachi and the Mw 9.0 2011 Tohoku earthquakes, we test different station grouping methods, including K-means clustering, non-overlapping
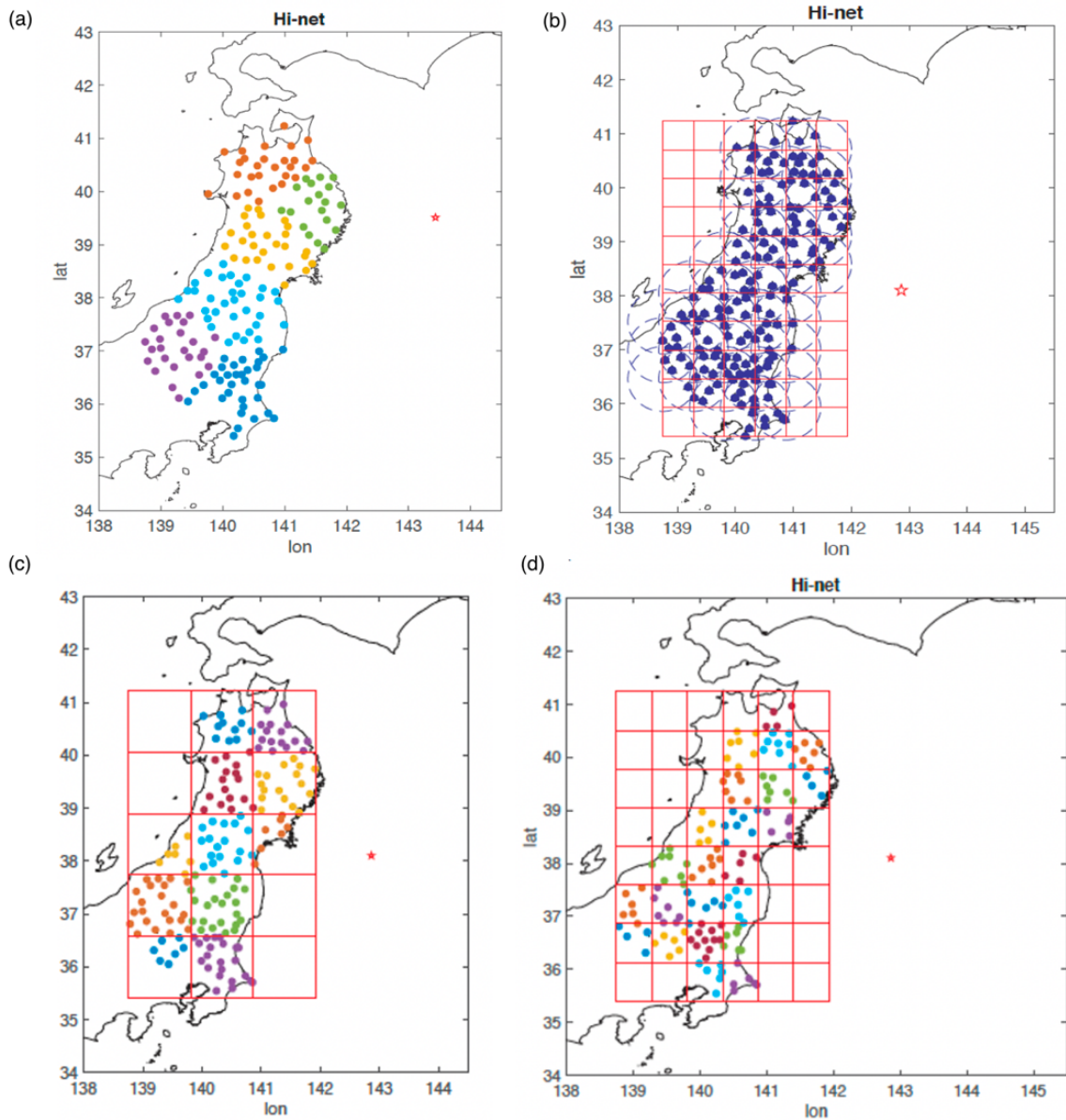
Figure 2.1: Examples of grouping algorithm. (a) is K-means clustering result when assigned 6 clusters. (b) is overlapping circular cluster with an interval of 50 km and a radius of 60 km. (c) and (d) are uniform grid clustering with grid size of 100 km and 80 km respectively.

rectangular clustering with uniform interval, overlapping circular clustering with uniform interval (Fig. 2.1). The frequency we use is relatively low (about 0.06 Hz) because we aimed to resolve the tsunami source, which is more related to low frequency signals. The waveform coherence increases with the decreasing of frequency band. So the stability of the BP result is high and all of these tests produce close results for the mainshock. But by checking the BP results of relocated aftershocks, we can evaluate the accuracy and uncertainty of the different grouping methods and parameters quantitatively.

We run systematic tests to determine the optimal array configuration and size. We test how accurately different grouping strategies locate small earthquakes compared with their catalog locations (Fig. 2.2, Table 2.1).

For a single array, our conclusion is that with the decreasing of cluster size, the accuracy of BP result of each array decreases, but the accuracy of epicenter location increases slightly due to the increasing of the number of clusters. The plane wave assumption becomes invalid when the array aperture exceeds 1.6 degrees when epicentral distance is about 2 to 3.5 °. The performance of a single array is not sensitive to the number of stations within one array (although a minimum of 5 to 8 is needed to get stable result).

For the combined result of multipel arrays, we found a large number of small clusters have good performance. The results of the combined BP become very stable when the number of clusters is large enough (about 30) regardless of the grouping methods and sizes of cluster (about 0.5-1.2 degree). So for the tsunami warning system for the subduction zone of Japan, we propose to use a uniform grid clustering method with a grid size of 70 km, with 5 to 7 stations in one cluster. This choice maximizes the number of clusters thus increase the accuracy of BP. This choice is most suitable for the cases when the waveform coherence is high so that the BP results of each arary are stable with only 5 to 7 stations.

For other regions, if the station density is low (when the station spacing is about 50 km), to ensure the number of clusters, we have to use overlapping clusters. In these cases, one station may belong to multiple arrays. More details about these tests are in the later

sections and the supplement material of Xie and Meng (2020).

In the applications of the 2021 Mw 6.4 and 7.1 Ridgecrest earthquakes, to maintain good azimuth coverage and adequate plane-wave assumptions, we group all potential stations into about 16 fan-shaped sub-arrays (Fig. 1.1, Fig. 2.3), each covering an azimuthal range of 20° with an interval of 10°. This grouping algorithm ensures stable and accurate result for high frequency bands (about 1 Hz). More details about the selection of the size of arrays are discussed in Xie, Bao, and Meng (2021).

2.4 Data and parameter selection

2.4.1 Waveform coherence and frequency band

Waveform coherence is important for back-projection. High waveform coherence means high accuracy and stability for back-projection. Waveform coherence increases with the decreasing of frequency bands and interstation distance. We also found waveform coherence correlates with topography, source radiation pattern and Vs30 (Fig. 2.3). We can remove incoherence stations within each array to increase the waveform coherence thus the quality of BP.

The selection of the frequency bands needs to balance the robustness and the imaging resolution of BPs. For local back-projection, the waveform coherence is lower compared to the teleseismic wave when the frequency band and station density is the same due to simultaneous arrivals of multiple phases at local stations. For a single subarray, lower-frequency waveforms are naturally more coherent, which produce stable BPs but provide lower resolution.

So we determine the frequency bands mainly based on the purpose of the back-projection and the station density. It has been widely recognized that seismic data with high frequency are more efficiently generated by the abrupt change in rupture speed, rather than by total
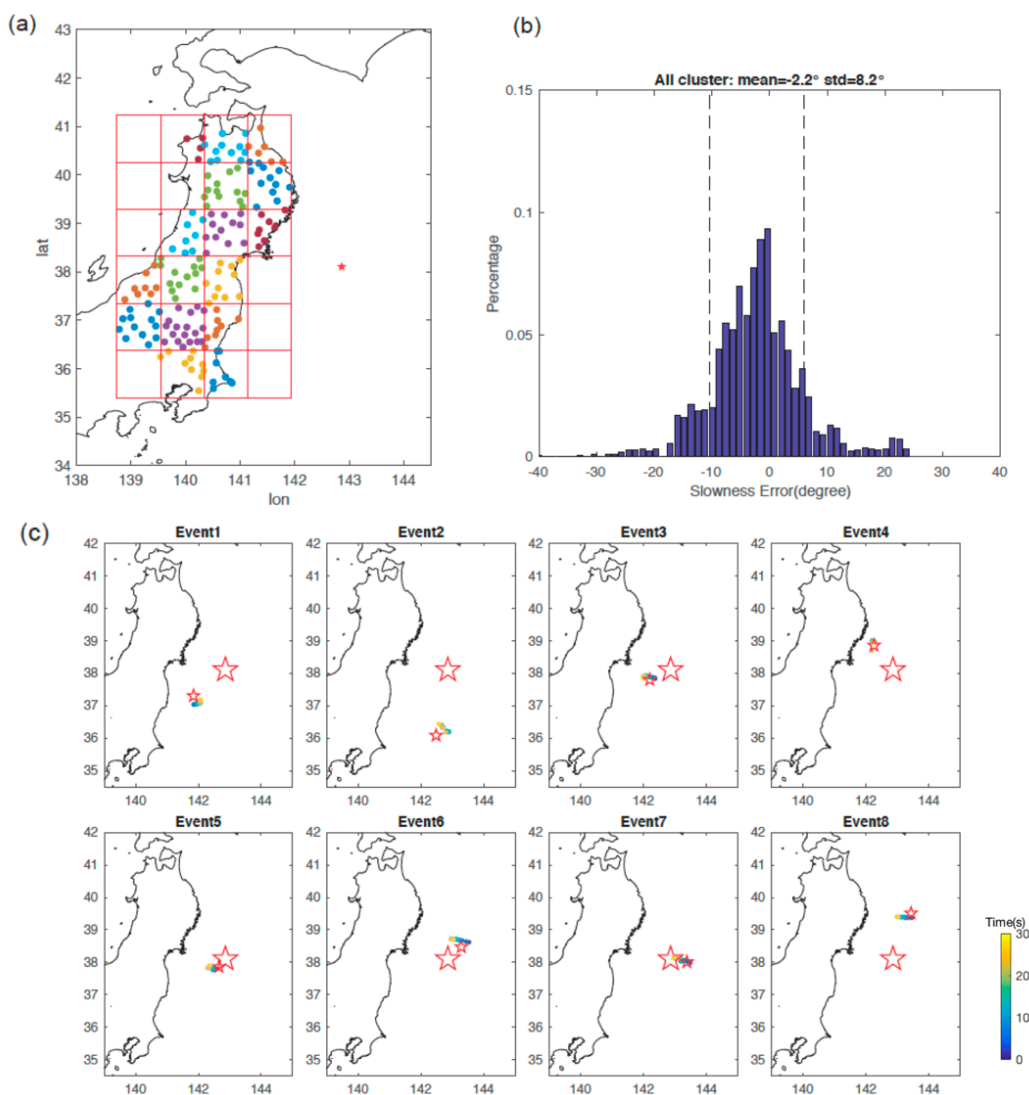
Figure 2.2: An example of the uncertainty analysis of the back-azimuth and earthquake location (test A4, with 16 clusters with uniform size (0.9 degrees) and interval). (a) The map of the distribution of stations (colored circles) on each cluster (circles in the same color). (b) The bias distribution of the measured back-azimuths in the first 30 seconds of 8 reference earthquakes. The dashed lines are 3 times of the standard deviation. (c) Earthquake location bias after combining the BPs of 16 clusters. The circles are back-projection radiators color-coded by time and sized by normalized power. The larger stars show the epicenter for the Tohoku earthquake and the smaller stars are the epicenters of the reference earthquakes.

17

large slip (e.g. Madariaga, 1983). In standard teleseismic BP, the seismograms are filtered at high-frequencies (1 Hz) to achieve the kinematic process of large earthquakes with high spatial and temporal resolutions. For imaging the rupture process of the Mw 6.4 Ridgecrest earthquake, which requires higher spatial and temperal resolution, we choose the highest frequency bands that ensure high enough waveform coherence and yield stable and concentrated BP peaks in slowness diagrams of each sub-array (about 1 Hz). When analyzing the static slip and tsunami generations, we use low frequency band (about 0.06 Hz).

2.4.2   Selection of seismic phases and components

We utilize the S phase for large earthquakes (the Mw 8.1 Tokachi earthquake and the Mw 9.1 Tohoku earthquake) because the S-P time (about 40 s at a station 3.5° away from the epicenter) is shorter than the duration of a Mw 9.1 earthquake (about 300 s). If we use P wave, the waveforms after 40 s will be contaminated by the S wave. We adopt the transverse component to enhance the signal of the S wave.

For the smaller earthquakes (the Mw 6.4 and the Mw 7.1 Ridgecrest earthquake sequence), we use the vertical component of the P phase because the duration is shorter. So the P wave train does not mix with S phases. We use higher frequency bands (about 1 Hz) to increase the spacial resolution, so the challenge is the complicates caused by multiple reflected P phases that have close arrival times (Fig. 2.4). These phases can be treated as one phase after filtered to low frequency bands, but not for high frequency bands. For the phases that are close in time and slowness domain, we have to treat them as a whole, although this brings some uncertainties and bias. If two phases (or two groups of phases) seperate clearly in time and slowness domian, we can choose the dorminating phase for back-projection. If both of the two phases have high quality (Fig. 2.5), we can conduct back-projections for them seperately, then combined the BPs to increase constraints. For the Ridgecrest earthquake sequence, we utilize the dominant P phases at the epicentral distance of 2° (about 222 km), which are a group of crustal phases, composed of PmP, Pg, PConradP and Pb (Fig. 2.4)
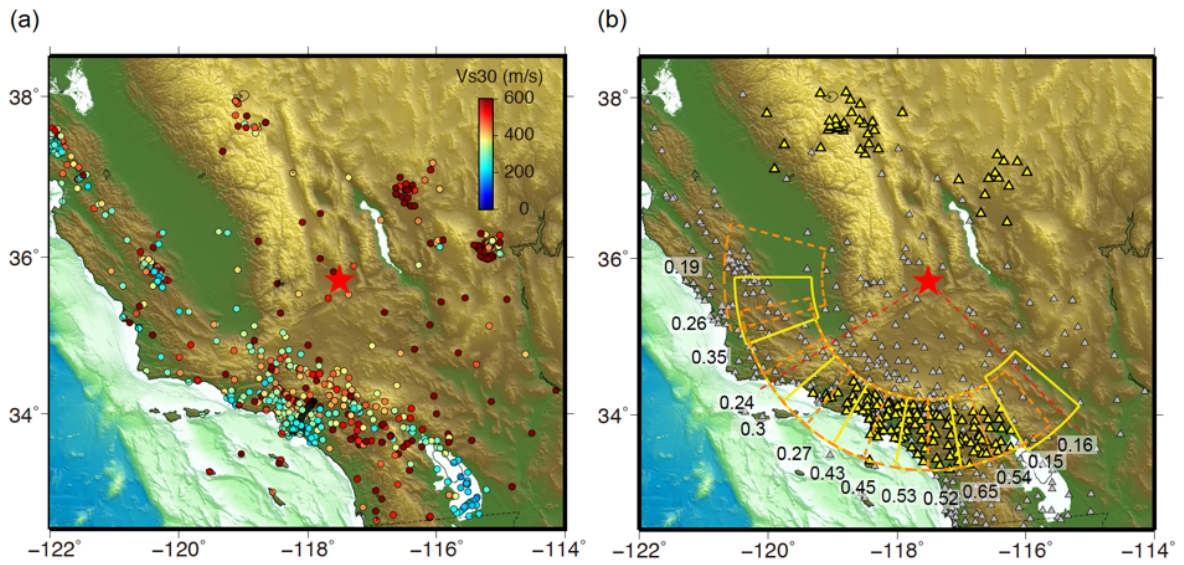
Figure 2.3: (a) Vs30 distribution. The colored dots are Vs30 at each site of the stations according to the USGS database (Yong et al., 2016). Dark red color denotes stations with Vs30 >= 600 m/s. (b) The array configuration of the MLBP of the Mw 6.4 event. The numbers show the average cross-correlation coefficients of all available stations within each sub-array.

Table 2.1: Errors of earthquake locations and back-azimuths for different station grouping methods estimated using 8 reference earthquakes.

Test	Uncertainty of back-azimuth (°)	Bias of earthquake location (km)	Cluster number	Avarage station number in one cluster	Cluster size (°)	Bias of back-azimuth within 1 std
Test A1 (Kmean)	6.6	32.3	6	28.7	1.2-1.5	3.5 to 9.7
Test A2 (Kmean)	6.2	24.9	8	21.5	1.1-1.4	-8.1 to 4.3
Test A3 (uniform grid)	6.2	23.9	11	15	1.06-1.16	-9 to 3.4
Test A4 (uniform grid)	8.2	24.3	16	10.2	0.80-0.97	6 to 10.4
Test A5 (uniform grid)	7.5	24.1	18	8.4	0.64-0.83	-10 to 5
Test A6 (uniform grid)	9.7	22.7	23	6.2	0.53-0.73	-11.8 to 7.6
Test A7 (overlapping circle)	6.4	21.5	38	16.25	1.2	3.8 to 9
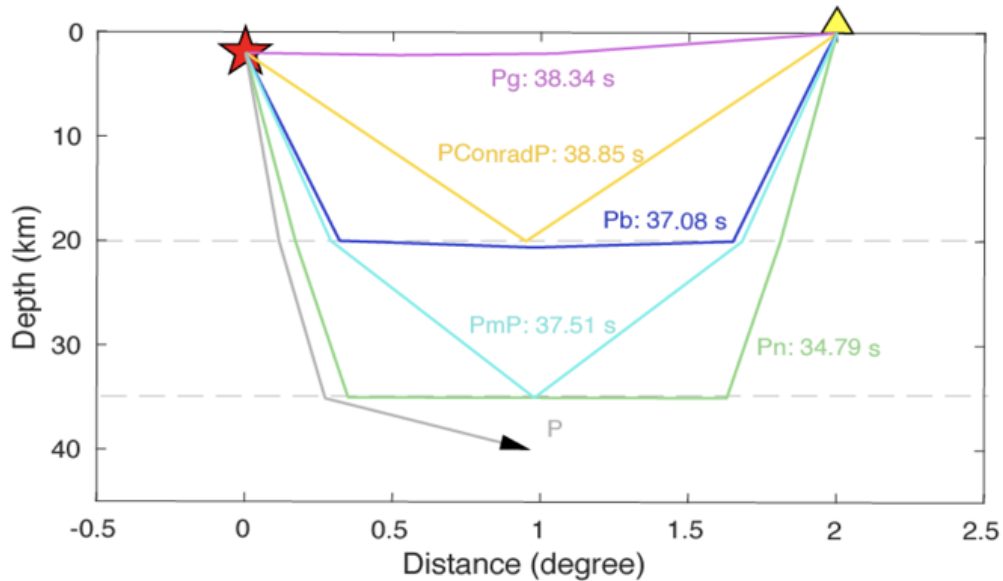
Figure 2.4: The ray paths and arrival times for different phases predicted using the IASP91 model (Kennett & Engdahl, 1991) assuming a source at 2 km and a station at 2° away.

with an apparent slowness of about 0.15 s/km (Fig. 2.6). These dominant phases are not always the first arrivals. In the northern sub-arrays, the first resolved radiators correspond to a group of crustal phases and we pick the first robust radiator around the theoretical arrival time to synchronize these sub-ararys with other sub-arrays. For the sub-arrays to the southwest, the radiators associated with crustal phases are overtaken by the radiators associated with mantle phases for several seconds possibly due to variations of 3D velocity structure or different BP resolvability. These two groups of phases are separated clearly in apparent slowness (about 0.12 s/km for the mantle phase and about 0.15 s/km for the crustal phases) (Fig. 2.6). In this case, we pick the first robust radiator in the second group of slowness peaks corresponding to the crustal phases to synchronize different sub-arrays.

2.5   Aftershocks calibration, uncertainty and resolution

To reduce the travel time errors due to 3-D velocity structures, we apply a static correction of the back-azimuth ranging from -5 to 10° so that the first radiator is located at the epicenter. We validate that this correction is applicable to the whole source region by examining the deviations of the MLBP-measured back-azimuths from the reference values of 14 aftershocks (M 4 to 5.5) of the Mw 7.1 event (Fig. 2.7) from the relocated catalog (H. Huang et al., 2020). We use the same array configuration for the Mw 7.1 earthquake to calculate BPs for each aftershock using a frequency band of 0.08 to 0.8 Hz and a window of 10 s. If we use the same frequency bands as the Mw 7.1 earthquake, the signal to noise ratio and the coherence will be too low to get concentrated BPs. So we use a slightly lower frequency band for the aftershocks. For each aftershock, we measure the back azimuths of the waveforms in the 10 s sliding windows with an interval of 0.5 s starting from the P arrivals. In Fig. 2.7(d), we show that the biases are not dependent on the location on the fault. So we apply a uniform correction along the strike of faults.

The resolution of the back-projection of a single array can be estimated using Rayleigh

21
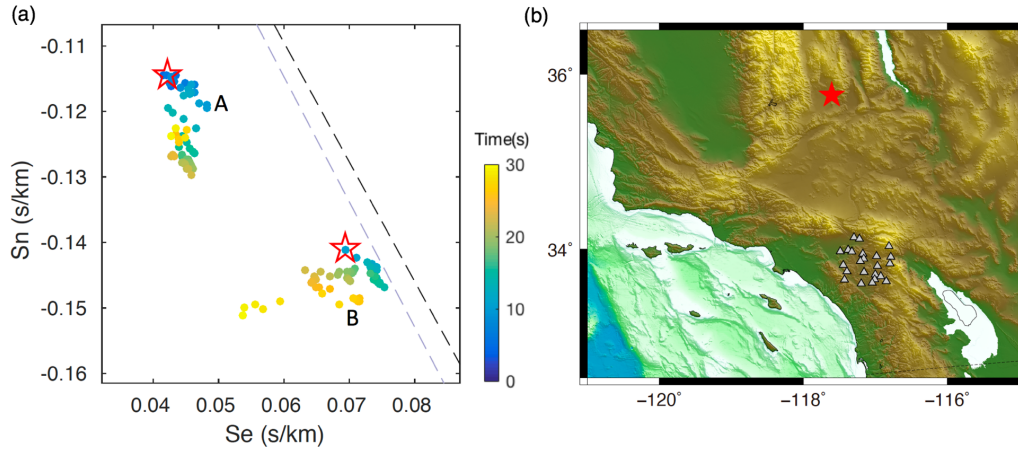
Figure 2.5: An example of two groups of phases that overlap in time but seperate clearly in slowness domain. (a) The BPs of the Mw 7.1 Ridgecrest earthquake in the first 30 seconds resolved by a sub-array (shown in (b)). The color of dots are coded by the time (relative to 10 s before the theoretical arrivals of the first P waves. The abscissa and ordinate are slownesses in the east-west and north-south directions, respectively. The star shows the manually picked arrival times of the two groups of phases, which can be used to synchronize with BPs of other phases and subararys. The black and grey dashed line are the theoretical source back-azimuth predicted from the relocated catalogue of the Mw 6.4 and Mw 7.1 Ridgecrest earthquakes (H. Huang, Meng, Bürgmann, Wang, & Wang, 2020).
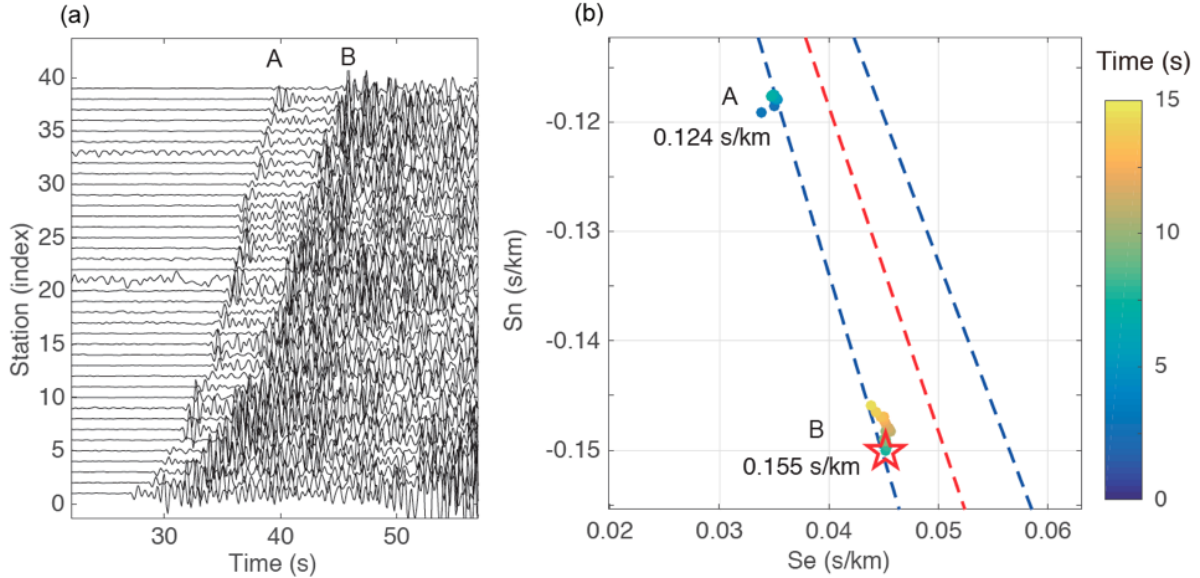
Figure 2.6: An example of waveforms and slowness showing the mantle phase group (A) and crustal phase group (B). (a) Waveforms of stations in C3 for an M 4.52 aftershock (Origin time: 2019-07-07 05:38:16; location: 35.77° N 117.58° W). The zero time marking the earthquake origin time. (b) The BPs of the aftershock in the first 20 seconds resolved by C3. The color of dots are coded by the time (relative to 10 s before the theoretical arrivals of the first P waves. We start to calculate the back-azimuths of individual sub-arrays 10 s earlier to avoid missing the initial P phase, considering the uncertainties of the theoretical arrival times). The abscissa and ordinate are slownesses in the east-west and north-south directions, respectively. The star shows the manually picked arrival time of the dominating crustal phases. The red dashed line is the theoretical source back-azimuth predicted from the relocated catalogue (H. Huang et al., 2020). The blue dashed lines show a deviation range of 2° from the theoretical source back-azimuth.
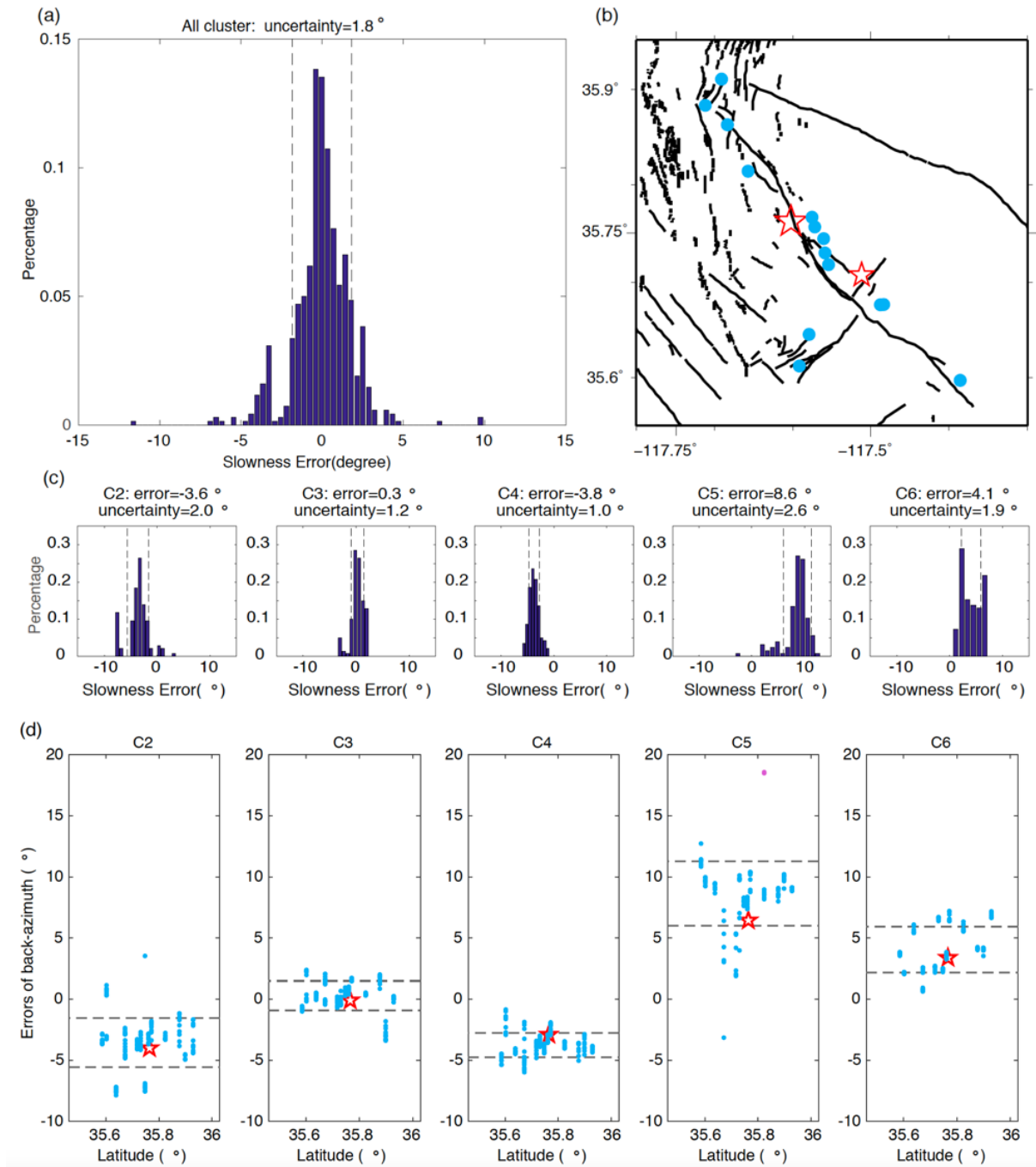
Figure 2.7: (Caption next page.)

(Caption of Fig. 2.7)The errors, uncertainties and biases of back-azimuth measurements of 5 sub-arrays of the Mw 7.1 earthquake estimated from 14 aftershocks of M 4 to 5.5. The error is defined as the difference between the MLBP-measured and reference back-azimuths calculated from the relocated catalog (H. Huang et al., 2020). The bias is defined as the mean of the error. The uncertainty is defined as the standard deviation of errors after removing the bias. (a) The distribution of the remaining errors of the back-azimuths for the 5 sub-arrays after removing the bias for each sub-array. The dashed lines show the standard deviation, 1.8°. (b) Locations of the aftershocks used for this analysis. The locations of the Mw 7.1 and Mw 6.4 earthquakes are shown by the red stars. (c) The distribution of the errors of back-azimuths at each sub-array. (d) The errors of the back-azimuths at each sub-array for each aftershock. The circles are back-azimuth biases for all measurements at all time steps for all aftershocks. The dashed lines show the standard deviation of the errors for each sub-array. The red stars show the errors of back-azimuth of the first radiators of the Mw 7.1 earthquake.

Criteria (Lipson, Lipson, & Lipson, 2010):

$$L \approx 1.22\frac{\Delta \cdot \lambda}{A}, \tag{2.3}$$

where L is the resolution limit in the azimuthal direction on the fault for an array, Δ is the distance away from the source, A is the aperture of the array, λ is the horizontal wavelength.

So theoretically, the resolution of a single array is related to frequency band, epicentral distance, and the aperture of an array. We can use the BP analysis of aftershocks to estimate the uncertainty of the BPs of mainshocks. For the Ridgecrest earthquakes, Fig. 2.7 shows that after removing the systematic bias (the static calibration), the standard deviation of errors of back-azimuths is about 1.8 °. When the resolution is projected along fault strike, we need also consider the angle between the fault strike and the azimuth of sub-arrays. We take the cases in Fig. 2.8 as an example. When the raypath is perpendicular with the fault strike direction (Fig. 2.8(a)), given that the uncertainty of the back-azimuth ($\angle$FSA) is 2°,

the uncertainty of the location along the fault strike (FA) is 7.7 km. When the ray path has a smaller angle with the fault strike direction (e.g. 45 °), as (Fig. 2.8(b)) shown, we can get FA = 11. 4 km using the law of sines. So the uncertainty of the back-azimuth of 2 ° transfers to approximately 7.7 to 11.4 km of along-strike distance error for sub-arrays oriented 45 to 90 ° from the fault strike direction of the Mw 7.1 earthquake, which is small compared to the 40 km length scale of the Mw 7.1 mainshock.

2.6   The termination of an earthquake

MLBP is performed from t=0 s until the termination of the earthquakes determined based on the degree of spatial scattering of the radiators (Fig. 2.9). During the earthquake the radiators stay focused, but towards the end of the earthquake, the radiators become scattered due to incoherent coda waves. We evaluate the degree of scattering using the root-mean-square variant of the radiators from t=0 s to each time step. An earthquake is considered to end when the spatial variance of the radiators exceeds a threshold, which is based on the scaling law between magnitudes and rupture lengths (Wells & Coppersmith, 1994). We estimate the thresholds of scattering of radiators for different magnitudes assuming a bilateral rupture propagation along a hypothetical fault line (Fig. 2.9(a)). The standard deviation of linearly distributed radiators is the same for unilateral and bilateral rupture and is larger than other scenarios including L-shape faults. This method is applied to the Ridgecrest earthquake sequence and the results (Fig. 2.9(b) and (c)) are roughly consistent with manually picked rupture termination times.
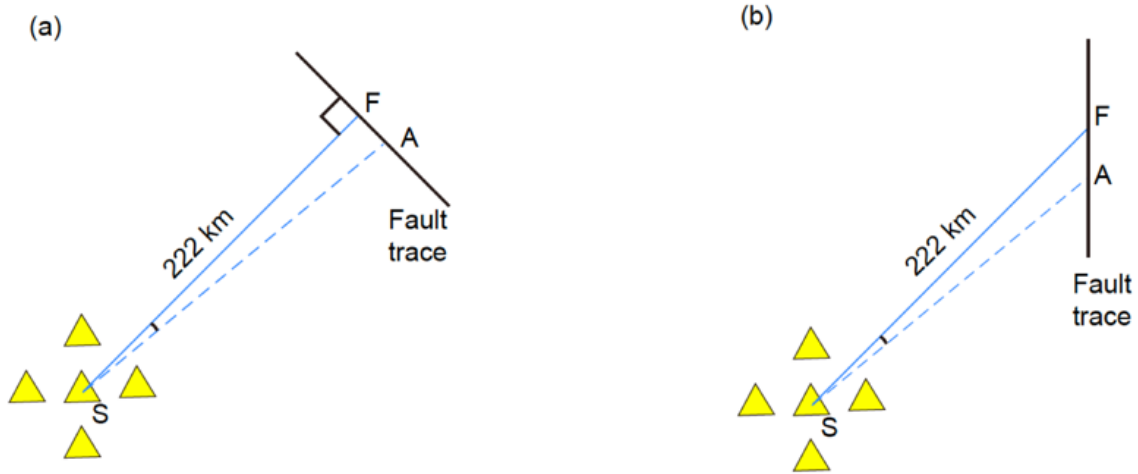
Figure 2.8: The cartoon for estimating the uncertainty of back-azimuths projected to the source region. The yellow triangles are stations in a sub-array with the station in the center as the reference station. The blue line (FS) is the ray path projected to the surface. The dashed blue line (SA) is rotated clockwise by 2 degrees. The angle between FS and AS is corresponding to the uncertainty of the back-azimuth. The black line is the fault trace, which has an angle of 90 degree in (a) and 45 degree in (b) with the ray direction FS.

27
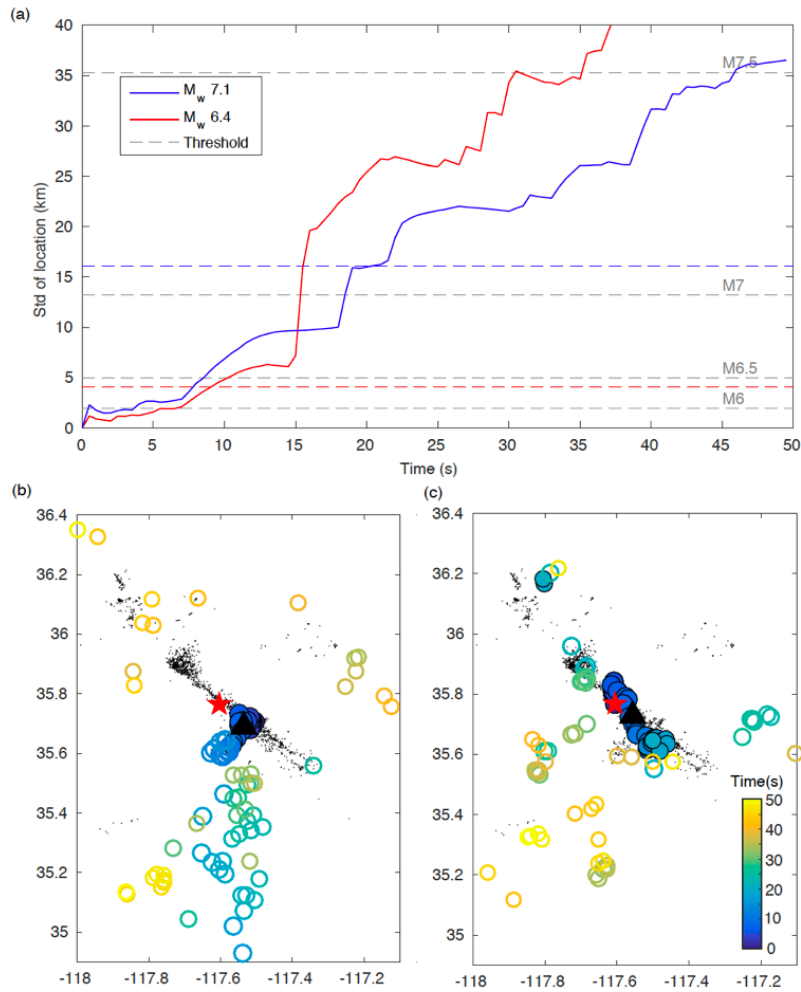
Figure 2.9: The automatic estimation of the terminal time of earthquakes. (a) The history of the variance of the continuous radiators' location from 0 s to each time step. The grey dashed lines are the thresholds for different magnitudes, which are estimated by considering the maximum separations according to the scaling law between rupture length and magnitude assuming linear rupture propagations (Wells & Coppersmith, 1994). The red and blue dashed lines are corresponding to the thresholds for a Mw 6.4 and a Mw 7.1 earthquakes, respectively. (b) and (c) All the radiators from the origin time to 50 s for the Mw 6.4 (b) and the Mw 7.1 (c) earthquakes, respectively. The filled radiators are radiators before an earthquake ends. The small black dots denote aftershocks detected and relocated by H. Huang et al. (2020).

CHAPTER 3

Application of MLBP to tsunami early warning

Abstract

Taking the advantage of the short data collection time, we develop a tsunami warning approach based on MLBP method using local seismic networks ($0.7°<\Delta<3.5°$). Case studies of the 2003 Mw 8.1 Tokachi and the 2011 Mw 9.0 Tohoku earthquakes demonstrate fast and accurate predictions for tsunami warning. In this chapter, we first introduce the background for tsunami early warning. Then we introduce the workflow of the tsunami warning approach based on MLBP and show the results of the two case studies. We then discuss the uncertainties of the predicted tsunami waves. At last, we discuss the generalization of the tsunami approach to the region with smaller station density.

This chapter is modified from Xie, Y., & Meng, L. (2020). A multi-array back-projection approach for tsunami warning. Geophysical Research Letters, 47(14), e2019GL085763.

I am the first author to develop the tsunami approach, conduct back projection and tsunami simulation.

3.1 Introduction for tsunami early warning

Near-field (about 30-60 min after earthquake) tsunami warning in the absence of tsunami data is challenging, especially for real-time predictions of tsunami arrival time and wave heights. Seismic waves and land-based geodetic data are available sooner than direct tsunami

data, so they can be potentially used to construct a source model for the prediction of tsunami waves. As a first step, point source solutions are automatically derived from seismic data after an earthquake, which are then used to evaluate the tsunamigenic potential of the earthquake. For instance, the W-phase solution (Kanamori & Rivera, 2008) determines the moment robustly based on long-period seismic body waves. Those solutions can be obtained in a short timeframe (about 5-10 min using regional seismic data or about 15 min using teleseismic data) (Zhao, Duputel, & Yao, 2017; Duputel et al., 2012). The Pacific Tsunami Warning Center (PTWC) is using a similar method to carry out real-time tsunami forecast models (RIFT) of tsunami propagation using W-phase solutions with a uniform slip (D. Wang et al., 2012). However, since this approach does not include the rupture area or the final slip distribution, it is ineffective to make accurate site-to-site tsunami predictions. Tele-seismic data (about 15 min after earthquake) can be inverted in real-time to derive a slip model. However, such inversions suffer from non-uniqueness and tradeoff between rupture speed and final slip distribution (e.g. Lay, Yue, Brodsky, & An, 2014; An, Sepúlveda, & Liu, 2014). The real-time application of land-based GPS and strong-motion recordings has also been explored for the purpose of tsunami warning (e.g. Melgar & Bock, 2015). Such an approach leads to a fast estimation of the fault slip distribution (< 10 min), and can be enhanced by ocean-bottom GPS sensors, which provide better constraints of slip near the trench and hence the tsunami generation

Over the last two decades, the development of large-scale dense seismic networks, such as USArray, ORFEUS array (European network), China National Seismic Network, and Hi-net (Japanese network), has enabled rapid progresses in many fields in seismology, including the back-projection (BP) technique which images the spatial and temporal rupture process based on the wave arrivals (e.g. Meng et al., 2014). Previously, a tsunami prediction approach based on the BP analysis of seismic data recorded at regional or teleseismic distances is poposed by (An & Meng, 2016). This approach does not depend on the assumptions of prescribed fault length, width and average slip in pre-calculated tsunami scenarios,

and also circumvents the non-uniqueness issue in source inversion using seismic waveforms. The required epicenter information in this method can be provided by standard earthquake warning systems; The moment magnitude can be obtained from high-rate GPS estimations or regional W-phase inversion (Allen & Ziv, 2011; Zhao et al., 2017). The fault geometry can be constrained by the focal mechanism of the W-phase solution or extracted from the slab geometries in subduction zones (e.g. Hayes, Wald, & Johnson, 2012). The procedure is illustrated and tested for tsunamis generated by the 2011 Tohoku, 2014 Iquique and 2015 Illapel earthquakes (An & Meng, 2016).

For the sake of waveform simplicity and coherency, the BP-based tsunami approach originally uses direct P-waves recorded by regional seismic arrays or teleseismic arrays. The data collection time in regional and teleseismic arrays are on the order of 5 min and 15 min, respectively. The local stations potentially provide faster warning but are not included because the P-wave BP requires longer S-minus-P time than the rupture duration to avoid the overlapping of multiple phases. Here, in order to reduce the data collection time, we apply a multi-array S-wave BP method using seismometers at local distances (between 0.7 to 3.5 degrees). This approach first calculates source back-azimuths using individual arrays and then merges them to constrain the kinematic rupture process. We test this multi-array BP approach in a simulated real-time environment for the 2003 Mw 8.1 Tokachi-oki and the 2011 Mw 9.0 Tohoku earthquakes. The data acquisition is shortened to 100 s for S-waves recorded by local stations (about 3.5 degrees) compared with 300 s for P-waves at regional distance (about 10 degrees). Based on the local BP approach, accurate tsunami predictions are available 7 min after the origin time compared with 9 min using regional BP, if an accurate estimation of the magnitude inverted from W-phase is operationally achievable within 5 min. Our method could deliver fast tsunami warning without blind zones along the near-field coastal regions for future repeats of both the Tohoku and Tokachi events. Our method sets the basis for developing an automatic procedure that provides rapid predictions of tsunami arrival times and wave heights in the near-field.

3.2 The workflow of the MLBP-based tsunami early warning approach

The MLBP-based tsunami warning approach (Fig. 3.1) is briefly described as follows. First, the BP approach determines the centroid locations of strong seismic radiations by analyzing the S-wave trains recorded by multiple local clusters of stations (black dashed squares in Fig. 3.1(b). In standard teleseismic BP, the seismograms are filtered at high-frequencies (about 1 Hz) to achieve high spatial and temporal resolutions, which are more efficiently generated by the abrupt change in rupture speed, rather than by total large slip (e.g. Madariaga, 1983). Here, we analyze the low-frequency signal (about 0.06 Hz) which is more representative of the static slip and therefore tsunami generations. The seismic radiators can be regarded as the centroid locations of seismic sub-events at different stages during an earthquake. We use an ellipse that encloses the seismic radiators to approximate the rupture area. We then develop a simplified source model with uniform slip over the estimated rupture area, based on the assumption that the long-period tsunami waves are not sensitive to the detailed slip distribution (An, Liu, Ren, & Yuan, 2018). Given the rupture area S inferred from the BP result and the seismic moment M_0, the average slip, D_a can be evaluated using the definition of seismic moment $M_0 = \mu S D_a$, assuming a crustal rigidity of μ=32 GPa. To facilitate timely warning, the original array-based tsunami prediction approach indirectly infers the moment based on a scaling relation between the rupture area and seismic moment, derived for large (M 6.7 to M 9.2) subduction-zone earthquakes (Murotani, Satake, & Fujii, 2013). More accurate estimates of seismic moment of M>7.5 earthquakes can be retrieved by global W-phase solutions within 20-30 min after the event origin time using teleseismic records (Duputel et al., 2012), which is too slow for the near-field tsunami predictions. Recently, rapid W-phase solutions are made available by Zhao et al. (2017) within 4 to 7 min after the event origin time using regional and local seismic data with relatively small magnitude errors (+-0.2). We envision to implement the regional W-

phase inversion alongside our tsunami warning method which allows the retrieval of accurate seismic moment in a time frame comparable to the local BP operations.

We envision that the BPs will be applied automatically to the continuous recording in real-time. It's therefore essential to identify the beginning and the end of the earthquake. We assume that the origin time of the earthquake is provided by the authority such as the JMA EEW system. The end of the earthquake can be described by the spatial scattering of the successive radiators. During the earthquake, the seismic radiators are focused in space due to coherent S-wave arrivals. At the end of the earthquake, the radiators become scattered due to the dominance of the coda waves. An earthquake can be considered to end when the spatial variance of the radiators exceeds the maximum possible separations within a time window.

Once the locations of seismic radiators are determined, we construct a simplified source model for tsunami forward simulation. First, we estimate the rupture zone by enclosing the radiators with an ellipse using the confidence interval algorithm (Fig. 3.2). The radiators are fitted by a covariance ellipse representing 95% confidence.

The ellipse is projected onto a fault plane defined by the real-time focal mechanism from a regional W-phase solution. Pre-mapped fault catalogs such as the Slab 2.0 or the outer-rise normal fault traces can be used to distinguish between the two candidate fault planes. We measure the area of the projected ellipse, S_{bp}. Since the low-frequency (about 0.06 Hz) BP radiators represent centroid locations of seismic sub-sources, we assume that the "asperities" (area of large slip) dominate the tsunami generation and the contributions of low-slip rupture area can be ignored in the tsunami wave simulation. Fig. 3.4(a) and 3.5(a) show that the elliptical source area enclosing the BP radiators are similar to the "asperity" (source area with slip larger than 1.5 times of the average slip) defined in Murotani et al. (2013). Then we determine the average slip inside the BP-inferred area, D_{bp}. The average slip on the total source area, D can be inferred based on seismic moment and the whole rupture area, S. To estimate D_{bp}, we establish an empirical relation between the degree of
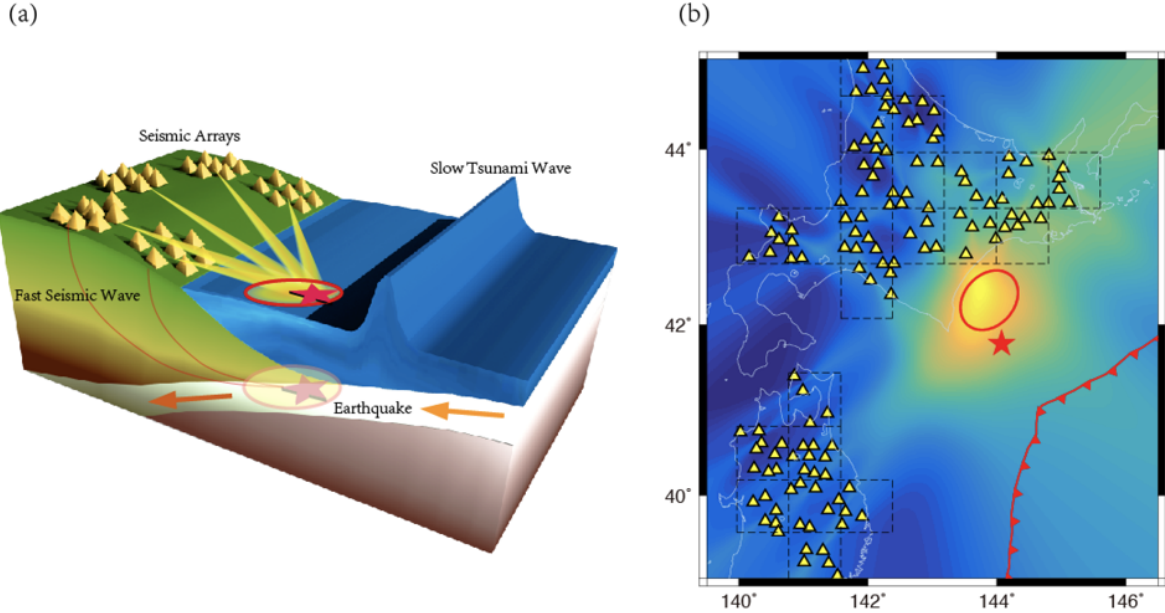
Figure 3.1: (a) Sketch of tracking tsunami-genic earthquakes with multi-array back-projection method. The seafloor motion excites the tsunami wave during a megathrust earthquake that occurred at the subduction interface. The red stars represent the hypocenter and epicenter. The earthquake rupture area (red ellipse) is imaged by the local onshore seismic networks (yellow tetrahedrons). (b) The snapshot of the multi-array back-projection image. The background color indicates the joint spatial probability distribution of the source location 10 seconds after the origin time of the M 8.1 Tokachi earthquake determined with multi-array BP analysis using 22 Hi-net clusters (black dashed squares) and 31 K-NET clusters. Yellow triangles are Hi-net stations that are used. The red star is the epicenter. The red ellipse is the large slip region enclosing 95% of the radiators.
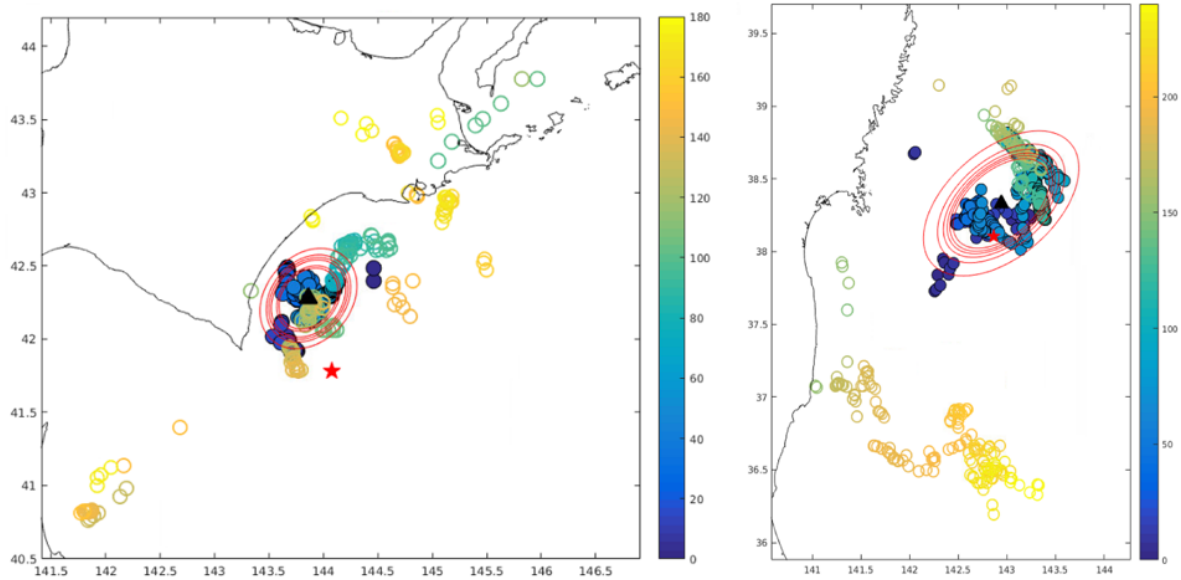
Figure 3.2: The simplified source model constructed by enclosing the radiators with an ellipse using the confidence interval algorithm. All the radiators from the origin time to 180 s and 240 s are shown for the Tokachi (a) and the Tohoku (b) earthquakes, respectively. The filled circles are radiators before an earthquake ends, which are used to fit the ellipse. The red ellipses are scaled to enclose 70%, 75%, 80%, 85%, 90%, 95% of the radiators before an earthquake ends.

slip concentration (D_{bp}/D) versus normalized source area (S_{bp}/S), based on slip models of 8 historical tsunamigenic megathrust earthquakes (Fig. 3.3). Following the same method as Murotani et al. (2013), we define the rupture area S as the total area of subfaults of the slip model with slip greater than 0. For the Tohoku and Tokachi earthquakes, S_{bp}/S is about 0.133 and D_{bp}/D is about 2.95. Based on this relation, the total area S is first estimated using the BP-inferred area S_{bp}. Then using the seismic moment estimated from the W-phase, the average slip D is calculated according to the definition of seismic moment $M_0 = \mu SD$ assuming the rigidity of the fault zone rock is 32 GPa. Then, we construct a uniform slip model assuming that the slip over the BP source area D_{bp} is 2.95 times of the average slip D. Finally, we conduct a tsunami simulation to predict the amplitudes and arrival times of the tsunami waves.

3.3 The case studies

3.3.1 The 2003 Mw 8.1 Tokachi earthquake

Our MLBP-based warning approach is applied in a simulated real-time fashion to the 2003 Mw 8.1 Tokachi-oki event and the 2011 Mw 9.0 Tohoku event. The size of a cluster of stations needs to balance the waveform coherency, the plane wave assumption and the resolution of the BP imaging. We run 7 tests using 8 reference earthquakes to determine the optimal number and size of the clusters based on the slowness and source location uncertainties. We then compare the BP results of the Tokachi and Tohoku events using 4 different grouping methods, which produce consistent BP patterns. For simplicity considerations, we adopt the uniform-grid configuration with the size of 70 km. For the Tokachi event, we use 53 square seismic clusters with epicentral distances smaller than 3.5 degrees, 31 of which are constructed from the K-NET strong motion stations and 22 from the Hi-net stations, respectively ((Fig. 3.1(b)) and (Fig. 3.4(a)). The station spacings are between 11 - 15 km for the K-NET and 15 - 55 km for the Hi-net. We adopt the transverse component to enhance
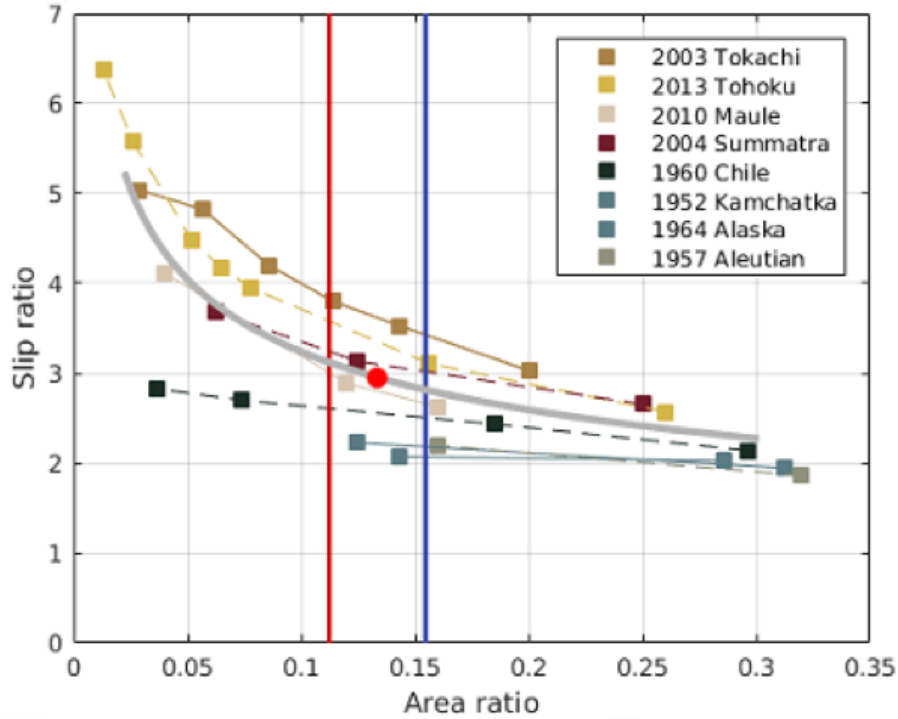
Figure 3.3: The empirical relation between slip ratio (D_{bp}/D) and area ratio (S_{bp}/S), based on slip models of 8 historical tsunamigenic megathrust earthquakes (Satake, Fujii, Harada, & Namegaya, 2013; Fujii & Satake, 2013; Romano, Piatanesi, Lorito, & Hirata, 2010; Fujii & Satake, 2007; Johnson et al., 1994; Johnson, Satake, Holdahl, & Sauber, 1996; Johnson et al., 1994; Johnson & Satake, 1999). The slip ratio is the average slip on the asperity over the average slip on the whole rupture area. The area ratio is the asperity area over the whole rupture area. The squares show how the slip ratio and the area ratio vary when changing the slip ratio threshold to define the asperity. The grey solid curve is the regression line of all the data (squares). The red and blue vertical lines show S_{bp}/S of the Tokachi and Tohoku events, where S_{bp} is inferred from the multi-array BP analysis and S is measured from the slip model inferred from tsunami observations (Romano et al., 2010; Satake et al., 2013). The red point is the slip ratio corresponding to the average area ratio of the two events on the regression curve (the grey line). The estimated area ratio and slip ratio are 0.133 and 2.95.

the signal of the S wave and filter the waveforms to a low-frequency band of 0.05 - 0.1 Hz for Hi-net stations (after removing the instrument response) and 0.01 - 0.07 Hz for K-NET stations. Note that we adopt the velocity measurements recorded by Hi-net and acceleration data recorded by K-NET. The stations of the two networks are used separately for the BP analysis. Since we combine the BP results instead of the data from the two networks, it is not necessary to uniformly convert the recordings to either acceleration or velocity. Only the Hi-net stations are used to image the initial stage of the rupture process, because the initial S-waves did not reach the triggering threshold of the strong-motion accelerometers (The triggering time ranges from 27 s to 68 s after the S-wave arrival depending on the stations in K-NET).

We perform the correlation stacking approach (equation 2.1) to the Tokachi earthquake recordings with a 30-second sliding window to calculate the back-azimuths. This relatively long window corresponds to the relatively long-period filter we apply to the data. Then equation 2.2 is used to intersect the back-azimuths of individual clusters and identify the seismic radiators, shown as colored circles in Fig. 3.4(a). The locations of the seismic radiators agree well with the principal slip zone defined by a finite fault inversion model using tsunami waves [Romano et al., 2010]. The time span of coherent BP is about 82 s, which exceeds the reported earthquake duration of 50 s based on the finite fault solutions (Yagi, 2004; Yamanaka & Kikuchi, 2003). This apparent longer duration is possibly due to the dominance of long-period S and Love phases after applying the low-frequency filter. The area of the fitted ellipse S_{bp} is 4,310 km^2, which corresponds to an average slip D_{bp} of 6.08 m, given the USGS W-phase moment magnitude estimate of Mw 8.16. These estimations yield more concentrated slip compared with the large-slip zone in the Romano model, with an S_{bp} area (area of all the grids with slip larger than 2.95 times of the average slip) of about 6,200 km^2 and an average slip D_{bp} of 4.14 m. The estimated total rupture area is 32,405 km^2, which is close to 31,000 km^2 in the Romano model.

Using the prescribed fault surface based on the Slab 2.0 model (strike = 210°, dip =

Figure 3.4: The case study of the 2003 Mw 8.1 Tokachi-oki earthquake. (a) The brownish circles are back-projection radiators color-coded by time and sized by normalized power. The red ellipse encloses the estimated 'asperity' region; The red star is the epicenter and yellow triangles are strong motion stations. Black triangles are tsunami stations. The dashed black squares mark the clusters of stations used for the array analysis. The estimated warning time (color circles along the coast) is estimated by subtracting the time needed for data processing (2 min), S wave propagation (within 2 min) and the rupture duration (within 3 min) from the arrival time of tsunami wave observed by Tanioka et al. (2004). The greyish tiles are the slip distribution estimated with tsunami data (Romano et al., 2010). The yellow curve encloses the region with a slip larger than 1.5 times of the average slip; (b) The runup heights estimated from the elliptical source model (red) and tsunami heights from a post-tsunami survey (grey dots) (Tanioka et al., 2004). The magenta stars denote the peak amplitudes at the coastal tsunami stations; (c) The measurement (black) and tsunami waveform (red) predicted by the simplified rupture model.

39

19.5°) and assuming a rake angle of 90°, the source model with uniform slip distribution is implemented to predict the tsunami waves. For fast real-time computation, we adopt the linear version of COMCOT v1.7 package (X. Wang & Liu, 2006, 2007) to calculate runup height and PCOMCOT (An et al., 2014), a parallel version of COMCOT to compute the tsunami waveforms. The computing region is divided into 2,131,825 elements with grid size of 15 arcsec. Using 128 cores (Intel(R) Xeon(R) Gold 6148 CPU @ 2.40GHz), two hours of tsunami wave propagation with a time step of 0.6 s takes 1 minutes and 44 seconds to compute, which is sufficiently fast for tsunami predictions in the near-field. Computation time can be shortened further if we use more cores, multi-scale grids, less time steps or smaller computation ranges. Note that due to the non-linear effect, relatively coarse grids in real-time simulation, and the limited bathymetry resolution, our simulations tend to underestimate extremely large local runup heights in some areas. It nevertheless captures the overall runup patterns along the coastline (Fig. 3.4(b)).

The amount of the estimated warning times (difference between tsunami arrival time and the time for issuing the warning, shown by the colored circles along the coast line on (Fig. 3.4(a)) are greater than 20 min using our approach in the best case scenario when the W-phase solution could be achieved within 5 minutes. We describe the estimation of warning time in more details in the discussion part. We compare our predictions with recordings at 16 coastal tsunami stations and 2 ocean bottom tsunami-meters in Hokkaido and northern Honshu. The average errors of the predicted arrival times and amplitudes are 4.14 min and 0.14 m, respectively. At 80% of the stations, the arrival time and amplitude errors are smaller than 5.94 min and 0.33 m, respectively, which achieves sufficient accuracy for warning purposes.

3.3.2 The 2011 Mw 9.0 Tohoku earthquake

The proposed methodology is also applied to the tsunami generated by the 2011 Tohoku earthquake. We use 28 square clusters of the K-NET strong motion stations and 23 square

clusters of the Hi-net stations (Fig. 3.5(a)). The size of the clusters is 70 km. All stations are located in eastern Honshu with epicentral distances smaller than 3.5 degrees. We conduct the MLBP using the same parameters as the Tokachi earthquake. The inferred seismic radiators are shown as the colored circles in 3.5(a). The time duration for BP is about 128 s, which is comparable to other BP studies using teleseismic stations or local strong motion networks (Kiser & Ishii, 2012; Meng et al., 2011; Maercklin et al., 2012; Honda et al., 2011). The inferred source region is consistent with the principal slip zone in the finite fault inversion model based on tsunami recordings (Fujii, Satake, Sakai, Shinohara, & Kanazawa, 2011). The estimated S_{bp} is 10,769 km^2. Based on the moment magnitude of Mw 9.1 determined by USGS W-phase solution, the average slip D_{bp} is 44.3 m. In comparison, the S_{bp} and D_{bp} estimated from the model of Satake et al. (2013) are 13,927 km^2 and 36.32 m, respectively.

A uniform slip model is then constructed in order to predict the tsunami waves using COMCOT. The resolution of the bathymetry data and the computing grid sizes are 30 arcsec. The amount of the estimated warning times is greater than 16 min using our approach assuming that the W-phase solution could be achieved within 5 minutes. The coastline near the Sendai bay is concave landward and its shallow water area is larger than the neighboring Iwate region in the north and the Fukushima area in the south, resulting in a slower tsunami wave speed and counterintuitive later arrival and longer warning time despite of its closer proximity to the source region (Fig. 3.5(a)). We compare our predictions with 28 tsunami recordings and post-tsunami survey data (Mori et al., 2011)(Data from the 2011 Tohoku Earthquake Tsunami Joint Survey Group, 2012). The average errors of the predicted arrival times and amplitudes are 3.14 min and 0.55 m, respectively. The arrival time and amplitude errors at 80% stations are smaller than 4.27 min and 0.78 m, which is reasonably small for warning purposes. The runup heights are underestimated for the coastal region from 39.5° N to 40° N. A possible second tsunami source near the trench around 39.5 °N (Satake et al., 2013) may contribute to the larger tsunami heights observed along the Sanriku coast.
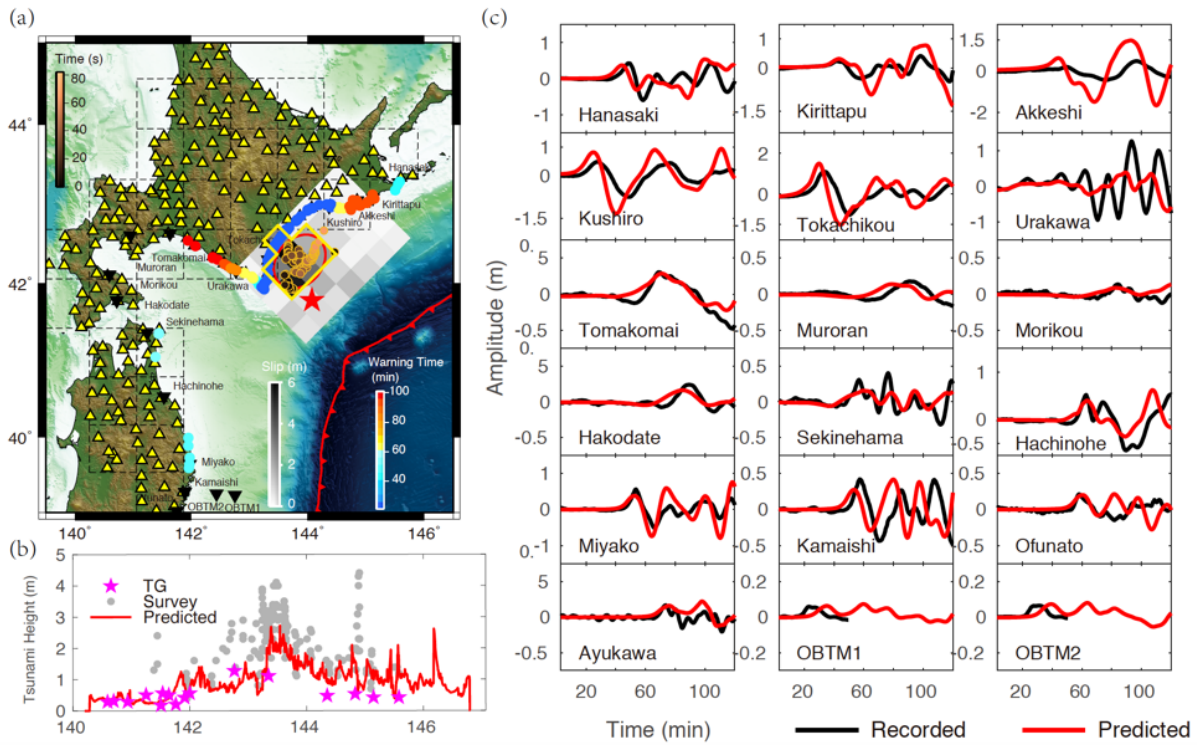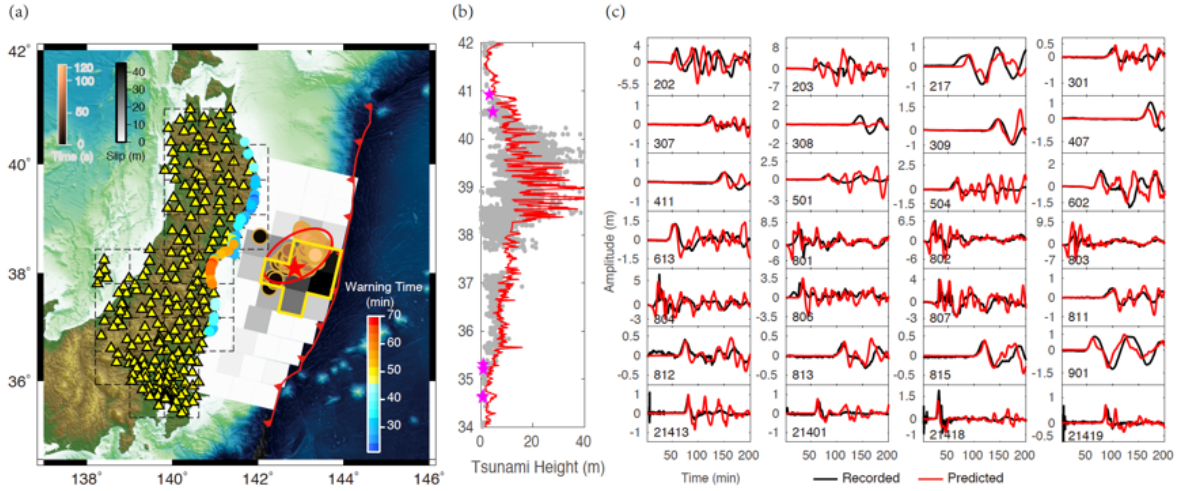
Figure 3.5: The case study of the 2011 Mw 9.0 Tohoku event. (a) The brownish circles are back-projection radiators color-coded by time and sized by the normalized power. The red ellipse encloses the estimated 'asperity' region; The red star is the epicenter and yellow triangles are strong motion stations. The dashed black squares mark the clusters of stations used for the array analysis. The estimated warning time (color circles along the coast) is estimated from the arrival time observed by Muhari, Imamura, Suppasri, and Mas (2012). The greyish tiles are the slip distribution estimated with tsunami data (Fujii et al., 2011). The yellow curve encloses the region with a slip larger than 1.5 times of the average slip. (b) The runup heights estimated from the elliptical source model (red) and tsunami height from a post-tsunami survey (grey dots) (Mori, Takahashi, Yasuda, & Yanagisawa, 2011). The magenta stars denote the peak amplitudes at the coastal tsunami stations; (c) The measurement (black) and tsunami waveform (red) predicted by the simplified rupture model.

3.4 The accuracy of the predicted tsunami wave

The case studies of the Tokachi-oki and Tohoku earthquakes allow us to assess the performance of the simplified source model in predicting tsunami generations. First, since the multi-array approach uses a low frequency band (0.05-0.1 Hz and 0.01-0.07 Hz), we are explicitly assuming that the "asperities" (source areas of large slip) are responsible for the tsunami generation. This assumption seems to provide better tsunami predictions than the uniform slip models over the entire rupture area explored in our previous work (An & Meng, 2016). In our case studies, this asperity model successfully captures the decay of the run-up height along the coastline as a function of the epicentral distance. In comparison, the runup heights predicted by uniform slip models over the whole rupture area are underestimated close to the epicenter and overestimated away from the epicenter (An & Meng, 2016); The value of S_{bp}/S and D_{bp}/D may inherit the uncertainties and peculiarities of the slip models of the 8 earthquakes we used to derive the scaling relation, which may contribute to the errors of the simplified slip model, thus the predicted tsunami waves. Another simplification is that the 3D velocity variation is not considered when the S-wave arrival times are calculated. Moreover, the location estimation of the radiators is achieved assuming the theoretical back-azimuths are along the great circle path, which ignores the ray path distortion due to lateral velocity variation. These problems are partially mitigated by our strategy of combining multiple clusters, which bears some tolerance on the back-azimuth errors (Fan et al., 2018). We do not apply the static correction of the back-azimuths in this study because the initial seismic recordings at strong motion stations are not available. This bias of the back-azimuths is about 10 degrees for the Kyushu array and is possibly caused by the lateral velocity contrast between the island arc and the back-arc basin. In our future work, we will test if the local 3D velocity model improves the location accuracy of the BP radiators (Z. Liu et al., 2017). We will pre-calculate such travel-time tables and corrections for back-azimuth errors for target source regions to facilitate real-time BP. Alternatively, empirical correction can be applied to improve the accuracy of the BP radiators (Ishii, Shearer, Houston, &

Vidale, 2007; Meng et al., 2014, 2016). The back azimuths bias can be estimated based on the difference between the theoretical and measured back-azimuths of relocated background earthquakes.

The proposed warning approach achieves reasonable predictions of tsunami waves (Fig. 3.6). The errors of the amplitudes and arrival times range from -1.59 to 3.74 m and -10.0 to 10.0 min for all tsunami stations, respectively. The errors at 80% of the stations are less than 4.75 min in arrival time and 0.42 m in amplitude. This error level is close to the predictions using high-rate GPS data (Melgar & Bock, 2013), which is reasonably small for tsunami early warning purpose. Most of the arrival time errors can be accounted by the limited resolution of the bathymetry data used in the tsunami forward simulation. For example, the predicted arrival time is about 5.4 min earlier than the measurement at the station Akkeshi (Fig. 3.4(c)) . Using 15 arcsec bathymetry data, which initially places the station on land, we have to move the station 1500 m into a wet grid point in the wave propagation simulation, which results in about 4.5 min error for the arrival time considering that the water depth of this region is about 3 m and the tsunami wave velocity is 5.5 m/s.

The runup heights are underestimated in both case studies. For the Tohoku event, the runup heights from 39.5° N to 40° N are significantly underestimated. Satake et al. (2013) use 53 tsunami stations to invert for the slip model. Their result indicates that a delayed shallow rupture with a 10 m slip is responsible for the maximum tsunami heights measured on the Sanriku coast. In our approach, the later rupture in the south of the principal-slip area is missing, which may be masked by the Love wave of the previous sub-sources (Maercklin et al., 2012). In this scenario, the seismic radiation of the rupture on splay faults is also masked by the plate-interface rupture and is hence not able to be picked up by the BP method, which leads to the underestimation of the elevated run-up near Sanriku. Besides, the inundation is sensitive to the topography and bathymetry near the coast. The runup heights predicted from the slip model of Satake et al. (2013) fit the observations very well, using the digital bathymetry charts (M7000 series) provided by MIRC, which has a resolution

44
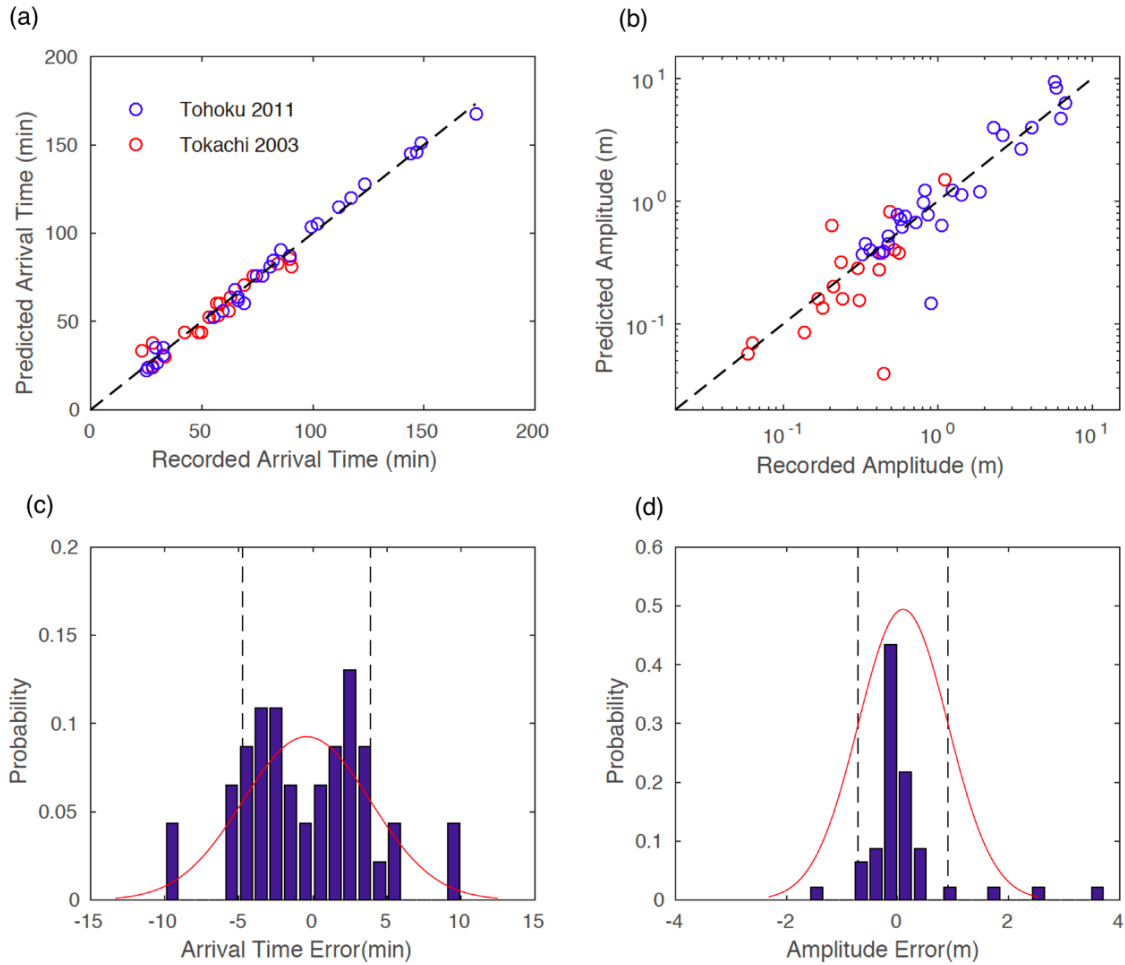
Figure 3.6: Errors of predicted arrival time and amplitude at all tsunami stations for the Tohoku and Tokachi earthquakes. (a) Predicted and recorded arrival time; (b) Predicted and recorded amplitude; (c) Arrival time error distributions; (d) Amplitude error distributions. The red curves are the fitted probability density using a Gaussian distribution. The dashed lines mark the region within the standard deviation.

of 5 arcsec near the coast. Shimozono et al. (2012) investigate the inundation characteristics of the 2011 Tohoku event on the central Sanriku coast using 50 m bathymetry data and find that the tsunami height has a positive dependency on topographic slopes and shows significant variations along the coastline. They also suggest that compared to the U-shape bays, the V-shape bays (The case for Sanriku coast) suffer from more severe funnel effects and local wave resonances, which contributes to the observed extreme heights. With the 30 arc-seconds (about 1000 m) bathymetry after smoothed by the preprocessing by COMCOT, we cannot reproduce local effect caused by the kilometer-scale V-shape bays. Suppasri et al. (2016) reviewed the improvements of tsunami simulations using fine topographical data with a resolution of 5 m. Thus, the underestimation of tsunami height of our method is partially caused by missing a possible secondary tsunami source and by the coarse bathymetry (30 or 15 arc-seconds), which limits the capability of predicting the complicated wave behavior near the coast.

The first reliable W-phase inversion can be obtained using regional stations (5-6 degrees) within 5 min for the Tohoku event (Zhao et al., 2017). Assuming that data processing costs 2 minutes, the propagation of S waves takes about 100 s and that the rupture duration of the earthquake is 3 min, the approach could optimistically issue the warning 7 minutes after the initial rupture of the Tohoku earthquake (The data collecting, the calculation of the W-phase inversion and the BP analysis can be performed simultaneously). JMA EEW system issued the first warning for the 2011 Tohoku earthquake 5.4 s after the origin time (Hoshiba et al., 2011), which is significantly faster than the local-data collection time (100 s). Compared to the regional seismic array method (9 min) and teleseismic array method (19 min) proposed by An and Meng (2016), the warning time is significantly shortened because the local seismic data are collected faster. The warning time is comparable to the method using high-rate GPS waveforms and strong motion data (<10 min) (Melgar & Bock, 2015; Melgar et al., 2016) and slower than the widely implemented method using a pre-calculated database (The initial tsunami warning is issued 3 min after the origin time by JMA in the Tohoku event (Hoshiba

& Ozaki, 2014)). Note that the above warning time calculation assumes zero delay in data telemetry. Practically, the strong motion networks (e.g. K-NET and KiK-net) transmit the seismograms a few minutes after an event due to the triggered-system. Furthermore, the strong shaking may cause damage and blackouts in the closest stations preventing real-time data transmission. This situation is common to all seismic-based warning approaches and needs to be addressed by the network operators. The Hi-net stations are capable of real-time telemetry and are used in the JMA EEW systems (Hoshiba, Kamigaichi, Saito, Tsukada, & Hamada, 2008). We test using only Hi-net data (with real-time transmission) for the Tohoku and Tokachi events, which achieves consistent results with those using both the Hi-net and K-NET stations. The warning systems based on the tsunami observations are more reliable but require a dense tsunami array. Yamamoto, Hirata, et al. (2016) proposed a real-time tsunami forecast system by matching the offshore pressure data recorded by the cabled network, S-net with the pre-calculated tsunami height spatial distributions. They develop a method to constrain the centroid location of tsunami sources using S-net within several minutes. We also develop a tsunami warning approach based on inversion result using tsunami recordings and we will introduce it in the last chapter. In 3.4(a) and 3.5(a), we show the theoretical warning time of the MLBP-based tsunami warning approach estimated by subtracting the minimum time needed to generate an alert using our approach of 7 minutes from the measured arrival times of tsunami waves (Tanioka et al., 2004; Muhari et al., 2012). None of the coastline falls in the blind zone. The minimum warning times are 21 min and 16 min for the Tokachi and Tohoku events, respectively. The proposed warning approach is also easy to implement. The seismic clusters can be designed or pre-selected among existing networks prone high tsunami risks. The BP and tsunami waveform prediction process can be fully automated without human intervention. The proposed warning approach is a complement to the current warning systems. A combination with early warning approaches based on W-phase and high-rate GPS, as well as tsunami observations can potentially reduce the uncertainty and provide a more reliable outcome.

3.5 Generalize to low station density area

For global applications, it is important to understand the minimum station density to achieve reliable local BP. We conduct BP tests with 1/2, 1/4 and 1/8 of the original stations with different array configurations. We found grouping the stations into overlapping circular sub-arrays with a radius of 80 km achieves the best results for these low station density cases. Using this clustering method, the result using 1/4 stations are shown in Fig. 3.7. Other results are shown in Figure S22 to S30 in the paper Xie and Meng (2020). The 1/2, 1/4 and 1/8 station spacings are 30 km, 50 km and 70 km, respectively, which are comparable to the cases of Alaska or Cascadia, Southern America and Sumatra, respectively. Using 1/2 and 1/4 stations, we obtain consistent BP results, close rupture area and slip with those using all of the stations. The BPs with 1/8 stations are considerably more scattered due to aliasing effects. We consider our proposed warning approach can be applied to the existing networks in most of the major subduction zones except sparsely-instrumented area like Sumatra.

3.6 Conclusion

We developed an MLBP-based tsunami warning approach that predicts tsunami arrival time and wave heights based on rapid earthquake source characterization through back-projections (BP) of seismic arrays at local distances (0.7 to 3.5°). The back-azimuths retrieved by individual arrays are combined to estimate locations of low-frequency (about 0.06 Hz) seismic radiators. This multiple-array back-projection scheme mitigates the artifacts due to overlapping multiple phases and coda waves, and reduces the source location uncertainties due to 3D travel-time errors. The local BP observations allow for the construction of uniform-slip models enclosing the "asperity" (area of large slip), which is responsible for most of the tsunami generation. We also develop an empirical scaling relation to determine the slip of the asperity model, and an automatic procedure to determine the end of an earthquake in continuous seismic recordings. We apply the MLBP-based tsunami warning
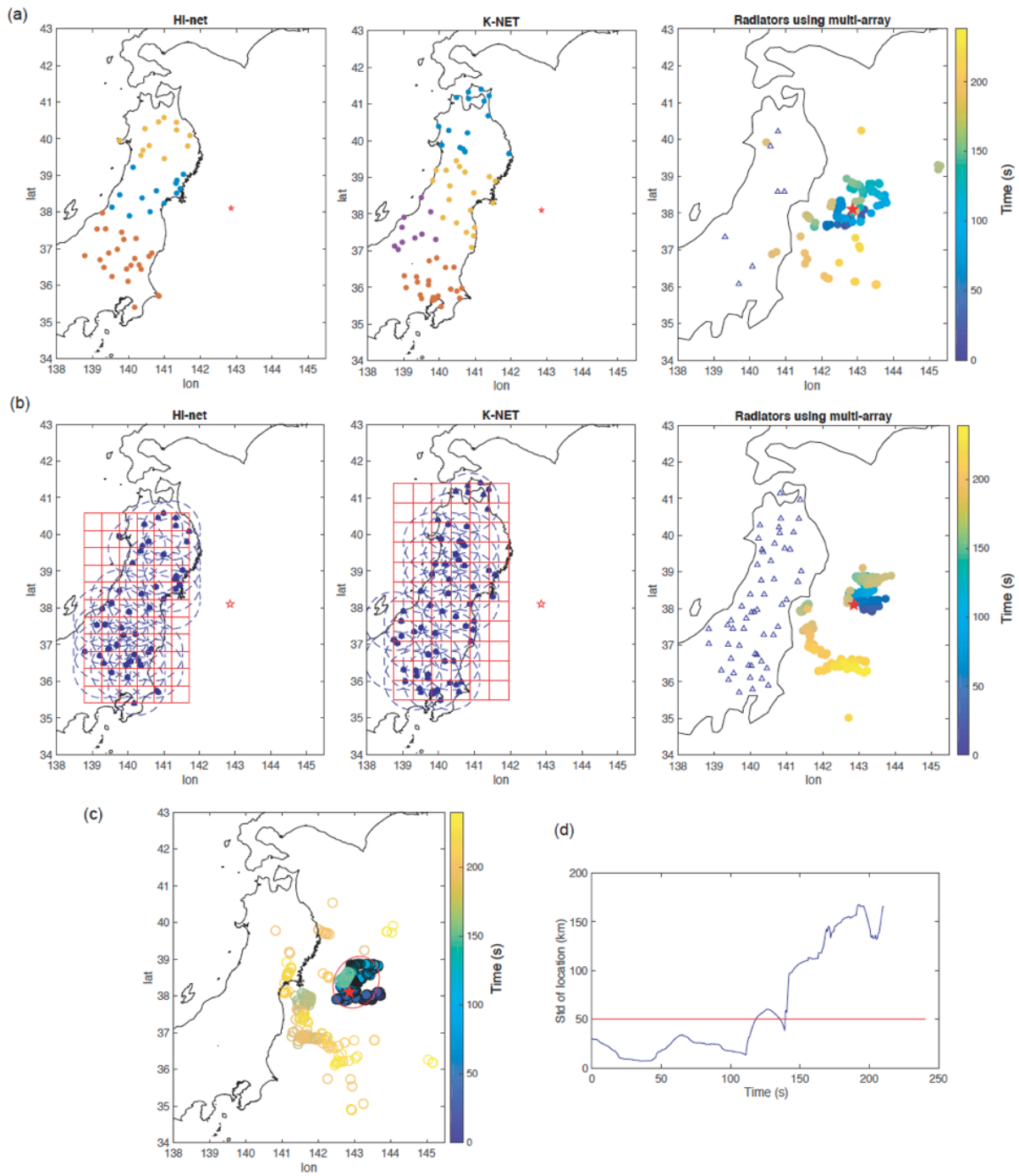
Figure 3.7: (Caption next page.)

(Caption of Fig. 3.7)Result of BP analysis of the 2011 Tohoku earthquake using 1/4 of the existing stations (a) Divide the Hi-net stations (left) into 3 clusters and K-NET (middle) to 4 clusters for Tohoku earthquake using K-means algorithm. (b) 26 circular overlapping clusters of Hi-net stations (left) and 26 clusters of K-NET (middle) for Tohoku earthquake. The right panels show the result of the BP analysis for 240 s after the earthquake origin time. The triangles are reference stations for each cluster. The radius of the clusters are 0.8 degrees. The uncertainties of the slowness is assumed to be 20 ° for K-means clusters and 10 ° for circular overlapping clusters. (c) All the radiators in the first 240 s obtained from the circular overlapping clustering method. The red ellipse is fitted according to the terminal time determined by the spatial scattering shown in (d). The duration is 118 s and the estimated S_{bp}/S and slip are 12820 km^2 and 37.2 m, respectively.

approach to the 2003 Mw 8.1 Tokachi-oki earthquake and the 2011 Mw 9.0 Tohoku earthquake in a simulated real-time environment utilizing 51-53 local clusters of strong motion stations or short period stations. The test results show that the asperity model is an effective approximation of the tsunami source and produces reasonably small errors of arrival times and amplitudes for warning purposes. This approach provides an independent perspective of evaluating low-frequency seismic sources in real-time and achieves tsunami-height prediction in as little as 7 minutes, based on an accurate and rapid (5 min) W-phase solution, which is significantly faster than previous array-based warning approach using regional and teleseismic recordings. Our method has the potential to be applied to the existing seismic network worldwide and be integrated into the current tsunami warning systems.

CHAPTER 4

Application of MLBP to resolve the complicated rupture process of the 2019 Ridgecrest earthquake sequence

Abstract

We apply the MLBP method to the 2019 Mw 6.4 and Mw 7.1 Ridgecrest, California earthquakes to resolve their kinematic process, with the dense seismic network in California. To increase the objectivity of stations selection criteria and to be prepared for future real-time BP implementations, we improve MLBP with an automatic procedure to group stations based on waveform coherence. Our MLBP highlights the rupture complexity in a multi-fault system. The Mw 6.4 quake initiates on a 5-km-long NW-trending segment, then ruptures the primary SW-trending fault at the speed of about 1.3 km/s. The Mw 7.1 quake ruptures bilaterally for 10 km and 22 km, on the NW and SE portion of the fault, respectively, at the speed of 1 to 1.6 km/s. The rupture paths agree with aftershock distributions and surface rupture estimated from satellite imagery. The slow rupture propagation may be driven by the low structural maturity of the fault. This case study demonstrates the effectiveness of MLBP for earthquake source imaging and rapid hazard assessment.

This chapter is modified from Xie, Y., Bao, H., & Meng, L. (2021). Source Imaging With a Multi-Array Local Back-Projection and Its Application to the 2019 Mw 6.4 and Mw 7.1 Ridgecrest Earthquakes. Journal of Geophysical Research: Solid Earth, 126(10),

e2020JB021396.

I am the first author to conduct back projection and write the paper, Han Bao conducted teleseismic back-projection.

4.1   Introduction

The 2019 Mw 6.4 and Mw 7.1 Ridgecrest, California earthquake sequence occurred on a conjugate fault system in the East California Shear Zone where it reaches the Garlock fault. The kinematic rupture is modeled in many studies (Ross et al., 2019; C. Liu, Lay, Brodsky, Dascher-Cousineau, & Xiong, 2019; K. Chen et al., 2020; Magen, Ziv, Inbal, Baer, & Hollingsworth, 2020; Goldberg et al., 2020; Barnhart, Hayes, & Gold, 2019; Jin & Fialko, 2020; X. Xu, Sandwell, & Smith-Konter, 2020; Yue et al., 2021; K. Wang, Dreger, Tinti, Bürgmann, & Taira, 2020). The Mw 6.4 quake broke the SW and NW fault portions near their intersection on 4th July, while the Mw 7.1 event ruptured a much longer segment along the NW branch 34 hours later. The Coulomb stress of the Mw 6.4 event and its aftershocks promoted the Mw 7.1 mainshock by unclamping the NW portion of the fault (Barnhart et al., 2019). H. Huang et al. (2020) explain the delayed triggering of the Mw 7.1 event by analyzing the foreshock sequence and repeater earthquakes, which reveals a combined mechanism of cascade triggering and possible delayed process related to slow slip or fluid flow diffusion. The sequence fills part of the gap between the Little Lake Fault and the Airport Lake Fault to the north and the Blackwater Fault to the south (Fig. 4.1). The recent nearby events include the 1999 M 7.1 Hector Mine earthquake, the 1992 M 7.4 Landers earthquake in the south (both earthquakes are about 100 km to the south of the Mw 7.1 Ridgecrest earthquake), and the 1872 M 7.4 Owens Valley earthquake (about 44 km to the north of the Mw 7.1 Ridgecrest earthquake)(Fig. 4.1). The two earthquakes are recorded by the dense arrays in southern California, which has the potential to resolve a more detailed kinematic process of the two earthquakes.
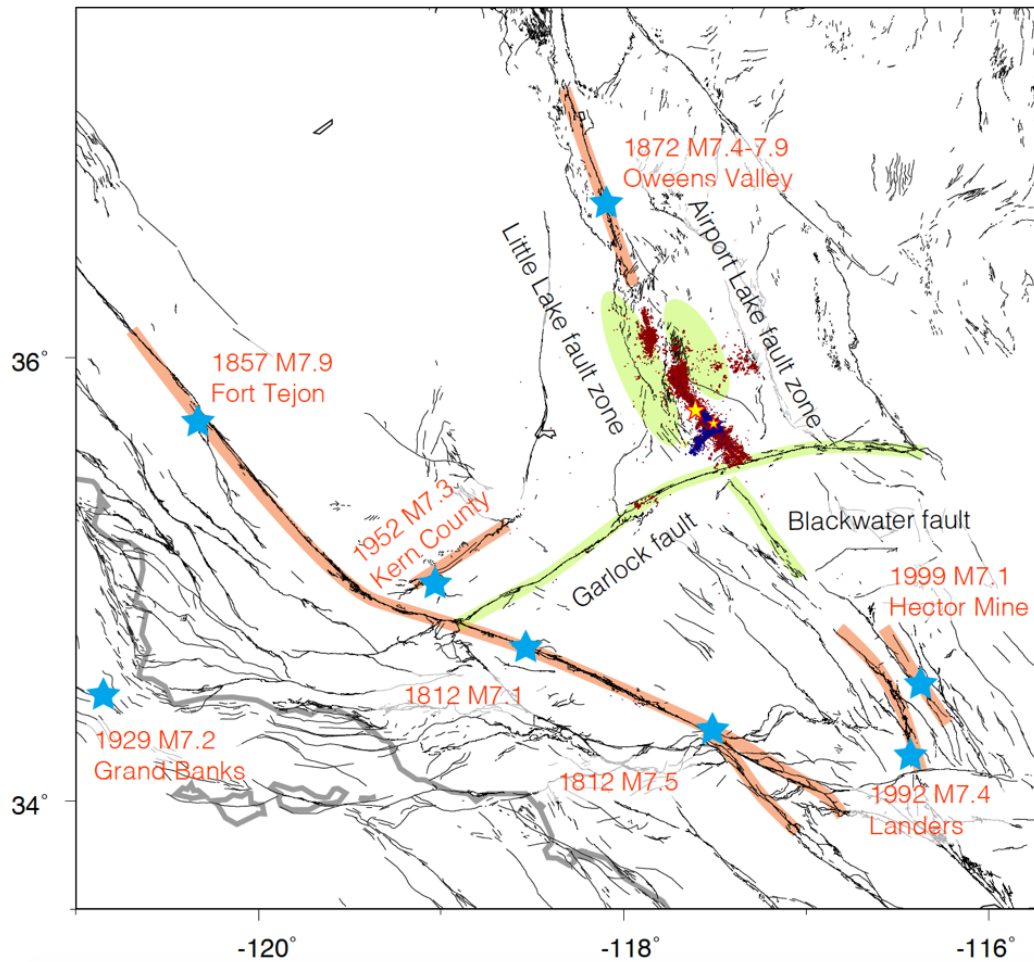
Figure 4.1: Active faults and historical earthquakes around the intersection of the Garlock Fault and the East California shear Zone. The yellow stars are the epicenters of the Mw 6.4 and Mw 7.1 earthquakes, respectively. The red dots are aftershocks within 6 months after the Mw 7.1 earthquake, the blue dots are the aftershocks between the Mw 6.4 and the Mw 7.1 earthquakes (H. Huang et al., 2020). The black lines are the Quaternary fault traces from USGS. The green shading shows faults close to the Ridgecrest earthquakes. The orange shading shows the surface rupture of recent earthquakes, modified from K. Chen et al. (2020). The grey thick lines are coastlines. The blue stars are the centroid locations of Mw 6+ earthquakes since 1976 (Global CMT)(Ekström, Nettles, & Dziewoński, 2012).

In this chapter, we first describe the data selection and station grouping process based on waveform coherence. Then we present the source imaging results of the Mw 6.4 and the Mw 7.1 earthquakes. We finally discuss the kinematic rupture processes (rupture length, speed, directivity) and compare them with previous work. In addition, we examine the reliability and uncertainty of the source parameters through extensive synthetic tests and demonstrate the potential of MLBP for high resolution rupture imaging and rapid hazard assessment for future large earthquakes.

4.2   Data selection and method

We apply the MLBP method to the Mw 6.4 and the Mw 7.1 earthquakes using both datasets recorded by strong-motion and short-period stations in California (Fig. 4.2(a) and Fig. 4.3) which are provided by SCEDC (Center, 2013) and NCEDC (NCEDC, 2014). For the strong-motion data, we first correct the waveform polarity by changing the signs of the waveforms according to the radiation pattern of the first P-phase estimated from the GCMT solution (Dziewonski, Chou, & Woodhouse, 1981; Ekström et al., 2012). Without this correction, the signs of the waveforms are not consistent among stations because some sub-arrays (C1, C10, C11, D1, D11) are passed through by the nodal planes. The corrected waveforms are used for all the following analysis including BP calculations. Following Walker et al. (2005), we align the first P-wave (with polarity corrected) using an iterative, cross-correlation technique (with a reference station) from low to high frequency bands (Reif, Masters, Shearer, & Laske, 2002). Then we examine the mutual coherence of waveforms of all available stations based on the K-nearest-neighbor algorithm. The most coherent group of stations is approximately 1.5 to 4° (166 to 444 km) away to the south of the epicenter, thus we consider the stations within this range of epicentral distance in our analysis. To maintain good azimuth coverage and adequate plane-wave assumptions, we group all potential stations into fan-shaped sub-arrays (Fig. 4.2(a)), each covering an azimuthal range of 20° with an

interval of 10°. Each sub-array spans an epicentral distance range of 100 km centered at 2° (222 km). An array with larger azimuthal range has higher resolution and stability for BP imaging but affects plane wave assumption and has lower coherence (Xie & Meng, 2020). We choose the optimal azimuthal ranges and intervals of sub-arrays by several tests. If there are less than 10 stations in a sub-array, we expand the azimuthal angle and epicentral distance ranges to 60° and 150 km, respectively.

After we divide all the available stations into fan-shaped sub-array, we use the method corrmap to select the stations with high mutual coherence (higher than half of the average cross-correlation coefficient (CC) of all station pairs within a sub-array). We first calculate the CC of the first 4-second waveform in 0.5 to 2 Hz after the P arrival for each pair of stations in the sub-array. Then corrmap reorders the stations based on the correlation coefficients for selecting the largest subgroup with high mutual coherence in the next step (Fig. 4.2(c)). In detail, the algorithm of the reordering first picks up the station pair with the maximum waveform coherence to form a subgroup. Then it iteratively selects the most coherent station pair in the remaining station pairs. The selected station pair forms a new group if neither of the stations is in existing groups. Otherwise, the new station joins in the existing group where the other station is already in. Finally, the groups are combined according to how coherent between groups. After we get the correlation matrix with new station order for a sub-array, we search all possible selection squares within the matrix image and then find the largest selection square in which each value is larger than the cross correlation threshold, which is 50% of the average CC in the sub-array (black box in Fig. 4.2(c)).

The purpose of using such relative CC thresholds is to balance the data quality and the numbers of remaining stations in each sub-array. We perform a test using the same absolute CC threshold (0.1, the lowest CC threshold among all the used sub-arrays for the Mw 7.1 earthquake) for all sub-arrays. The result shows no significant difference with that using relative CC threshold. Finally, we remove the sub-arrays with fewer than 8 coherent stations.

The short-period stations are complementary to the strong-motion ones in terms of their northeastward azimuthal coverage. They naturally form three closely spaced sub-arrays (Fig. 4.2(a)), with similar sizes (90 to 200 km) and azimuthal ranges (36 to 46°) to the strong-motion sub-arrays. Since the BP is performed separately for the strong-motion and the short-period sub-arrays, we choose not to remove the station response to avoid the amplification of the long-period noise. Because of the limited number of short-period stations, we remove stations with low signal-to-noise-ratio manually instead of automatically picking stations according to the coherence.

For the Mw 7.1 earthquake, we originally obtained 13 strong-motion sub-arrays (C1 to C13) and 3 short-period sub-arrays (C14 to C16) (Fig. 4.2(a)) after applying the automatic clustering algorithm. C1 and C10 are removed because their number of coherent stations is smaller than 8. C11, C12, C14, and C15 are removed because of their low waveform coherence due to the sparse station distribution and the proximity to the nodal plane. For the Mw 6.4 earthquake, we obtain 14 strong-motion sub-arrays (D1 to D14) after applying the automatic clustering algorithm. We then remove D1, D10, D11, D12, D13, and D14 because the number of coherent stations is less than 8 in each group. We adopt two short-period sub-arrays (D16 and D17), excluding D15 due to low SNR and strong coda waves.

We filter the vertical component of the waveforms to the frequency band between 0.1 to 2 Hz and use a running time window t_1 ranging from 6 – 10 s with an interval of 0.5 s (Most of the windows are overlapped). We choose the highest frequency bands and the shortest running time window t_1 that yield stable and concentrated BP peaks in slowness diagrams of each sub-array. To validate the combination of the BPs from different frequency bands across the subarrays, we conduct a synthetic test either using uniform or non-uniform frequency bands. The tests show that both the uniform and non-uniform frequency bands produce results that are close to the input model. We also validate our choice of frequency bands and the combination of acceleration and velocity data.

We perform a grid search of the slowness vector and identify the back-azimuth corre-
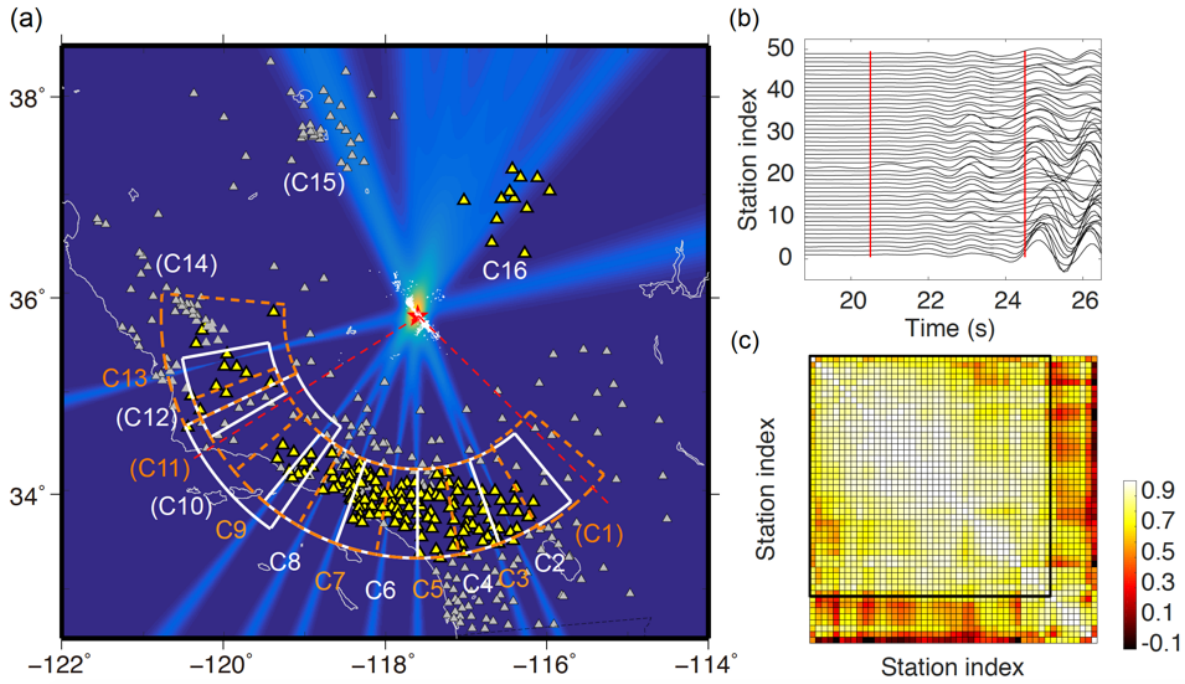
Figure 4.2: Concept, array configuration, and waveform-coherence-based station grouping strategy of the MLBP method (the Mw 7.1 Ridgecrest earthquake). (a) The background color indicates the distribution of joint spatial probability of the source location at the origin time of the Mw 7.1 Ridgecrest earthquake determined with MLBP using C2 - C9, C13, and C16. The red star is the epicenter. The red dashed lines are the nodal planes of the Mw 7.1 event. The orange dashed lines and the white lines delineate the fan-shaped sub-arrays. The grey triangles are the available stations. The yellow triangles are final stations chosen for MLBP. The texts in parenthesis denote sub-arrays that are not used. (b) Waveforms of the Mw 7.1 event recorded by all available stations in C4 (before station selection using the K-nearest-neighbor algorithm). The red lines show the waveform segments used to calculate the cross-correlation coefficient (CC). (c) The CC matrix of all pairs of stations of C4. The stations are reordered using "corrmap", a subroutine based on the k-nearest neighbor algorithm using waveform coherence, so that the neighboring-index stations are grouped into coherent sub-sets). The black box delineates the chosen subset with mutual coherence larger than 0.37, 50% of the average CC in C4.
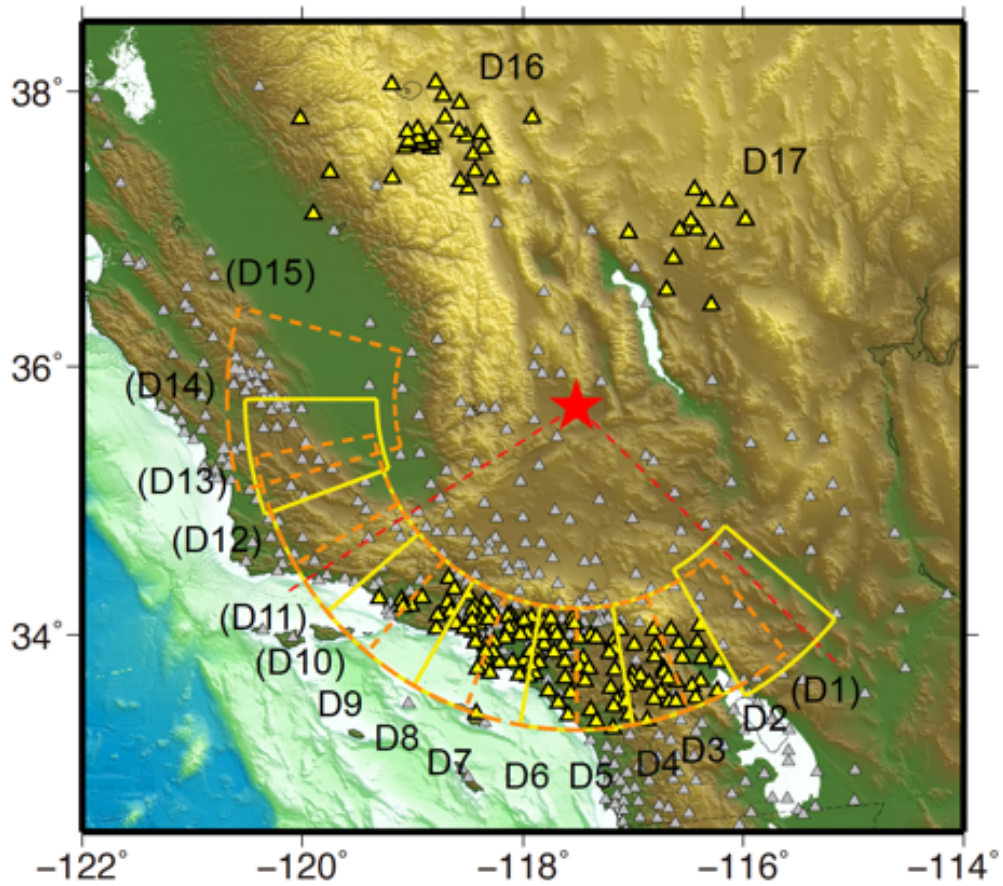
Figure 4.3: The array configuration of the MLBP of the Mw 6.4 event. The background color indicates the topography. The symbols are the same as Fig. 4.2

sponding to the peak stacked coherence for each sub-array. We apply a static correction of the back-azimuth ranging from -5 to 10° so that the first radiator is located at the epicenter. We validate that this correction is applicable to the whole source region by examining the deviations of the MLBP-measured back-azimuths from the reference values of 14 aftershocks (M 4 to 5.5) of the Mw 7.1 event (Fig. 2.7) from the relocated catalog (H. Huang et al., 2020). We use the same array configuration for the Mw 7.1 earthquake to calculate BPs for each aftershock using a frequency band of 0.08 to 0.8 Hz and a window of 10 s. If we use the same frequency bands as the Mw 7.1 earthquake, the signal to noise ratio and the coherence will be too low to get concentrated BPs. So we use a slightly lower frequency band for the aftershocks. For each aftershock, we measure the back azimuths of the waveforms in the 10 s sliding windows with an interval of 0.5 s starting from the P arrivals. In Fig. 2.7(d), we show that the biases are not dependent on the location on the fault. So we apply a uniform correction along the strike of faults.

We estimate the parameter σ_k in equation 2.2 to be 2° based on the uncertainty of the back-azimuths of 14 M 4 to 5.5 aftershocks observed at C2 to C6 (Fig. 2.7 (a) and (c)). Such level of uncertainty in back-azimuth transfers to approximately 7.7 to 11.4 km of along-strike distance error for sub-arrays oriented 45 to 90° from the fault strike direction of the Mw 7.1 earthquake (e.g. C5 to C14 and C16), which is small compared to the length scale of the Mw 7.1 mainshock (about 40 km). Since the signal-to-noise ratio (SNR) of the aftershocks is not sufficiently high for estimating σ_k at C7 to C9 and C13, we adopt a uniform σ_k of 2° for all sub-arrays. We show that σ_k of 1° and 3° do not alter our results significantly.

To synchronize different clusters, we need to estimate t_{0_k} in equation 2.2, the arrival time of the used phase at the reference station of each cluster. We utilize the dominant P phases at the epicentral distance of 2° (about 222 km), which are a group of crustal phases, composed of PmP, Pg, PConradP and Pb (Fig. 2.4) with an apparent slowness of about 0.15 s/km (Fig. 2.6, Fig. 4.4). These dominant phases are not always the first arrivals. Using 1-D Southern California velocity model (SoCal) (Hadley & Kanamori, 1977), we calculate

the first P arrival times for each sub-array assuming the National Earthquake Information Center (NEIC) epicenter locations of 117.599°W, 35.770°N and 117.504°W, 35.705°N, and hypocentral depths of 2 km (following H. Huang et al. (2020)) and 10.5 km for the Mw 7.1 and Mw 6.4 earthquakes, respectively. Then we search for the arrival times of the dominant P phase from 10 s before the theoretical first P arrival times. In the northern sub-arrays (C7 to C9, C13, and C16), the first resolved radiators correspond to a group of crustal phases and t_{0_k} can be determined by picking the first robust radiator around the theoretical arrival time (Fig. 4.4). For the sub-arrays to the southwest (e.g. C2 to C6) (Fig. 4.4), the radiators associated with crustal phases are overtaken by the radiators associated with mantle phases for several seconds possibly due to variations of 3D velocity structure or different BP resolvability. These two groups of phases are separated clearly in apparent slowness (about 0.12 s/km for the mantle phase and about 0.15 s/km for the crustal phases) (Fig. 2.6, Fig. 4.4) when data quality is high. In this case, we determine t_{0_k} based on the first robust radiator in the second group of slowness peaks corresponding to the crustal phases.

4.3 Result

4.3.1 The Mw 6.4 earthquake

The results of the MLBP (Fig. 4.5(a) and (c)) show that the Mw 6.4 earthquake broke an 8-km-long NW-trending segment in the first 7 s before rupturing the primary SW-trending fault for 15 km from 7 to 11 s. The 15 km rupture length on the SW branch is consistent with the aftershocks and fault traces (Fig. 4.5(a)). The average rupture speed on the SW-trending segment is about 1.3 km/s. The observed 8-km-long northwestward rupture is similar to that estimated by Yang et al. (2020). The radiators' locations are consistent with the subevent inversions (Jia, Wang, & Zhan, 2020), where the estimated duration is about 10 s.
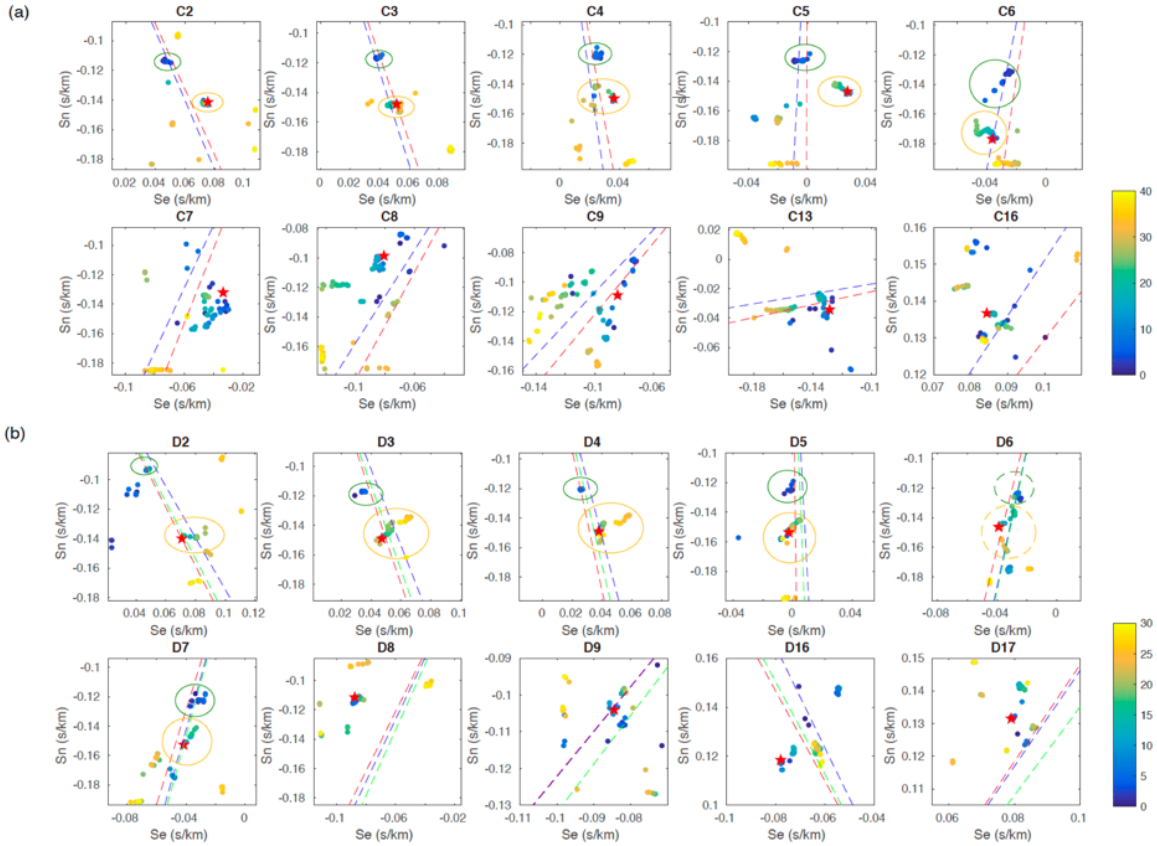
Figure 4.4: BP results from individual sub-arrays for the Mw 6.4 (a) and the Mw 7.1 (b) earthquakes, color coded by time from theoretical first P arrival. Each dot is the peak location in the slowness image for a given time step. The star shows the manually picked initial rupture resolved by the dominating crustal phases. The ellipses show the mantle (green) and crustal (yellow) phases that clearly separate or can be distinguished with less confidence (dashed ellipse). The straight dashed lines are the theoretical back-azimuths of reference source locations. In (a), the red, green and blue dashed lines correspond to the epicenters of the Mw 6.4 event and the Mw 7.1 event (a reference for rupture on the NW branch), and the end of the SW segment of the Mw 6.4 event, respectively. In (b), the red and blue dashed lines are the back-azimuths of the epicenters of the Mw 7.1 and Mw 6.4 events, respectively.
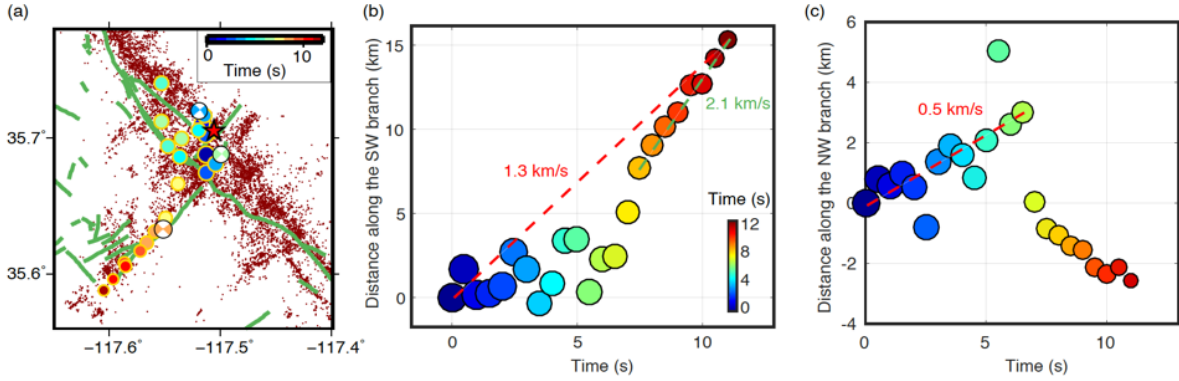
Figure 4.5: MLBP result of the 2019 Mw 6.4 Ridgecrest earthquake. (a) Rupture process of the Mw 6.4 event imaged by MLBP using 10 local seismic sub-arrays (D2 to D9, D16 and D17). The small red dots denote aftershocks detected and relocated by H. Huang et al. (2020). The beachballs show the subevent focal mechanisms inverted by Jia et al. (2020) color-coded by time. The green lines are Quaternary fault traces and surface rupture traces (Milliner & Donnellan, 2020). (b) The relation between distance along the SW fault (strike angle: 226.2°) and time of the seismic radiators. The red lines show the reference rupture speed of 1.3 km/s, which is a lower bound of the average rupture speed, assuming the rupture starts from the origin time. The green line shows the reference rupture speed of 2.1 km/s for the last 5 s, which is well constrained because the energy is mainly released from the SW fault after 8 s. (c) The relation between distance along the NW fault (strike angle: 320°) and time of the seismic radiators. The red line shows the reference rupture speed of 0.5 km/s for the NW fault, which is probably underestimated due to a lack of constraints.

4.3.2   The Mw 7.1 earthquake

For the MLBP of the Mw 7.1 earthquake, Fig. 4.6 shows that the rupture of the Mw 7.1 earthquake extends bilaterally along the fault trace for 10 km and 20 km at the speed of 1.1 to 1.6 km/s on the NW and SE branches of the fault, respectively. However, Fig. 4.7 shows that C4 and C16 resolve two simultaneous rupture fronts after about 8 s. C16, which is in the perpendicular direction to the fault strike thus has a high spatial imagining resolution along the fault, clearly shows the bilateral propagations in both the NW and SE directions: a persistent northward rupture front from 0 to 18 s, and a southward rupture front from about 8 to 20 s.

4.4   Discussion

4.4.1   Bilateral ruptures

The Ridgecrest earthquake sequence provides an interesting opportunity to examine particularities of imaging relatively small bilateral ruptures with BP techniques. For the Mw 7.1 earthquake, the MLBP result show successive rupture propagating to the north for about 10 km in the first 10 s and then southward for about 30 km in the next 10 to 15 s. However, C16 resolves two simultaneous rupture fronts propagations in both the NW and SE directions from 8 s to about 15 s (Fig. 4.7). The separation of the bilateral fronts may have started but was below the resolution limit before 8 s because the two bilateral fronts are too close to each other. In that situation, MLBP only resolved one single location representing the average location of the two rupture fronts, possibly closer to the stronger one. The rest of the sub-arrays are either less optimally oriented or lack enough coherence and station density to image the bilateral ruptures. To increase the reliability of the results, we only pick one maxima on the merged MLBP diagram for each time step. So the merged MLBP traces only the stronger of the bilateral rupture fronts, which appeared first northwestward and
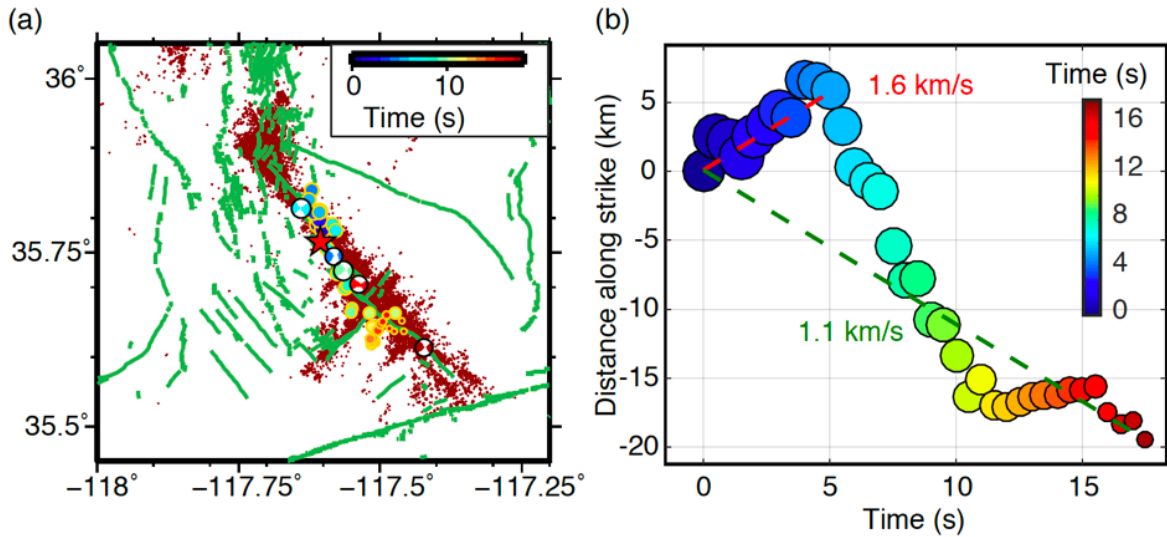
Figure 4.6: (a) Seismic radiators inferred by MLBP of the Mw 7.1 event using 10 local seismic sub-arrays (C2 to C9, C13, and C16) color-coded by time. The small red dots are aftershocks detected and relocated by H. Huang et al. (2020). The beachballs show the subevents inverted by Jia et al. (2020). The white lines are Quaternary fault traces and surface rupture traces (Milliner & Donnellan, 2020). (b) The relation between the along-strike (320°)(Jia et al., 2020) distance and time of the seismic radiators. The red and green lines show reference rupture speeds for the NW and SE segments.
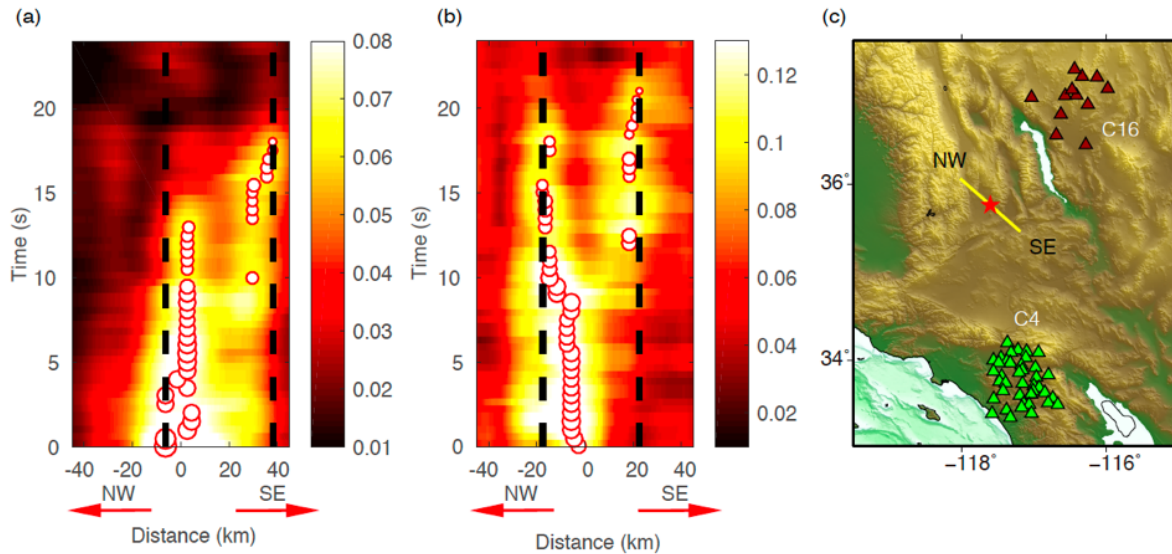
Figure 4.7: The projected BPs on the fault plane for the Mw 7.1 earthquake using (a) C4 and (b) C16. The abscissa is the distance along the fault assuming a strike angle of 320° (Jia et al., 2020) (yellow line in (c)) where negative and positive directions are towards NW and SE from the epicenter. The rupture lengths are 6 km to the northwest and 38 km to the southeast for C4, 17 km to the northwest and 23 km to the southeast for C16. (c) The configuration of C4 and C16.

then southeastward. The apparent high rupture speed of about 4 km/s during the transition around 5 to 10 s is more likely to be artificial because of switching between the primary rupture fronts (Fig. 4.6) according to the synthetic tests. Therefore, we estimate the speed of the southeastward rupture to be 1.1 to 1.3 km/s, assuming that the rupture started from the epicenter at the origin time. However, we can not completely rule out the possibility that the back-propagation and high apparent rupture speed are real. One possible scenario involves interactions and triggering between the M 6.4 and M 7.1 events. The transition zone between the NW and SE rupture areas is overlapping with the part of the rupture zone of the M 6.4 event (initial NE rupture branch) and possibly its post seismic slip or afterslip. If this zone was already ruptured (and hence was considered as in turn "mature" fault for the M 7.1 rupture), the M 7.1 rupture could have easily propagated without consuming much inelastic energy, resulting in faster rupture speed. With the same logic for interpreting the slow rupture speed and the fault immaturity (see later sections), the apparent fast rupture speed can possibly be made and promoted by the Mw 6.4 rupture. Or, alternatively, the migration of radiators in-between 5 to 10 s is not a continuous rupture, but is rather a static/dynamic triggering of rupture. The bilateral rupture is consistent with the slip model inferred from geodetic data by K. Chen et al. (2020), which shows a crack-like rupture propagation in the first 11 seconds both to the NW and SE.

Similar to the Mw 7.1 event, although the seismic radiators of the Mw 6.4 earthquake on the SW branch first appeared at 7 s, the rupture on that branch was likely to have started earlier and was masked by the stronger NW front. Because the separation of the two rupture fronts are smaller than the imaging resolution and the merged MLBP are tracing the stronger one. The bilateral rupture also presents a challenge in locating sources. The timing of the switching from primary rupture fronts is slightly different at sub-arrays of different azimuths due to radiation pattern and the directivity effect. In this case, the merging processing might intersect the source back-azimuths from different rupture fronts, which leads to source location errors. However, such a scenario often results in artificial sources far away from the

main fault plane. In our case study of the Ridgecrest sequence, we manually inspected the merging process by checking the snapshots of the joint spatial probability images and made sure such artifacts are not present in our final result. Collectively, the rupture speeds for the segments that are influenced by bilateral rupture have large uncertainties.

4.4.2   Comparisons with previous source analysis

The bilateral rupture processes of the two earthquakes resolved by SEBP and MLBP are consistent with previously published finite fault models (K. Chen et al., 2020; K. Wang et al., 2020). K. Wang et al. (2020) combine geodetic and seismic data to invert for the kinematic rupture model of the Mw 6.4 and Mw 7.1 earthquakes using a multiple time-window approach which allows the temporal variability of rupture velocity and rise time. Their preferred slip model for the Mw 6.4 earthquake shows a strong energy radiation from the NW branch in the first 5 s. The major asperity on the SW branch, which is more than 5 km away from the hypocenter, started to rupture around 4 s. For the Mw 7.1 earthquakes, K. Wang et al. (2020) show that the rupture was bilateral but the southward rupture is weak at the beginning and slightly delayed. This is consistent with our BP result from C16 (Fig. 4.7(b)) and our interpretation that the apparent back-propagation and the fast rupture speed around 5 to 10 s resolved by MLBP are artificial due to the transition from the NW branch to the SE branch (Fig. 4.6(b)). Yang et al. (2020) applied a multi-azimuth back-projection with regional seismic data to the Ridgecrest earthquake sequence according to the travel time table determined with a 3D regional velocity in California (G. Lin et al., 2010). Their results show that the rupture for the Mw 6.4 earthquake propagates to the NW branch at the first 8 s and then to the SW branch around 10 to 14 s, which is consistent with our observation. Their BP results for the Mw 7.1 earthquake show a northward propagation from 0 to 8 s, and an apparent back propagation from 8 to 18 s, which is similar to our BP results.

The results of MLBP show several new features for the rupture process of the Mw 7.1

earthquake, including the deceleration around 10 to 15 s and the accelerates during 15 to 20 s, possibly related to a geometrical barrier due to fault complexity near the intersection of the SW and NW segments. The MLBP method provides independent evidence for a simultaneous bilateral rupture propagation for the Mw 7.1 earthquake. The BP results are made without any assumptions of fault geometry, which thus should be useful to evaluate the assumption of the fault geometries used in the previous studies (e.g. Ross et al., 2019; K. Chen et al., 2020; Goldberg et al., 2020).

4.4.3   Rupture speed and its relation with immaturity

The rupture speed is estimated to be about 1.3 km/s for the Mw 6.4 earthquake and 1 to 1.6 km/s for the Mw 7.1 earthquake, close to but slightly lower than the previous estimates based on subevent inversions and finite fault modeling, which are around 1.5 to 2 km/s (e.g. Ross et al., 2019; C. Liu et al., 2019; K. Wang et al., 2020). There are several factors that contribute to the underestimation of the rupture velocity. Firstly, the same reasons for the underestimation of rupture length (discussed in the next section) leads to the underestimation of the average rupture speed. For example, the NW branch of the Mw 6.4 earthquake has a possibly underestimated rupture length of about 4 km possibly due to the biased array distribution and bilateral rupture, which leads to the extremely low rupture speed of 0.5 km/s (Fig. 4.5 (c)). Most of the arrays are to the southwest of the epicenter, so the observed BP power from the NW branch is weak due to the directivity effect. The second reason is the weak constraint on the location and timing of rupture initiation on the SW branch of the Mw 6.4 earthquake and the SE branch of the Mw 7.1 earthquake due to the masking of the rupture on the dominating branch. The estimation of 1 to 1.6 km/s for the rupture speeds of the two earthquakes is based on the assumption that the ruptures on all branches initiate from the epicenter, which is a lower bound of the average rupture speed. If the rupture speed is fit to a particular segment of the rupture, for example, assuming the rupture starts on the SW branch for the Mw 6.4 earthquake with a delay, the rupture velocity

is higher (2.1 km/s) (Fig. 4.5(b)). The third problem is the ambiguity of rupture time due to the relatively long BP time window (about 10 s) compared with the source duration (10 s and 18 s), which causes the smearing of timing of the rupture and artificially increases the rupture duration. For example, when the center of the BP time window is around 5 s before the Mw 6.4 earthquake initiates, the first sliding window already contains the radiation from the epicenter.

Despite these uncertainties, an overall rupture speed between 1 to 2 km/s seems to be a common feature shared by previous studies and this one. Such speed is relatively low compared with the shear wave velocity of about 3.2 km/s (between 1.9 and 8 km depth) (K. Wang et al., 2020), which is attributed to the immaturity of the fault system (Perrin, Manighetti, Ampuero, Cappa, & Gaudemer, 2016; Goldberg et al., 2020; K. Wang et al., 2020). An immature fault is typically associated with a slip rate smaller than 1 cm/yr, a length shorter than 300 km, and an age less than a few Ma (Manighetti, Campillo, Bouley, & Cotton, 2007). The fault system hosting the Ridgecrest earthquake sequence satisfies these criteria, with a fault length of about 50 km, a long-term slip rate of 0.49 mm/yr (Oskin & Iriondo, 2004), and a current slip-rate of 7 mm/yr (Peltzer, Crampé, Hensley, & Rosen, 2001). The segmentation of the primary fault plane, the large-scale networks of secondary branches revealed by the relocated aftershocks (Ross et al., 2019), and the low radiated energy are all characteristics that are consistent with the immaturity of the fault system (C. Liu et al., 2019). The correlation between low rupture speed and fault immaturity can be explained with a simple energy-budget argument. The fracture energy and fault roughness are greater in an immature fault system because the interface contacts are not yet broken and smoothed off. Compared with the case of a mature fault system, more energy is consumed to form new fault surfaces and off-fault cracking, and is dissipated by various thermal processes in an immature fault system (Perrin et al., 2016). Assuming the constant stress drop and hence constant released strain energy, the fracture-to-strain-energy-ratio is larger for immature faults, which hinders acceleration to high rupture speed. MLBP result

of the Mw 7.1 earthquake shows that the propagation of rupture toward the SE slows down around 10 to 15 s, and an accelerates during 15 to 20 s, possibly related to a geometrical barrier due to fault complexity near the intersection of the SW and NW segments.

4.4.4 Rupture length

The rupture length of the Mw 7.1 earthquake resolved by the MLBP method is about 10 km to the northwest and about 20 km to the southeast. This is slightly shorter than the surface rupture trace inferred from aftershock distribution (Fig. 4.6) and the slip model of K. Chen et al. (2020), where the estimated rupture length is about 20 km to the northwest and about 30 km to the southeast. It is likely that aftershocks and postseismic deformation had an extra contribution to the surface displacement. In the case of the MLBP, Fig. 4.8 (b) shows that most sub-arrays yield similarly short rupture length (about 10 km to the northwest and 20 km to the southeast). The underestimated rupture length could also be caused by the masking of the later part of the rupture after 16 s due to the domination of the coda wave and the contamination from the S wave. We found that most stations of the Mw 7.1 earthquake have a S-P travel time larger than 18 s. So within our analyzed time window, the effect of S wave can be neglected. But after 18 s, S waves start to arrive at some stations. So it is possible that the end of the P wave trains of the Mw 7.1 earthquake mix with and are then overtaken by the S wave if the rupture duration is larger than 18 s.

4.4.5 Effect of lateral velocity variation

It's worth noting that an accurate 3D velocity model can improve the arrival time estimate and hence reduce the back-azimuth bias. Yang et al. (2020) applied a multi-azimuth back-projection with regional seismic data to the Ridgecrest earthquake sequence according to the travel time table determined with the California Statewide Three-Dimensional Seismic Velocity model (G. Lin et al., 2010). Their BP images show strong source radiation close

70
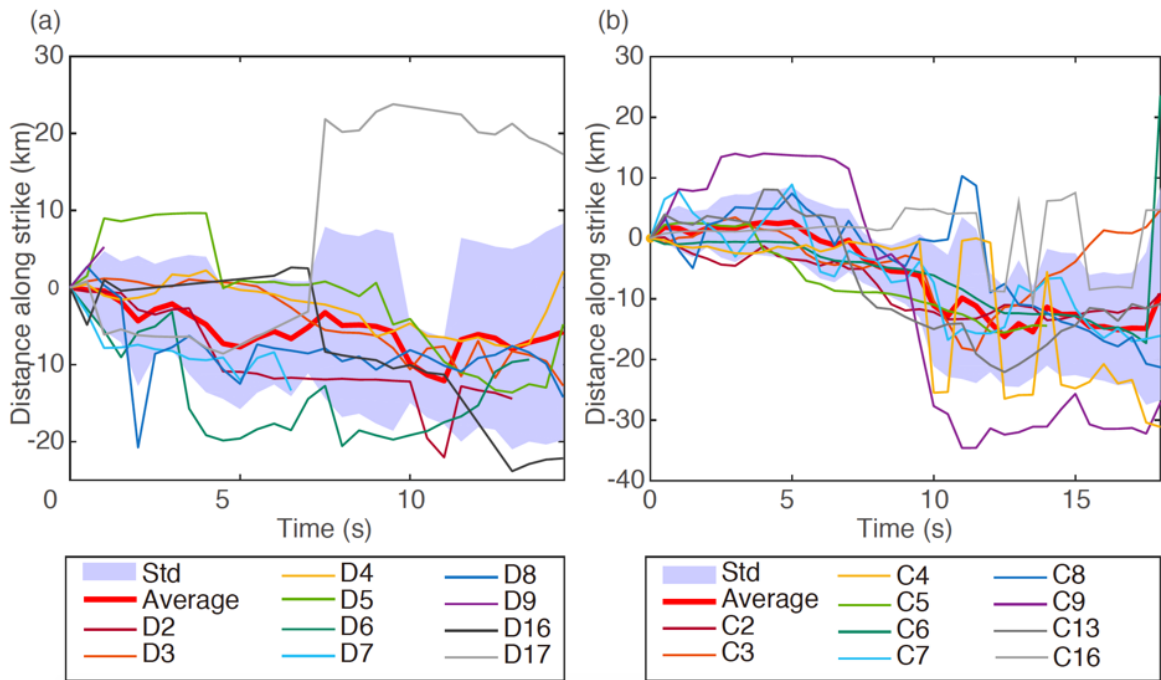
Figure 4.8: Rupture length (along strike distance) as a function of the time imaged by individual sub-arrays. The rupture length is estimated by intersecting the back-azimuths of individual sub-arrays with the fault trace of the SW branch for the Mw 6.4 (a) and the Mw 7.1 (b) earthquakes. The shaded zones show the ranges of one standard deviation of the locations along strike. The maximum, minimum, and average of the deviation from 2 to 13 s for the Mw 6.4 earthquake are 13.2, 2.5 and 8.22 km, respectively. For the Mw 7.1 earthquake from 2 to 17 s, these values are 12.4, 3.7 and 7.6 km, respectively. The curves of C4 and C16 are less smooth than other sub-arrays. The resolved slownesses (maxima of the slowness diagrams) come from one of the rupture fronts, which switches between the NW and SE branches. The scattering at 0 s is small because the static calibration is based on the first radiator. We remove the outliers with deviation larger than 25 km and 35 km for the Mw 6.4 and the Mw 7.1 earthquakes.

to the fault traces, and the inferred rupture process is overall consistent with this study. It is worth noting that Yang et al. (2020) adopted the travel times of the first-arrival, which does not necessarily correspond to the dominant one among the overlapping phases. For the sub-arrays in the southwest (e.g. C2 to C6 and D2 to D7), we find that the first arrivals are the mantle phases signals dominating only the first ~ 6 s before the stronger crustal phases arrive. A potentially more suitable method to take advantage of multiple overlapping phases is the adjoint source inversion (Somala, Ampuero, & Lapusta, 2018; Zhou, Meng, Xie, & Han, 2019), which reconstructs the source kinematics by back-propagating the full wave-field containing all seismic phases. Both the BP and adjoint source inversion can be easily automated given the prior knowledge of the velocity structures. However, since the accurate fine-scale 3D tomography is only available for well-studied areas, we consider that MLBP with empirical aftershock calibrations is more universally applicable.

4.4.6 The potential for real time implementation

Our result shows that the MLBP method can be used for rapid hazard assessment using the existing network in California. The Ridgecrest sequence demonstrates the rupture process of moderate to large earthquakes (M 6+) with rupture length >10 km can be resolved in near real-time using stations located between $1.5°$ and $2.5°$ (166 to 277 km) from the epicenter. The automatic clustering of stations based on waveform coherence is similar for the Mw 6.4 and the Mw 7.1 events. To image future earthquakes in real-time or post-event analysis, the station sub-arrays can be predetermined according to the waveform coherence as well as the source locations and focal mechanisms (the sub-arrays close to the nodal planes need to be removed). The point-source parameters can be provided by the standard early warning system (e.g., Elarms, (Allen, 2007)). The rupture termination can be evaluated based on the spatial deviation of source location in our MLBP algorithm(Fig. 2.9), which may also be a critical information when issuing an early warning. Taking into account the earthquake duration of about 20 s and the P phase travel time of about 50 s

(for stations located about 2.5° or 277 km in epicentral distances), characterization of the earthquake size, directivity, and speed in the Ridgecrest scenario can be achieved within 70 s from MLBP. The MLBP approach has the potential to be incorporated into the current system for real-time earthquake monitoring and rapid hazard assessment.

4.5   Conclusion

We improve the MLBP by grouping coherent station sub-arrays using the existing seismic network located between 1.5° and 2.5° (166 to 277 km) from the epicenter and performing empirical aftershock calibrations to reduce the slowness bias caused by the horizontal velocity variation, which is applicable to regions without explicit knowledge of 3D velocity structure. These improvements decrease the uncertainties of the back-azimuth to 2° (corresponds to along-strike lengths of 8 km in the source region) and enabled MLBP to resolve a M 6+ earthquake. We apply MLBP to the dominant crustal P phases to image the Ridgecrest mainshock rupture processes. Our results indicate the Mw 6.4 quake initiated on an 8-km-long NW-trending segment, before rupturing the primary SW-trending fault at a low speed of about 1.3 km/s. The Mw 7.1 quake extends bilaterally for 10 km and 22 km, on the NW and SE portions of the fault, respectively, at a speed of 1 to 1.6 km/s. The rupture path agrees with the aftershocks and the surface rupture trace inferred by pixel correlation of the Sentinel-2 optical images. The low rupture speeds of the two earthquakes are explained by the fault immaturity manifested by the fragmentation of the newly developed Ridgecrest fault system, linking the Little Lake and the Airport Lake faults to the north and the Blackwater fault to the south. The results of MLBP show several new features for the rupture process of the Mw 7.1 earthquake, including the deceleration around 10 to 15 s and the accelerates during 15 to 20 s, possibly related to a geometrical barrier due to fault complexity near the intersection of the SW and NW segments. The MLBP method provides independent evidence for a simultaneous bilateral rupture propagation for the Mw 7.1 earthquake. The

BP results are made without any assumption of fault geometry. The sources of relatively high frequency radiation are complementary to previous studies and more related to strong motion generations (Meng et al., 2014; Feng & Meng, 2018). The choice of the array configurations (size, distance range) and processing parameters (frequency, window length) can be used to optimize future applications of earthquake source imaging. The information of the seismic source can be achieved in a short time (70 s for the Mw 7.1 earthquake), which makes it a potential method for rapid hazard assessment.

CHAPTER 5

Multi-array back-projection of teleseismic arrays and its application to the 2021 Mw 7.3 East Cape, New Zealand earthquake

Abstract

In this chapter, we apply the multiple-array back-projection to teleseismic array to resovle the 3D locations of sub-sources of the 2021 Mw 7.3 East Cape, New Zealand earthquake occurred at the southern end of the Kermadec Trench. Due to the limited azimuthal coverage and low density of local seismic stations, we choose to use teleseismic arrays to study the Mw 7.3 earthquake. For individual teleseismic arrays, there is a strong trade-off between depth and horizontal direction. The combination of the BPs of multiple arrays improves both depth and horizontal resolution. Our back-projection results reveal a bilateral rupture predominantly propagating upward at a slow speed of 0.98 km/s and a triggered rupture at a depth of ∼10 km, corresponding to the deep reverse faulting event at a depth of ∼70 km and a triggered shallow normal faulting event (about 20 km) resolved by a subevent inversion and finite fault inversion (Okuwaki et al., 2021). The rupture of multiple faults with different orientation could explain the USGS W-phase solution, which shows that the rupture lasted for about 50 s involving oblique reverse faulting striking in the east-west direction. Such a focal mechanism is not expected in this region, since most historical earthquakes are normal faulting events striking in the northeast-southwest direction. The rupture on two distinctive fault planes is possibly explained by the thick subducting buoyant

oceanic plateau with widespread seamounts at East Cape. These seamounts are thought to produce complex fracture networks and favor small earthquakes or aseismic slip due to the fluid-rich sediments and granular bands. The large earthquakes such as the M 7.3 event occur only when multiple small fractures coalesce, linked by static or dynamic triggering (K. Wang & Bilek, 2011). The epicenter and a group of aftershocks are deeper than the bottom of the slab according to a regional tomography model. Such deep failure is possibly enabled by a delaminating lower crust of the Hikurangi plateau.

This is an collaborate work. I am the first author to conduction 3D back-projection, calculate the static and dynamic stress and write the paper. The manuscript is in review. Tong Zhou contributes the discussion about the delamination. Han Bao and Liuwei Xu provide the preliminary result of the back-projections using individual arrays.

5.1 Introcution

On March 04, 2021, a Mw 7.3 earthquake (Fig. 5.1) occurred approximately 182 km to the northeast of the city of Gisborne, at the southern end of the Kermadec Trench, where the Hikurangi Plateau underthrusts beneath the Australian plate. The Mw 7.3 event is followed by two larger Mw 7.4 and Mw 8.1 quakes about 4 hours later about 800 km to the north. The thickness of Hikurangi Plateau is approximately 12 - 15 km (the average thickness of Pacific oceanic crust is 8 km), close to the critical thickness (17 km) where buoyancy switches from driving to resisting subduction (Collot & Davy, 1998). Due to the thickening of the oceanic plate and the increasing obliquity from north to south, the convergence rate decreases from 6.3 cm/yr near 30°S to 4.9 cm/yr at 37°S. The subduction stops around 44° S, where the Chatham Rise indicates the transition from oceanic to continental crust of the Pacific plate. The obliquity in the Hikurangi trench causes a slip-partitioning motion with the trench-parallel motion accommodated by strike-slip faulting and the rotation of the eastern North Island arc (Wallace, Beavan, McCaffrey, & Darby, 2004; Wallace & Beavan, 2010).

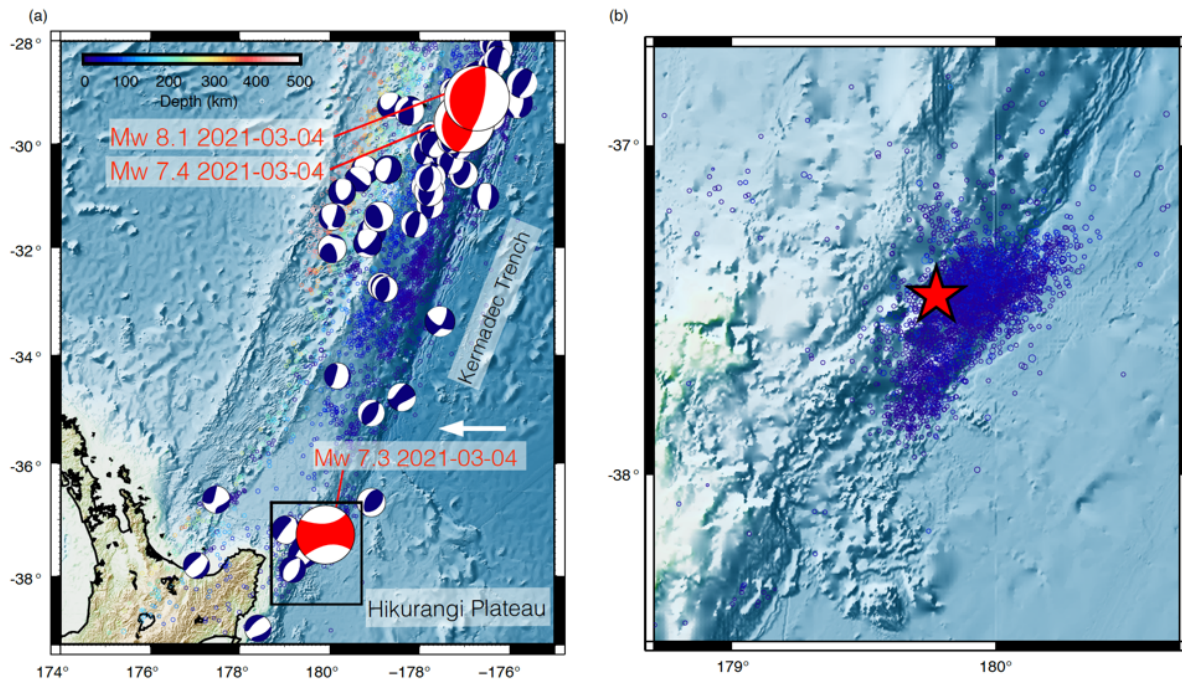Figure 5.1: Tectonic background of the Kermadec subduction zone and the seismicity near the Mw 7.3 earthquake. (a) The small circles are the EHB catalog of M 4.5+ from 1/15/1964 to 12/13/2017, color coded by depth. The beachballs are the CMT solution of M 6.5+ events (GCMT) from 1/1/1979 to 2/1/2021. (b) The aftershock distribution from Geonet catalogue. The range of the map is shown by the black box in (a).

There have been several Mw 6.5+ historical normal-faulting earthquakes but few large megathrust earthquakes around the source region of the 2021 Mw 7.3 earthquake. The only two recorded large interplate thrust earthquakes along the Hikurangi subduction zone are the 1947 Mw 7.1 Poverty Bay earthquake and the 1947 Mw 6.9-7.1 Tokomaru Bay earthquakes. Both of them are tsunamigenic with long source duration (about 40 s) and slow rupture speeds (about 1 km/s). They produced disproportionately large tsunamis for their magnitudes (Doser & Webb, 2003). The lack of large megathrust events in this region can be explained by the small interseismic plate coupling coefficient of about 0.6 at seismogenic depth from 0 to 10 km inferred from GPS studies (Wallace et al., 2004; Wallace & Beavan, 2010). The plate convergence seems to be accommodated by repeating aseismic slow slip events, often found at the depth of 6 to 15 km, which marks the transition from the interseismic coupling and the deeper stable slipping portion of the plate interface (Wallace & Beavan, 2010). The most recently reported slow slip episodes, detected both before and after the 2016 Mw 7.0 earthquake, partially overlapped with the source area of the 2021 Mw 7.3 earthquake.

The Mw 7.3 earthquake is unusual in several aspects. The rupture lasted about 50 s according to the USGS earthquake W-phase inversion, significantly longer than about 25 s for typical earthquakes of similar magnitudes (Ye, Lay, Kanamori, & Rivera, 2016). The focal mechanism is predominantly oblique-reverse, striking in the east-west direction where the historical M 6+ earthquakes are mostly normal-faulting events. The W-phase solution also suggests a 20% non-double couple component, which indicates that the earthquake ruptured multiple faults of different orientations. Okuwaki et al. (2021) conducted a finite fault inversion and a multiple point source inversion and concluded that this earthquake is composed of an initial subevent on an unexpected, deep trench-parallel compressional fault (50 to 100 km) and a second subevent on a shallow trench-normal extensional fault (0 to 30 km). The aftershocks span a large depth range from 0 km to 100 km (Fig. 5.4(c)), which extends to about 30 km below the bottom of the slab according to the tomography and the

background seismicity relocation result of Eberhart-Phillips and Bannister (2015). Intraplate earthquakes at these depths are rare because brittle frictional failure is prohibited by high pressure and temperature. The mechanisms for such intermediate-depth earthquakes (70-250 km deep) are under debate. The leading hypotheses are (1) Fluid-aided embrittlement or weakening (Halpaap et al., 2019). (2) Rapid strain in fine-grained shear zones results in thermal runaway and highly localized zones of viscous failure (Kelemen & Hirth, 2007).

Our aim is to resolve the details of the co-seismic rupture process of the Mw 7.3 earthquake and understand the cause of its source complexity. The rest of the article is organized as follows. We first describe the method and results of multi-array 3D back projection imagery of the mainshock, which shows rupture on multiple distinctive faults. We then investigate the static and dynamic stress transfer between the two subevents. Finally, we discuss the physical mechanisms of the deep ruptures and the triggering effects connecting the earthquake sequence.

5.2 Multi-array 3D back-projection using teleseismic arrays

Due to the limited azimuthal coverage and low density of local seismic stations, we choose to use teleseismic arrays to study the Mw 7.3 earthquake. We apply the Multi-taper 3D MUSIC Back-projection to resolve the spatial-temporal rupture process of the Mw 7.3 earthquake (Meng et al., 2011; Meng, Huang, Bürgmann, Ampuero, & Strader, 2015; Y. Chen, Meng, Zhang, & Wen, 2018). We performed the 3D MUSIC BP separately on the P-wave seismograms of four broadband seismic arrays, composed of 211 stations along the western coast of continental US (US), 87 stations in South America (SA), 133 stations in Australia (AU) (Fig. 5.2) and 254 stations in China (CN), respectively. We check the BP result using the initial 10 s of the Mw 7.3 earthquake for individual arrays. The initial rupture of an earthquake can be regarded as a point source. Inspecting its BP image helps to understand the blurry and aliasing effect. Fig. 5.3 shows that individual

arrays have limited spatial resolution, especially for depth. Fig. 5.3 shows that there is a strong trade-off between along depth and along N-S direction for the SA array, but the E-W direction is well constrained. For the AU array, the N-S direction is constrained better but the depth resolution remains low. The US array shows low resolution along the ray path due to its nearly linear configuration. Here, we combine BPs from individual arrays, which improves both depth and horizontal resolution (Fig. 5.3). Compared with single-array BPs, multi-array BPs enable higher spatiotemporal resolution and reduce false alarms in earthquake detection and location problems (Fan et al., 2018). The multi-array approach was also applied to improve stability and resolution of the BPs at local distances, where BPs of individual arrays may suffer large uncertainties due to crustal heterogeneities and simultaneous arrivals of multiple phases (Xie & Meng, 2020; Xie et al., 2021).

We first backproject the waveforms of individual arrays to a 3D source region surrounding the hypocenter. The imagery domain is 1 degree by 1 degree large, with the depth ranging from 0 to 140 km. We choose the highest frequency band with adequate waveform coherence for each network (We require the average interstation correlation coefficients larger than 0.85 in the first 10 s of the P wave). For all of the 4 arrays, we filtered the waveforms with a band-pass filter between 0.5 to 2 Hz. For each array, we aligned waveforms individually with a 6-second window centering at the P arrival using multi-channel cross-correlation to correct the travel time. The waveforms are back-projected to the source region in 10-seconds-long sliding windows with an increment of 1 second. We adopt the hypocenter relocated by Okuwaki et al. (2021) (-37.466N, 179.774E, 72 km). After we obtain the 3D back-projection images of the 4 arrays, we combine them by multiplying their MUSIC pseudo-spectrum at each grid in the source region. We normalize the BP results of each array by their maximum power during the mainshock so that the four arrays are equally weighted.
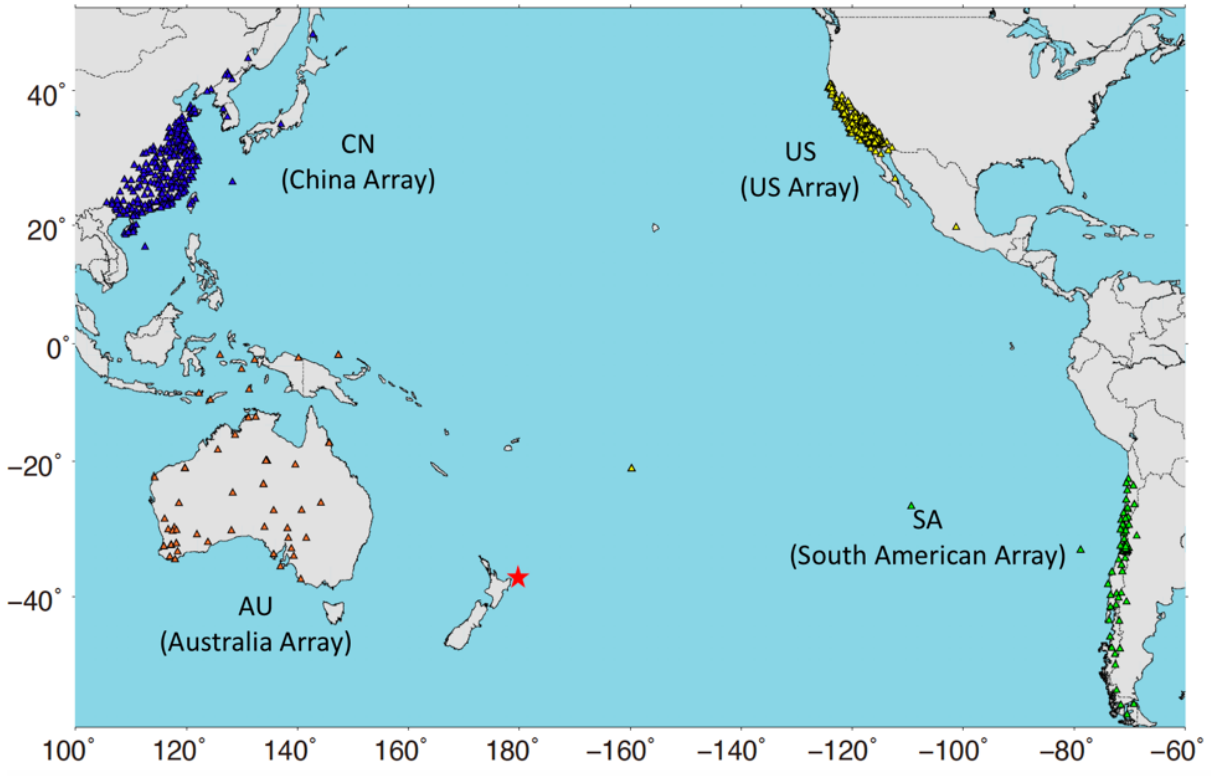
Figure 5.2: All available arrays within teleseismic distances: US array, South America network, China array and Australia network. The star is the epicenter of the Mw 7.3 earthquake from USGS.
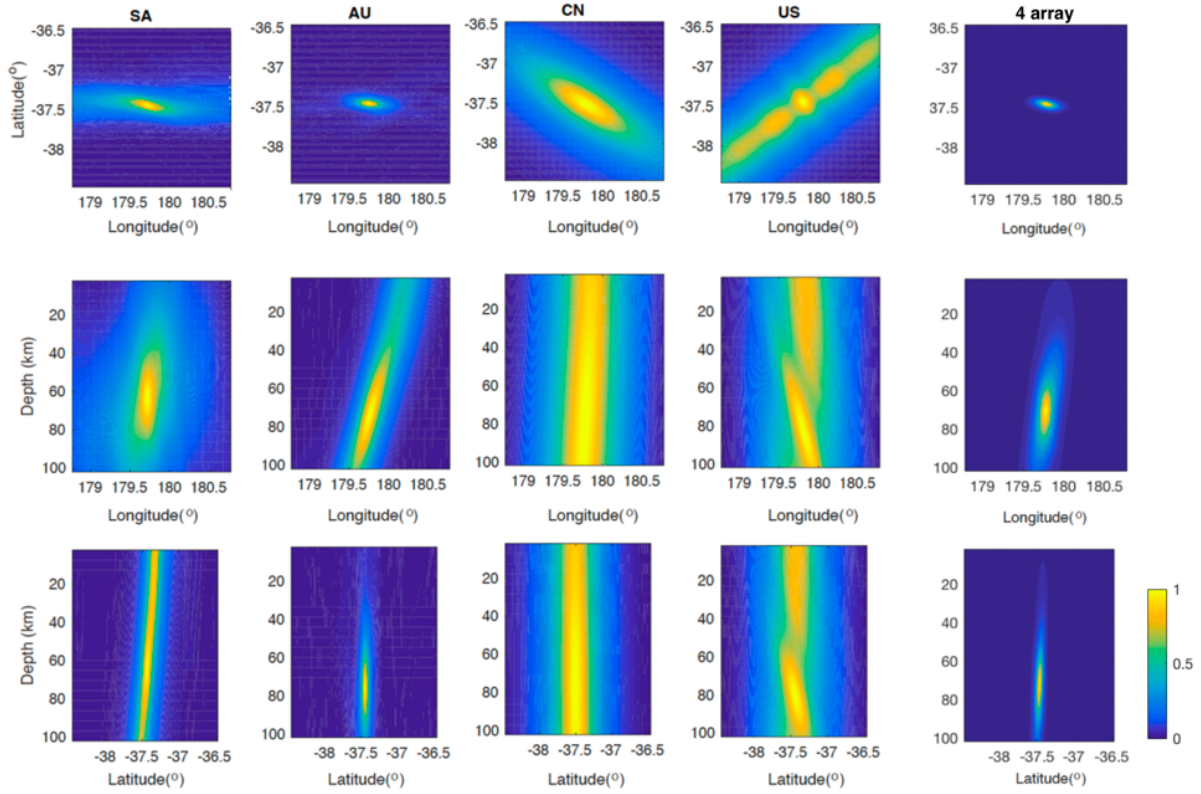
Figure 5.3: The BP result using the initial 10 s of the Mw 7.3 earthquake for individual arrays and multiple arrays. The three rows are the map view, cross section along longitude and the cross section along latitude, respectively. The columns from left to right are the results of the South America array, Australia array, China array, and US arrays. The last column is the results after combining the 4 arrays with the same weighting.

5.3   Result of back-projection

Fig. 5.4 shows the result of the combined teleseismic 3D BP using 4 arrays. Fig. 5.4(a) and Fig. 5.4(c) show the 3D locations of the high-frequency (HF) radiators, which are defined as the peak locations of BP images and could be viewed as the centroid locations of the rupture front at each time frame. Fig. 5.4(c) shows that the rupture mainly propagates upward, from a depth of 72 km to the surface but propagates horizontally by only about 20 km to the northeast. Fig. 5.4 (d)shows that in the first 20 s, the rupture propagates from depth D = 72 km to 40 km with a velocity of about 0.98 km/s. At T= 22 s, the main rupture abruptly splitted into two separated groups of radiators at D about 20 km and D about 80 km, possibly corresponding to simultaneous upward and downward propagating fronts, respectively. The BP-imaged bilateral propagation is grossly consistent in location with the rupture episode E1 to E4 in Okuwaki et al. (2021). The abrupt splitting of the main rupture fronts might be caused by the resolution limit of BP (Xie et al., 2021). It is likely that the bilateral fronts exist before T = 22 s, but only their averaged/predominant location is imaged because their spatial separation did not yet meet the minimum resolvable length of the BP. In such a case, the rupture speed of 0.98 km/s of the apparent unilateral front should be slower than the actual rupture speed on the upward-propagating front. If we assume continuous bilateral propagation from the rupture initiation, the average rupture speed from 0 to 24 s to reach the segment at D about 20 km is about 2.38 km/s (Fig. 5.4(d)). Another possibility to explain the abrupt separations is that the rupture at D about 20 km is triggered on a separated fault. Given the upward propagation (about 2.38 km/s) is slower than the P wave (about 7 km/s) and S wave speeds (about 4.3 km/s) at a depth of 40 km in this region (Eberhart-Phillips & Bannister, 2015), it is possible that either the P or S wave radiated from certain energetic episode of the early rupture triggered the fault segment at D = 20 km.
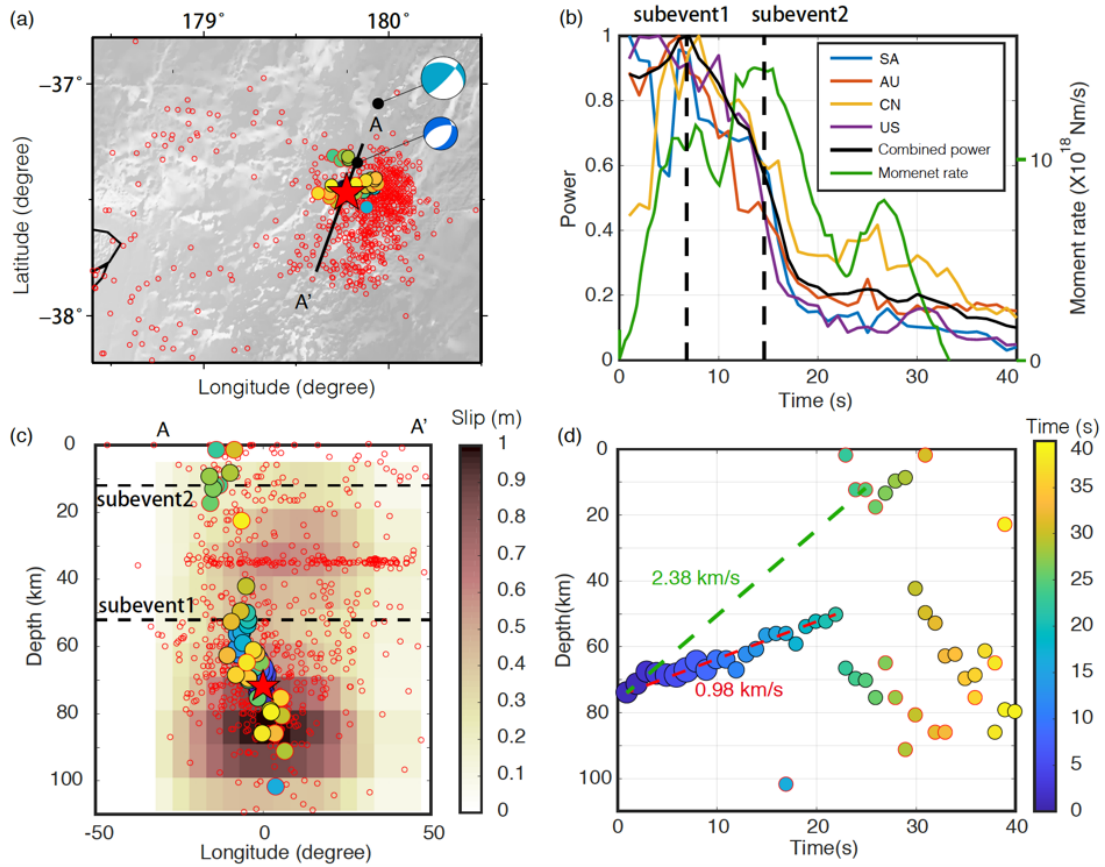
Figure 5.4: Back-projection results of the Mw 7.3 earthquake after combining the images of 4 teleseismic arrays. (a) and (c) are the mapview and vertical cross sections of the back-projection results, respectively. The filled circles are the seismic radiators color-coded by time. The red star and small red circles are the relocated mainshock and aftershocks by Okuwaki et al. (2021). The beach balls are multiple point source inversion results by Okuwaki et al. (2021) color coded by time. The circles with red edges in (a), (c) and (d) are the second strongest peaks of BP images. The second strongest peaks are plotted only when their power exceeds 50% of the strongest peak at a time step. (b) The BP power at each time step. The moment rate of the slip model and the centroid time of the two subevents (dashed lines) are from Okuwaki et al. (2021). The combined power is the sum of the normalized power of each array. (d) The relation between time and the depth of radiators. The red and the green dashed lines are the average rupture speed of the deep and shallow rupture fronts.

5.4 Static and dynamic stress transfer

To understand the triggering effect between the two subevents, we first calculate the static Coulomb stress change on the assumed fault for subevent 2 due to subevent 1 using the software coulomb 3.3 (J. Lin & Stein, 2004). We build simplified slip models based on the subevent inversion results. We use the depths, moments and fault orientations from subevent inversion results. Then we use the moment-dimension scaling relation (Wells & Coppersmith, 1994) to determine the fault length, width and slip assuming that the rigidity of the rock is 30 GPa (Table 5.1). The results (Fig. 5.5 and Fig. 5.6) show that the maximum Coulomb stress change is about 0.4 bar.

We also consider the dynamic stress triggering by examining the synthetic seismograms received at the centroid location of subevent 2 generated from subevent 1. The seismogram is computed with Qseis, a waveform simulator based on an orthonormal propagator algorithm assuming a layered viscoelastic half-space model (R. Wang, 1999). The results (Fig. 5.5(c)) show that the amplitude of the transverse component is the largest, with two pronounced arrivals at 13 s and 20 s, corresponding to S wave (4 km/s) and a reflected phase (2.4 km/s). We then estimate the peak dynamic stress using the following equation (Jaeger, Cook, & Zimmerman, 2009):

$$\sigma = \frac{Gu}{v_s}, \tag{5.1}$$

where u is the peak velocity, which is estimated to be 0.2 m/s according to Fig. 5.5(c). v_s is the phase velocity, which is about 3.34 km/s for S waves at a depth of 10 km according to a 1D velocity model (Kaneko et al., 2019). Given that the density is 2854 km/m^3 (Kaneko et al., 2019), the rigidity G is about 31.8 GPa. The estimated peak stress σ is approximately 19.1 bar, significantly larger than 0.1 bar, which is commonly considered the threshold of dynamic triggering (Brodsky & Prejean, 2005).
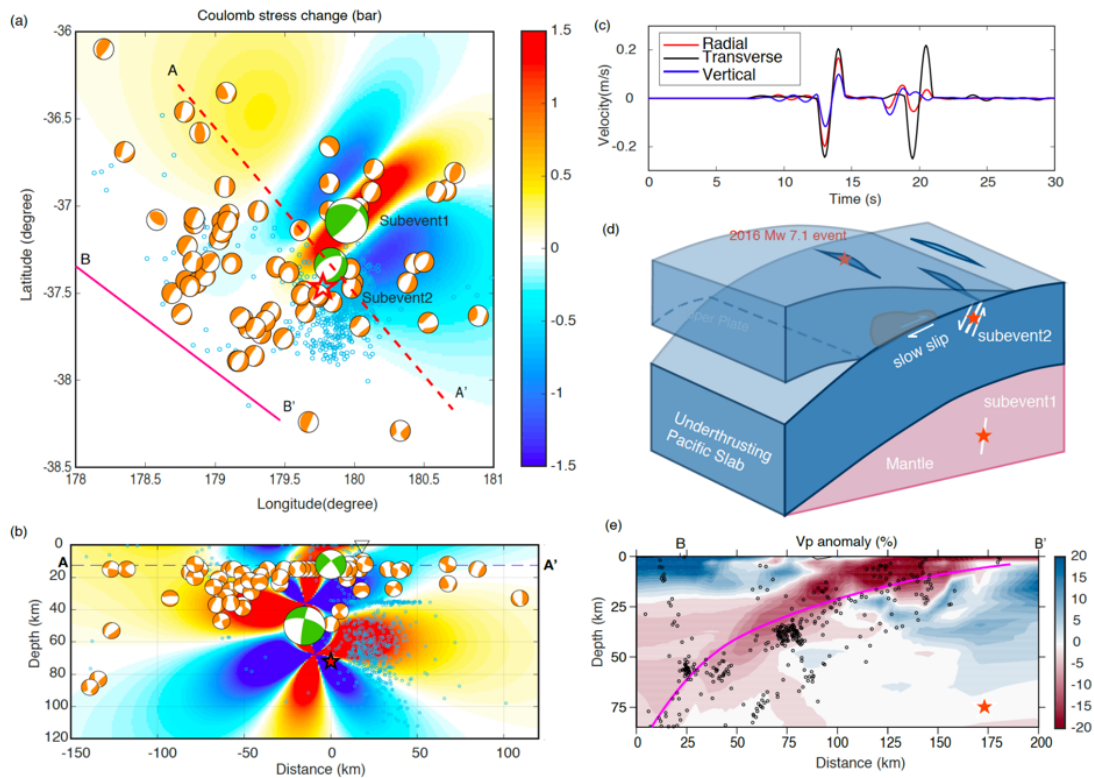
Figure 5.5: Static and dynamic stress triggering and the schematic diagrams for the deep and shallow ruptures. (a) The horizontal cross section (at depth of 12 km) of Coulomb stress change projected to the fault orientation corresponding to subevent 2 (nodal plane 1) caused by subevent 1 (nodal plane 1) based on the subevent inversion results of Okuwaki et al. (2021); The orange beach balls show the focal mechanisms of the background seismicity from 2005 to 2013 (GCMT). The small red circles are the relocated aftershocks by Okuwaki et al. (2021). (b) The vertical cross section of the Coulomb stress changes along AA' (shown in (a)). The results for the other 3 combinations of candidate fault planes are shown in Fig. 5.6; (c) Synthetic velocity seismograms at the centroid location of subevent 2 simulated using the source parameters of subevent 1; (d) The schematic diagrams showing the faults of the two subevents; (e) The vertical cross section of the P wave velocity tomography along BB' (shown in (a)) and the background seismicity (modified from Fig. 5a in Eberhart-Phillips and Bannister (2015)). The red star is the projected hypocenter of the Mw 7.3 earthquake along the direction parallel to the strike of the trench.

Table 5.1: The parameters of the slip models for estimating the Coulomb stress

Subevent and nodal planes	dip	rake	strike	longitude	latitude	depth(km)	moment(N.m)	fault length (km)	fault width (km)	slip (m)
subevent1, np1	80	59	43	179.774	-37.466	52	9.71e19	76.9	31.8	1.983
subevent1, np2	31.0	162.0	298.0	179.774	-37.466	52	9.71e19	76.9	31.8	1.983
subevent2, np1	42.0	-120.0	29	179.8309	-37.12	12	2.12e19	45.96	22.67	1.019
subevent2, np1	54	-65	247	179.8309	-37.12	12	2.12e19	45.96	22.67	1.019
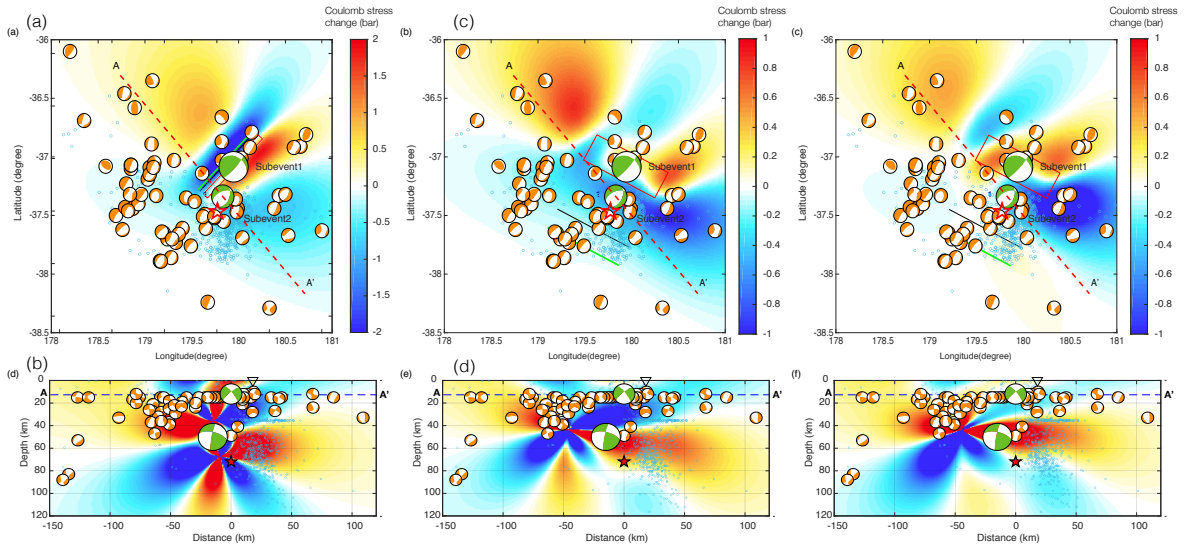
Figure 5.6: The coulomb stress changes using 3 more combinations of candidate fault planes. (a) and (d) are using nodal plane 1 of subevent 1 and nodal plane 1 of subevent 2. (b) and (e) are using nodal plane 2 of subevent 1 and nodal plane 1 of subevent 2. (c) and (f) are using nodal plane 2 of subevent 1 and nodal plane 2 of subevent 2. The symbols are the same as that in Fig. 5.5. The red rectangles are the projection of the fault plane to the ground surface. The black lines are where the faults intersect the depth at which stress is being plotted.

5.5   Discussion

We combine the BPs of 4 teleseismic arrays to resolve the details of the rupture on multiple faults during the Mw 7.3 earthquake, which reveals that the earthquake is mainly composed of two episodes of rupture, with a deep rupture from D at about 70 km to 50 km from 0 to 20 s, and a triggered rupture at D about 20 km from 20 to 40 s. The rupture regions and the bilateral pattern in the vertical direction are consistent with the finite fault slip model and the subevent inversion results of Okuwaki et al. (2021). We then evaluate the possibility that the shallow normal faulting event is triggered by the deep subevent with the effect of static and dynamic stress transfer separately.

5.5.1   Physical mechanisms of the deep rupture

The hypocenter relocated by Okuwaki et al. (2021) is at 72 km, which is below the lower plane of the double seismic zone and is in the slab mantle in this region (Fig. 5.5(e)). There is also a swarm of aftershocks from 50 to 80 km, most of which are in the regions with positive Coulomb stress change (Fig. 5.5(b)). Earthquakes at these depths are rare because the subducting mantle is ductile (Duba, Durham, Heard, Handin, & Wang, 1990). One possible mechanism of the initial deep rupture is that the failure is viscous due to heat produced by rapid strain in fine-grained shear zones, which was proposed by Kelemen and Hirth (2007) and is used to explain the 2012 off-Sumatra earthquake that rupture the whole oceanic lithosphere (McGuire & Beroza, 2012).

Tomography of velocity structure in this region provides another possible explanation: the deep rupture may be caused by brittle failure due to delamination of the lower crust. Delamination is the sinking of part of the continental crust in the mantle due to increased density. The subducting Hikurangi plateau has a thick crust (12 to 15 km) thus possibly behaves like a continental plate and allows delamination. The tomography cross section along A-A' (Fig. 5.5(d)), modified from Fig. 5a in Eberhart-Phillips and Bannister (2015),

shows a high v_p anomaly (3%-10%) region above the hypocenter. This v_p anomaly region is in the lower crust and uppermost mantle (150 to 200 km in horizontal direction, and 25 to 70 km in depth in Fig. 5.5(e)), which correlates with the location of the first sub-event. This low v_p anomaly indicates a delaminating lower crust, which enables the brittle failure and can explain the deep faulting in the slab mantle (Fillerup, Knapp, Knapp, & Raileanu, 2010).

Another possibility for faulting in the slab mantle is related to fluid-aided embrittlement or weakening (Halpaap et al., 2019). The increasing pore pressure reduces effective normal stress and allows for earthquake rupture in high pressure and temperature conditions. Fluids may penetrate through the normal faulting, which is enhanced by the downward pumping effect by slab bending (Ranero, Phipps Morgan, McIntosh, & Reichert, 2003; Faccenda, Gerya, & Burlini, 2009). In Mariana, significant velocity reduction below the southernmost Mariana trench is observed, which provides evidence for such penetration (Wan et al., 2019). The velocity reduction is resolved with an array of ocean bottom seismometers above the Mariana trench and an active source seismic experiment. In the future, a similar experiment in the East Cape region can be performed to investigate this hypothesis. The fluid may also be fed from the lower region (Halpaap et al., 2019). Halpaap et al. (2019) observe seismicity at the depth of 60 to 80 km (about 40 km below the bottom of the slab) in the subduction zone in Sanriku, Japan and Northeastern New Zealand, which is proposed to be related to fluid flow.

The second subevent is in the vicinity of historical normal faulting events (Fig. 5.5(a) and (b)), which are related to the normal faults activated or caused by slab bending (Masson, 1991; Ranero et al., 2003). The near parallel directions of the tectonic fabric and the axis of the bending (Fig. 5.1) further enhances the frequent normal faulting earthquakes (Ranero et al., 2003).

5.5.2   The role of the triggering effects in the earthquake sequence

The rupture of the shallow faulting is probably triggered by the rupture of the deep faulting. The Coulomb stress change on the assumed fault due to the rupture of the first fault is about 0.4 bar. The peak dynamic stress is about 19.1 bar when assuming an elastic model. With the existence of the overlying sedimentary layers which amplifies the dynamic stress (Wallace et al., 2017), the amplitude of dynamic stress could be two orders of magnitude larger than the static stress change. The dynamic stress calculation is based on a point source. If considering the upward propagation of the initial rupture, the rupture directivity will result in elevated dynamic stress in the shallow region. The back-projection results show that the rupture of the shallow event starts around 20 s, which is coincidentally consistent with the timing of the reflected wave at about 20 s shown in Fig. 5.5(c). It is also possible that the S wave radiated by the first subevent at a later time (e.g. about 7 s) triggers the shallow rupture.

The rupture of the subsequent Mw 7.4 and Mw 8.1 earthquakes occurred about 4 and about 6 hours later after the Mw 7.3 event, which are probably due to a delayed dynamic triggering of the Mw 7.3 earthquake considering the fast decay of the static stress with distance. Possible triggering mechanisms with delay include frictional properties changes (Parsons, 2005), pore fluid redistribution (Brodsky & Prejean, 2005), triggering by slow slip or earthquakes that are instantaneously triggered (Brodsky, 2006; Shelly, Peng, Hill, & Aiken, 2011). Due to a lack of observation, we can not find more evidence for these mechanisms.

The Mw 7.4 and Mw 8.1 earthquakes are 900 km to the north of the Mw 7.3 earthquake. The two earthquakes are close to the Kermadec Island, a region with dense historical M 7+ megathrust earthquakes. In contrast, the Mw 7.3 earthquake fails to trigger a few aftershocks along the subduction zone between the Mw 7.3 and another two earthquakes, a 900-km-long section along the subduction zone. The low seismicity rate and the lack of

90

large megathrust earthquakes from 38 °S to 34 °S indicates that this region may be a weakly coupled zone which accommodates shear deformation through ductile or aseismic slip. Its coupling condition may be similar to that of the eastern North Island based on GPS studies (Wallace & Beavan, 2010; K. Wang & Bilek, 2011). However, we take a cautionary note that the about 100 yrs recording history of larger earthquakes is not long enough to exclude the possibility that this region is well locked in an interseismic period.

CHAPTER 6

Fault simulation on an orthogonal strike-slip fault system: rupture pattern and the maximum earthquake size

Abstract

Motivated by the complexity of the 2012 Mw 8.6 off-Sumatra earthquake and the 2019 Ridgecrest earthquake sequence, we conduct earthquake cycle and dynamic simulations on an orthogonal strike-slip fault system. The 2012 Mw 8.6 off-Sumatra earthquake is the largest strike-slip and intraplate earthquake recorded to date with an exceptionally tortuous rupture path. It featured two episodes of branching into fault segments that were experiencing increased compressive dynamic stresses, hence increased frictional strength. Meng et al. [2012] attributed this unexpected compressional branching to slow rupture and weak pressure-sensitivity of the fault strength. Here, by conducting 3D earthquake cycle and dynamic rupture simulations on a T-shape conjugate strike-slip fault system, we check the effect of different frictional coefficients and heterogeneous pre-stress on the rupture pattern. Our simulation results show that when small events alternatively rupture the compressional and dilatational branches, lower pre-stress on the dilatational stress and high pre-stress on the compressional branch is occasionally produced. This pre-stress favors the rupture to branch into the compressional branch in following large event. Besides, we find that for the rupture to propagate to the compressional segment, a low frictional coefficient of 0.2 is needed. We suggest that serpentinized minerals or ductile shearing may provide the low

apparent frictional coefficient. We also reproduce rupture patterns close to the Ridgecrest earthquake sequence, with the second earthquake nucleating in the positive Coulomb stress region with a delay. In our simulation, the delayed triggering is related to aseismic slip in the transition zone. Poroelastic effect is another alternative mechanism for the compressional branching. It buffers the dynamic clamping instantaneously so that the branching is not sensitive to the change of normal stress. After the diffusion of fluid pressure, the stress and strength of the fault will go back to the normal level, which can explain the delayed rupture of the dilatational branch for both episodes in the 2012 Off-Sumatra earthquake and the Mw 7.1 Ridgecrest earthquake.

This is an independent work by myself. The manuscript is in preparation. We will collaborate with Huihui Weng, Yindi Luo and Jean-Paul Ampuero in the paper.

6.1   Introduction

The possibility of an earthquake rupture propagating along distinct branches of a fault system has been the subject of several earthquake dynamic studies. Understanding the mechanics of fault branching, rupture path selection and the connectivity of rupture across multiple fault segments could provide a physical basis to assess the maximum earthquake size in complex fault systems. The basic principles of rupture branching are established based on analytical studies. It is shown that fault branching can occur under specific conditions of principal stress orientation, branching angles and rupture speed (Poliakov, Dmowska, & Rice, 2002; Kame, Rice, & Dmowska, 2003). On the other hand, rupture branching can be complicated by the interaction with directivity effects (Fliss, Bhat, Dmowska, & Rice, 2005), rupture propagation and arrest (Bhat, Olives, Dmowska, & Rice, 2007), fault geometry, heterogeneous stress distribution and the state in the earthquake cycle (Duan & Oglesby, 2007; Duan, Liu, & Elliott, 2019; D. Liu, Duan, Prush, Oskin, & Liu-Zeng, 2021). The 2012 M 8.6 off-Sumatra earthquake provides a rare example of large scale branching

in a system of almost orthogonal faults (Meng, Ampuero, Stock, et al., 2012). Its rupture path showed preferred branching into the compressional side, i.e. into faults that were experiencing increased normal stresses (Fig. 6.1). This challenges the conventional view that clamping increases frictional strength and hence discourages compressional branching (Oglesby, 2005). Meng, Ampuero, Stock, et al. (2012) attributed this puzzling observation to weak pressure sensitivity of fault strength (low apparent friction coefficient) in the deep oceanic lithosphere.

The 2019 Ridgecrest earthquake sequence is another earthquake that occured on similar orthogonal strike-slip fault system (Fig. 4.5 and Fig. 4.6). The first Mw 6.4 event ruptured an L-shape fault system and triggered the Mw 7.1 earthquake with a delay about 1 day in a positive Coulomb stress region of the Mw 6.4 earthquake. The Ridgecrest earthquake sequence draws attention of a lot of researchers with the dense obervations in southern California. The mechanism of the delayed triggering of the Mw 7.1 earthquake is also under debate.

Facilitated by the opportunities and advances in observation studies of large earthquakes, including the studies based on space-geodesy (Ozawa et al., 2011; Simons et al., 2011), waveform inversions (Ide et al., 2011; Wei et al., 2013) and short-period back-projections (Ishii, 2011; Koper et al., 2011), numerous efforts to understand the underlying earthquake physics through earthquake cycle and dynamic simulations have assessing the role of a variety of ingredients, including depth-dependent heterogeneities (Y. Huang et al., 2012; A. Kato & Igarashi, 2012), plastic dissipation and poroelasticity (Ma, 2012; Zhu et al., 2020), subducting seamounts (Duan, 2012; Yu et al., 2018) and shallow velocity-strengthening (Kozdon et al., 2012). The unusual complexity of the 2012 off-Sumatra event, the largest strike-slip and intraplate earthquake recorded to date, provides an opportunity to shed light on the dynamics of such extreme events.

Here, we perform earthquake cycle simulation and one-way coupling dynamic simulations on an orthogonal conjugate strike-slip fault system to (1) address the conditions of frictional

coefficient and pre-stress that allow dynamic branching on an orthogonal segment in a compressional quadrant. (2) explain the delayed triggering of the Mw 7.1 Ridgecrest earthquake. (3) research the rupture pattern on the orthogonal conjugate strike-slip fault system.

6.2   Method

We use a quasi-dynamic solver for earthquake cycle simulation, which generates earthquake histories of thousands of years efficiently. All earthquakes have spontaneous nucleation, which provides initial conditions for dynamic simulation. The dynamic simulation considers the stress change traveling with the rupture front and seismic radiation, which is more accurate and essential for investigating the rupture propagation near the fault intersection.

6.2.1   The earthquake cycle simulation

We conduct numerical simulation of earthquake cycles using a quasi-dynamic code, QDYN (Luo & Ampuero, 2011, 2012), which applies a boundary element method with adaptive time stepping. The stress is accumulated during interseismic periods and released during coseismic period, which is described by the equation:

$$\tau_i = \sum K_{ij} u_j - \frac{G}{2\beta} V_i, \tag{6.1}$$

where τ_i is the stress at j th cell, u_j is the slip at j th cell, K_{ij} is the "stiffness matrix". The last term is a approximation of the seismic radiation damping, where G is the shear modulus, β is the shear wave velocity and V_i is the slip rate of the i th cell.

The frictional stress is assumed to obey the rate-and-state friction law of Dieterich (1979) and Ruina (1983):

$$\tau = \mu \sigma_n, \tag{6.2}$$

$$\mu(V, \theta) = \mu^* + a \ ln \left(\frac{V}{V^*} \right) + b \ ln \left(\frac{\theta V^*}{D_c} \right), \tag{6.3}$$

95

$$\frac{d\theta}{dt} = 1 - \frac{\theta V}{D_c}, \tag{6.4}$$

where σ_n is the effective normal stress, V is slip rate, θ is the state variable. μ^*, V^*, a, b, D_c are friction parameters.

We take the first episode of compressional branching in the 2012 off-Sumatra earthquake (from segment (1) to (2) in Fig. 6.1) as an example in the modeling and build a 3D fault system consisting of 4 fault segments (Fig. 6.2). In our model, fault plane A is a pure right-lateral strike-slip fault. Fault plane B is a pure left-lateral strike-slip fault. The length and width are estimated based on back-projection results (Meng, Ampuero, Stock, et al., 2012) and finite fault slip models (Yue, Lay, & Koper, 2012). The two fault planes are divided into 6825 grids, with a grid sizes of 2 km. The 4 fault segments separate from each other by 10 km, which avoids the numerical singularity and mimics the rupture barrier caused by the complicated microstructure at the fault intersection at the same time. The two fault planes of the conjugate strike-slip fault system are discontinuous in several cases, including the fault system of the Garlock fault and the East California Shear Zone, the Anyimaqen-Kunlun-Muztagh suture zone and the two NW-SE strike-slip faults to the north (with a gap of about 100 km). There are two sources of the discontinuities: (1) If the fault system is not mature, each fault consists of discrete subparallel segments of different sizes separated by geometrical discontinuities (Perrin et al., 2016). The 2019 Ridgecrest earthquake sequence occurred on such an immature conjugate strike-slip fault, which shows multiple sub-parallel faults highlighted by relocated aftershocks (Ross et al., 2019). (2) If the fault is mature, large dislocation on one fault may lead to large offsetting (no any real-world example) or rotation of another fault. The intersection of the Red River Fault and Xianshuihe-Xiaojiang Fault system shows a rotation case, where the slip of the Xiaojiang Fault (similar to Fault segment 2 and 3 in this research) causes a clear bending on the Xianshuihe fault (similar to Fault segment 1 in this research) (Taylor & Yin, 2009). These microstructures act as barriers for the rupture to propagate through and are simplified to a gap in our model.

The gaps partly solve the numerical problem by decreasing the stress concentration. But the stress concentration at the intersection is still very strong. After several earthquake cycles, the normal stress at the closest grid to the intersection in the dilatational quadrant decreases to 0 MPa after several earthquake cycles, which causes numerical singularity. In real world, large strike-slip dislocation on a fault could be the shearing of multiple parallel faults or rotation of small blocks (Sylvester, 1988). We simplified these process with a viscoelastic relaxation process.

The rupture patterns could be sensitive to the geometry at the intersection and the loading on segment 4. So we calculated and discussed the simulation results of 7 more geometry models. For each case, one or two fault planes are continuous.

The back-projection results of the off-Sumatra earthquake show that fault plane A and B are approximately orthogonal. Potentially, aftershock distribution and high resolution bathymetry data could provide more accurate constraints. But the aftershocks are hard to relocate due to a lack of local seismic stations. The high-resolution bathymetry and seismic reflection data (Singh et al., 2017; Hananto et al., 2018) reveal complex fault system composed of several groups of shear zones, without any one has consistent strike direction as Fault Plane B resolved by back-projeciton. This is probably due to the thick sedimentary layers or Fault plane B is en echelon strik-slip faults with overstepping. For simplicity, we assume that the angle between the two fault planes is 90 degrees based on the back-projection results (Meng, Ampuero, Stock, et al., 2012) and assume dip angle of 90 degrees for the two fault planes based on the focal mechanism of the earthquake.

We load the fault system by adding creeping patches (the orange patches in Fig. 6.2) around the locked patches of the fault system (the blue patches in Fig. 6.2) following Stuart and Tullis (1995). We determine the size of the loading patch and benchmark our loading method using the SCEC SEAS models. The creeping patches are moving at a constant rate of 10^{-8} m/s. The same slip rates on the two fault planes make the faults optimally oriented with respect to the regional stress 45° to the principal stress axis, based on Delescluse and
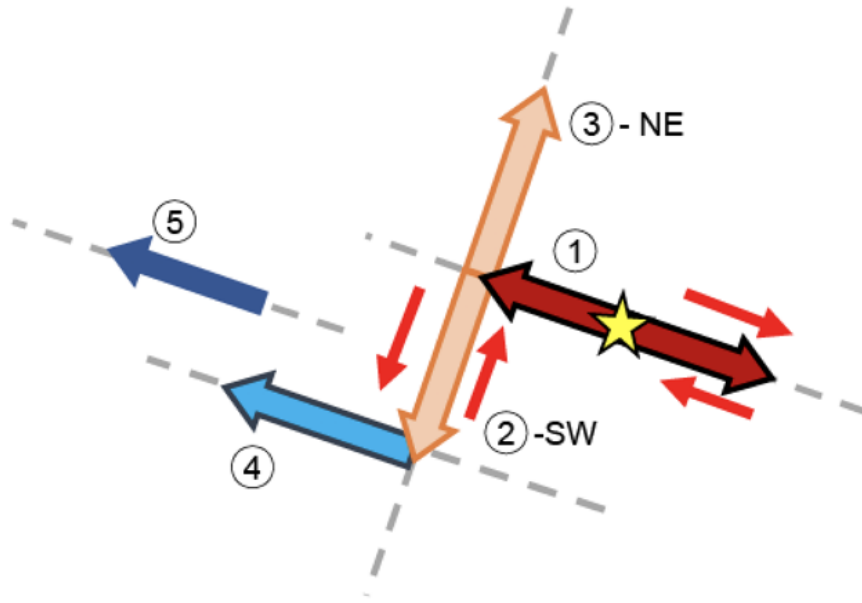
Figure 6.1: Concept map of the kinematic rupture process of the 2012 off-Sumatra earthquake. The star is the epicenter. The arrows show the rupture directions on each segment.
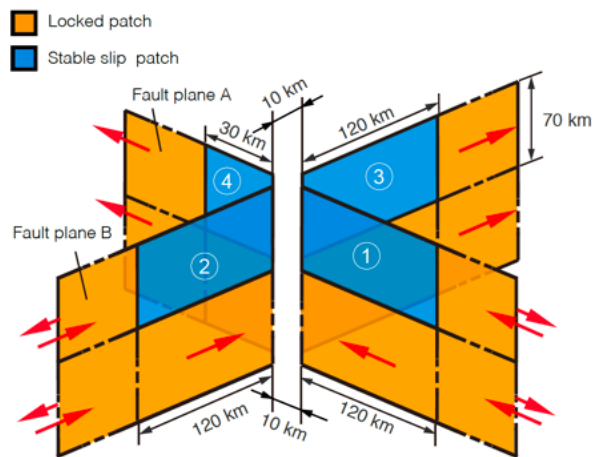

Figure 6.2: The basic geometry (geometry 1) model for the earthquake cycle simulation.

Chamot-Rooke (2007). This is also required for the rupture of multiple faults on a conjugate strike-slip fault system (Lozos, 2022).

Fig. 6.3 shows the values of a - b. The locked patches have an a-b smaller than 0, which allows the seismic slip to nucleate. The loading patches have a-b larger than 0. The boundaries between the locked and loading patches is tapered in a transition zone with a width of 15 km.

The range of the frictional coefficient (μ^* in equation 6.3) is 0.37 to 0.66 based on experiments (Hunfeld, Niemeijer, & Spiers, 2017). Meng, Ampuero, Stock, et al. (2012) inferred that the strength of the fault is not sensitive to the pressure, which means a low frictional coefficient. To study the threshold of the low frictional coefficient that allows the compressional branching, we run earthquake cycle simulations with $\mu^* = 0.2$, 0.3 and 0.4 in Test 1, 2 and 3, respectively.

We assume uniform distribution of the initial effective normal stress and characteristic nucleation length (D_c). We assume an σ_n of 50 MPa, which is difficult to constrain. The effective normal stress is not constant in the earthquake cycle simulation. The coseismic slip, tectonic loading and the viscoelastic relaxation will change the normal stress over time. The nucleation length L_c, or the minimum size of the rupture region for instability can be estimated using the equation:

$$L_c = \frac{ED_c}{2(1 - \nu^2)\sigma_n(b - a)},\tag{6.5}$$

where E is Yong's modulus (65 GPa), ν is the Poisson's ratio, which is assumed to be 0.25 in our simulation. We use a D_c of 0.08 m, so the nucleation length L_c is about 9000 m, which is 4 times of the grid length. Using this combination of σ_n and D_c, we simulate a spectrum of earthquakes from Mw 6.6 to Mw 8.1, which produces heterogeneous stress distribution on the fault. The moment release in a super cycle is about 2.69e21 N.m (Mw 8.28), which is close to that of a Mw 8.0 earthquake. A smaller D_c leads to a smaller L_c, which increases
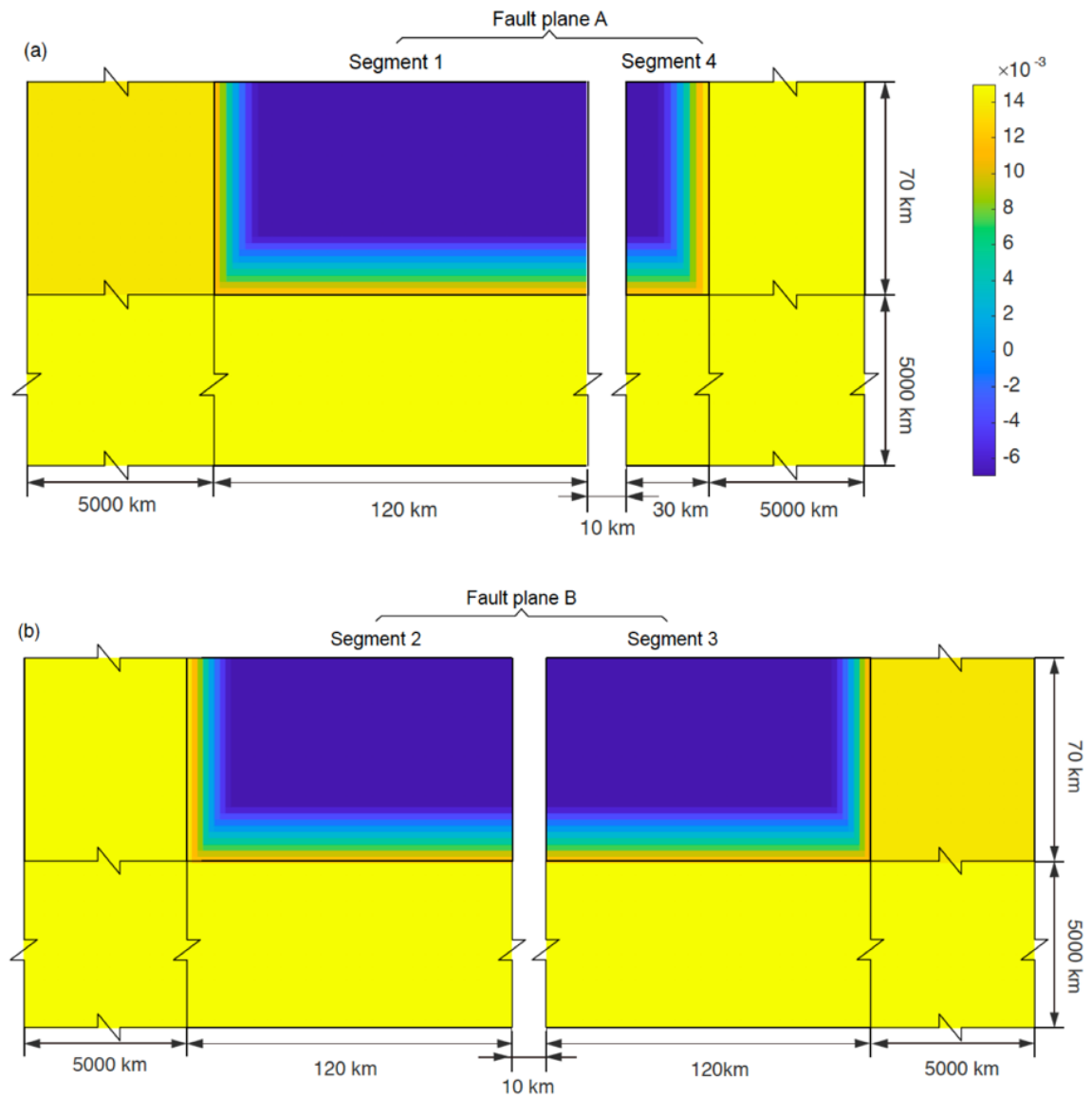
99

Figure 6.3: The distribution of a − b. b is a constant, 0.01.

the computation a lot due to an increasing number of smaller earthquakes.

6.2.2　The method of the dynamic simulation

To simulate the rupture process more accurately, we run dynamic simulations for selected events, which considers the stress perturbation caused by seismic waves. We use the software SPECFEM3D (Komatitsch & Tromp, 2002; Galvez, Ampuero, Dalguer, Somala, & Nissen-Meyer, 2014) to run dynamic simulation. The dynamic simulation starts when an earthquake we interest nucleates (when the maximum slip rate exceeds 0.01 m/s. Occasionally a threshold of 0.2 m/s is used for the rupture to transit to dynamic slip within about 100 s). In the dynamic simulations, we use the same fault geometry, constitutive law (rate and state dependent equations) and parameters (including D_c, μ^*, a, b) as the earthquakes cycle simulations. The initial values of the variables (θ, V) and the stress distribution are generated by the earthquake cycle simulation. The density, P and S wave velocities of the surrounding media are 3000 km/m, 8000 m/s and 4618 m/s, respectively. The meshes are generated using CUBIT (Fig. 6.4), which are composed of 4,050,000 hexahedrons. The gird size is about 2 km, the same as the earthquake cycle simulation.

6.3　Result

6.3.1　Result of cycle simulation

The simulated slip histories (Fig. 6.5) are all the same for Test 1, 2 and 3. But the shear stress are different (Fig. 6.6). Fig. 6.5 shows that the fault Seg 1, 2 and 3 rupture independently. Foreshocks, aftershocks and swarms of small earthquakes occur at the boundary of the fault segments. The irregular earthquake sequences produce heterogeneous stress fields. The earthquake sequences starting in about 5031 and about 6382 years (shown by blue dashed lines in Fig. 6.5(b)) nucleate from Seg 1 and start with a stress distribu-
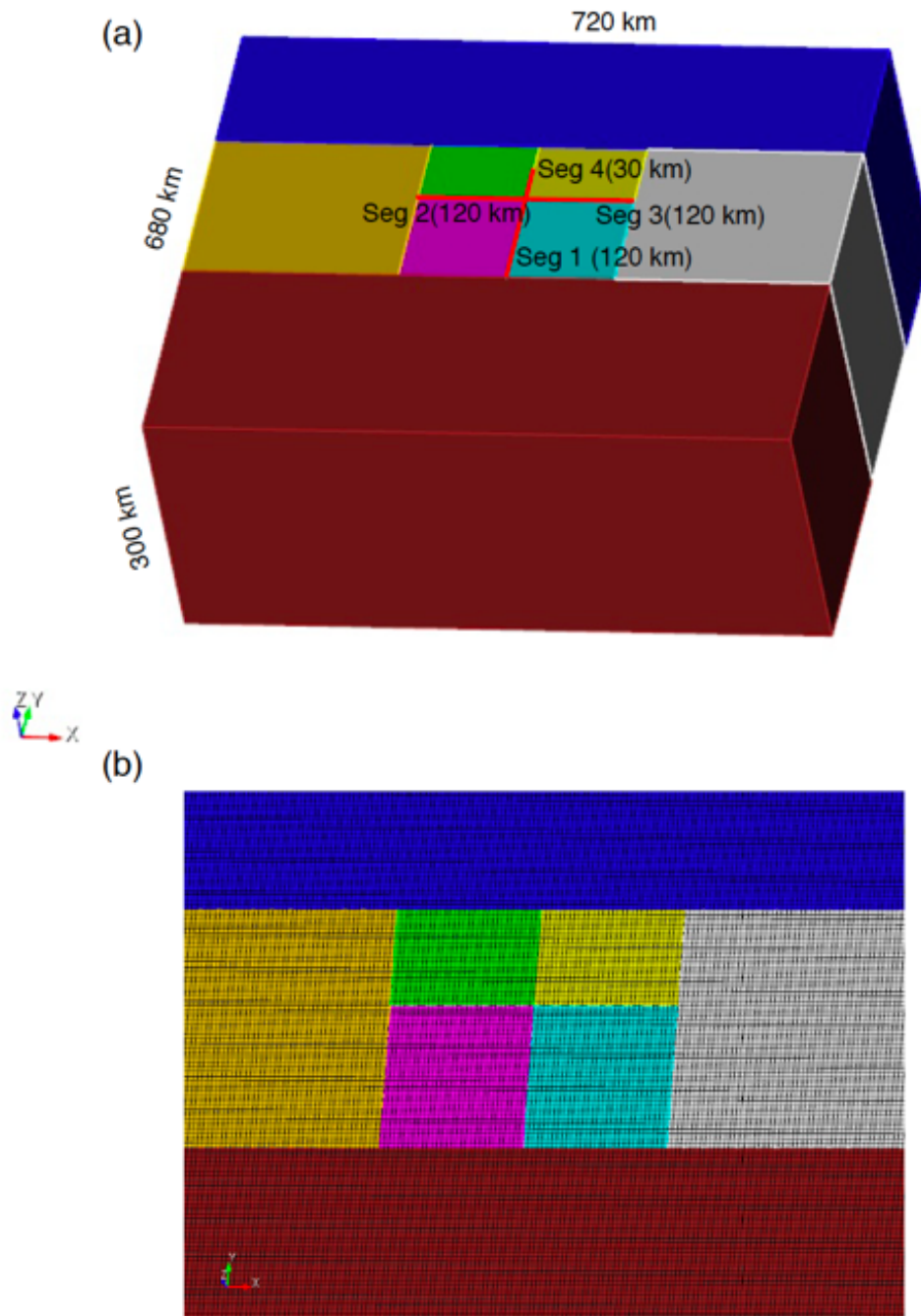
Figure 6.4: The fault geometry for the earthquake dynamic simulation. (a) The fault geometry and the surrounding media. (b) The meshes in the fault domain.

tion that favors the compressional branching, which is consistent with the 2012 off-Sumatra earthquake. Fig. 6.6 shows that the dilatational branch (Seg 3) has a relatively lower initial stress due to previous events, which may favor the rupture to branch into the compressional branch compared to the dilatational branch. But cycle simulation result shows that the compressional branch does not rupture immediately after the rupture reaches the intersection, possibly due to that the static stress transfer is not strong enough for the rupture to pass through the intersection. The compressional branch (Seg 2) ruptures several hundreds of years later, with enough accumulated stress due to tectonic loading. So we run a one-way coupled earthquake dynamic simulation by using the same initial condition of the two earthquake sequences as the earthquake cycle simulation to check whether the rupture can pass through the intersection after considering the effect the dynamic stress.

6.3.2 Result of earthquake dynamic simlation

We run the dynamic simulation for the earthquake sequences in 5031 yr and 6382 yr when $\mu^* = 0.2$, 0.3 and 0.4, respectively. The rupture pattern for the case when $\mu^* = 0.2$, 0.3 and 0.4 in 5031 yr and 6382 yr are shown in Fig. 6.7 . Fig. 6.8 to Fig. 6.11 show more details for the case in 5031 yr for $\mu^* = 0.2$ and the case in 6382 yr for $\mu^* = 0.3$, respectively.

The rupture propagates to the fault intersection and triggered slip on Fault Plane B for all of the 6 cases (Fig. 6.7). But the rupture propagation on Fault Plane B are very different. When $\mu^* = 0.4$, the rupture on the dilatational branch is first triggered and the rupture on the compressional branch starts several second later. But the rupture on both the compressional and dilatational branches stop after 10 s. When $\mu^* = 0.3$, The dynamic simulation results for the sequence in about 5031 yr is similar to the cases when $\mu^* = 0.4$. But for the sequence in 6328 yr, after the first triggered rupture stops, another nucleation starts at the intersection about 20 s later. Fig. 6.10(b) shows that the re-nucleation point start at the bottom of the fault at the intersection, which is probably triggered by a reflected rupture front form the surface at the fault intersection. The triggered rupture propagates
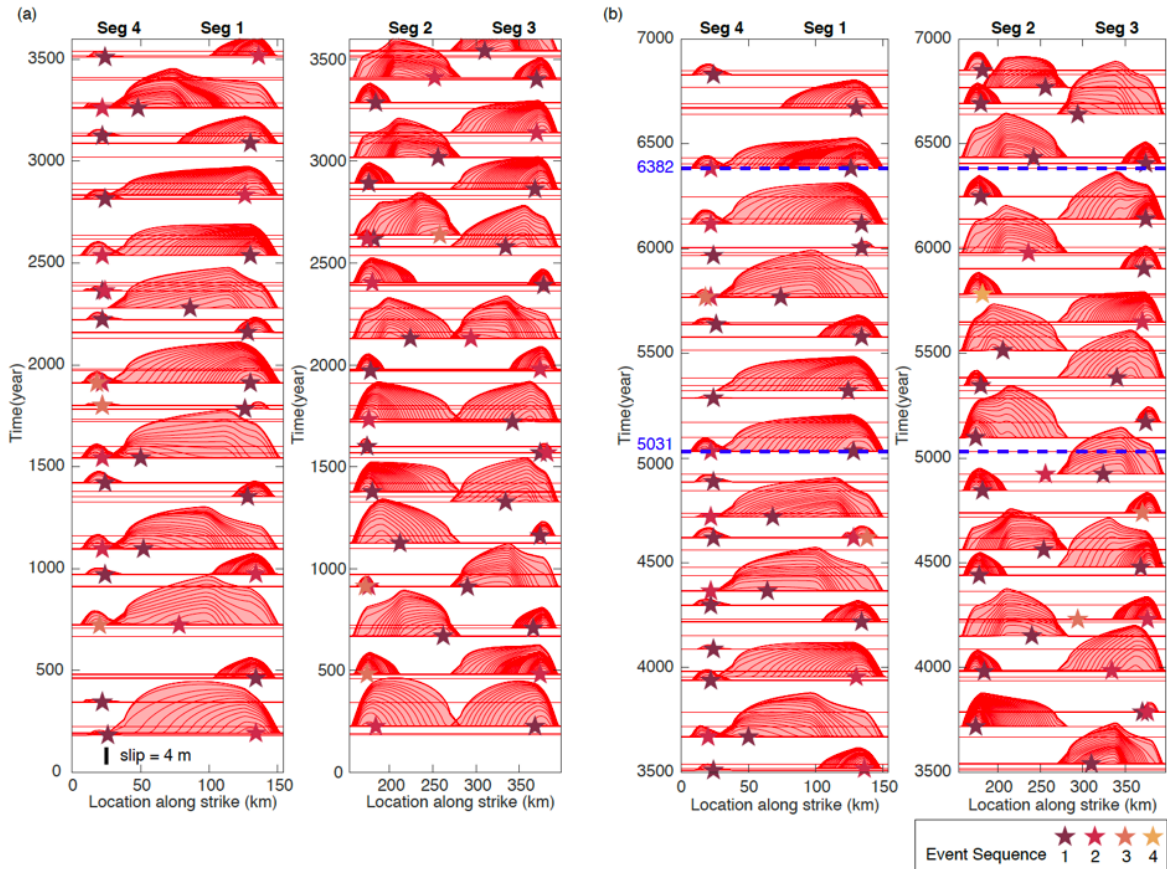
Figure 6.5: The spatial and temporal distribution of the slip on the T-shape conjugate fault system from 0 to 3500 yr (a) and from 3500 to 7000 yr for Test 1 (The slip histories of Test 2 and Test 3 are all the same as Test 1). The blue dashed lines highlight the start of the two earthquake sequences which are then recalculated with dynamic simulations.
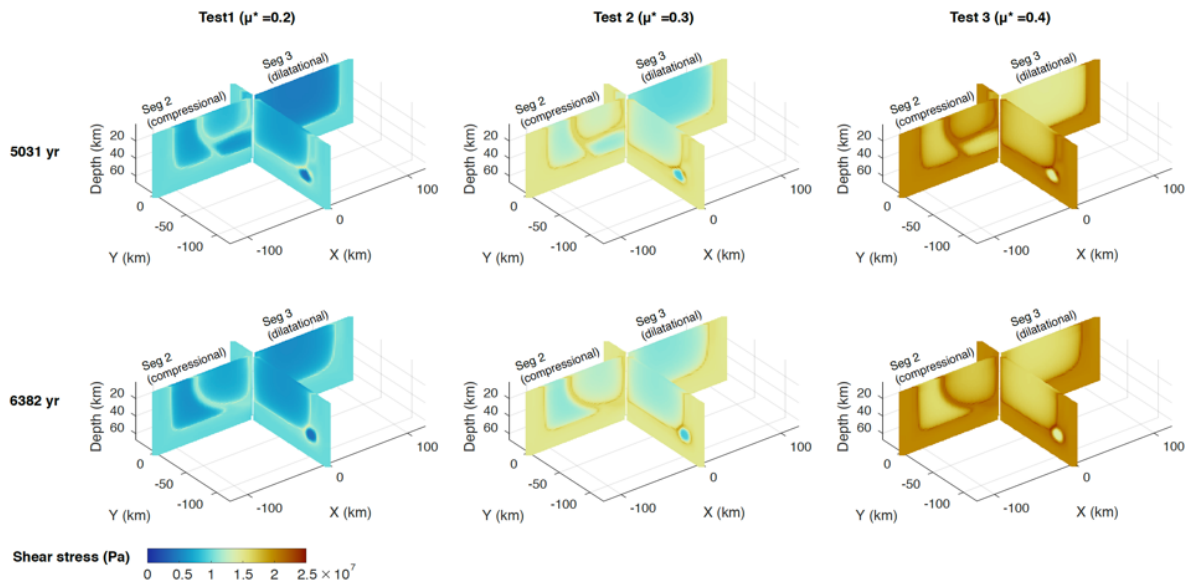
Figure 6.6: The initial shear stress distributions for dynamic simulation, which are the stress distribution before the nucleation of the first earthquake in the sequences in 5031 yr and 6382 yr. Different columns are for different tests with different μ^*. Different rows are for different sequences.
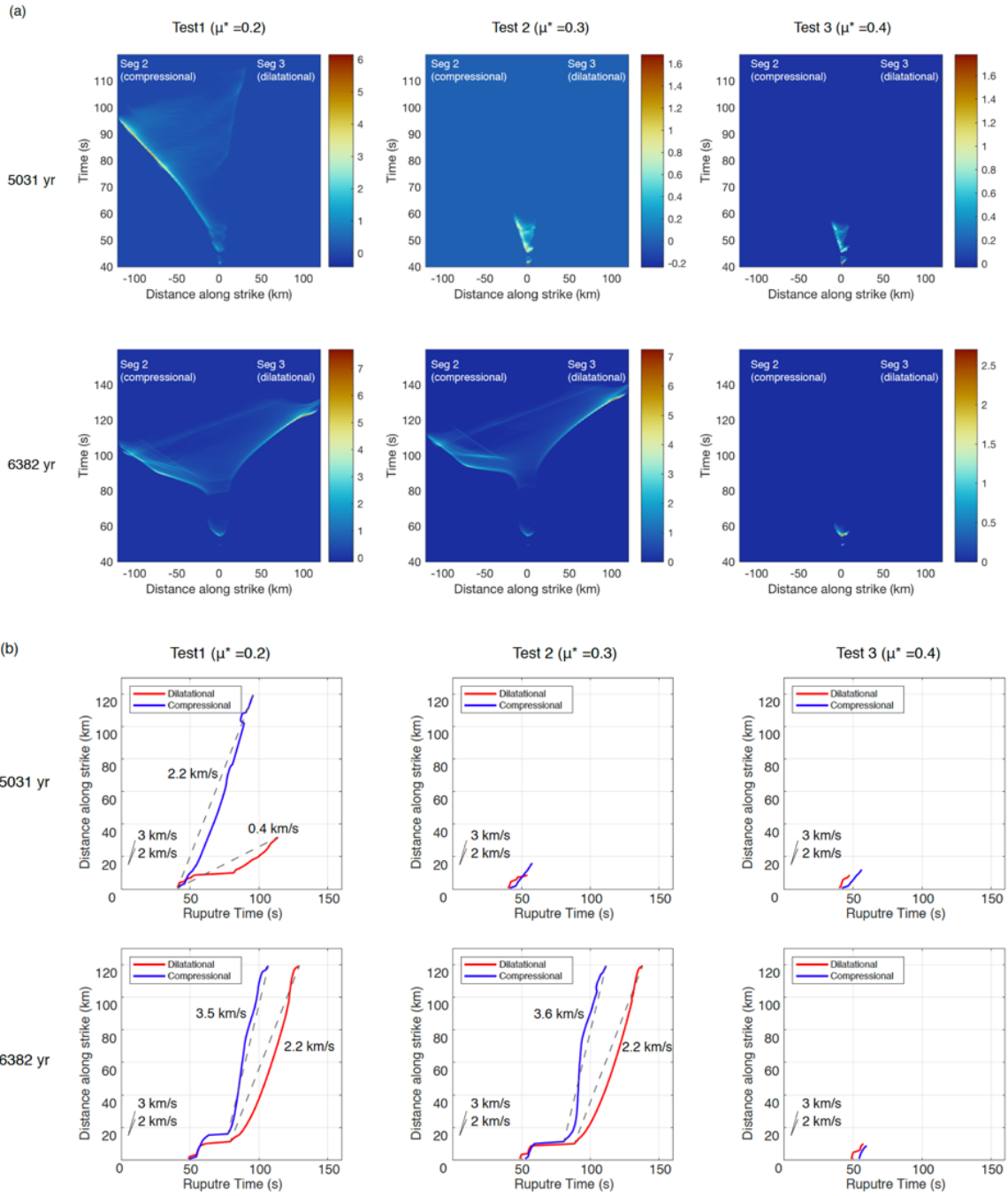
Figure 6.7: Earthquake dynamic simulation results of two sequences. (a) The spatio-temporal distributions of slip rate at the depth of 10 km on Seg 2 and 3 on Fault plane B. (b) Rupture propagation along strike direction on Seg 2 (compresional) and 3 (dilatational).

to the compressional branch first, with an average rupture velocity of about 3.6 km/s. The rupture on the dilatational branch start about 8 s later than the dilatational branch and propagates with a smaller average speed (about 2.2 km/s). The rupture pattern is similar to the first compressional branching observed in the 2012 off-Sumatra earthquake. When μ^* = 0.2, the sequence in about 6328 is similar to the case when $\mu^* = 0.3$. The average rupture speeds on the compressional and dilatational branches are about 2.5 km/s and 2.2 km/s. The sequence in 5031 yr shows that the rupture on the two branches propagate immediately after the rupture is triggered. But compressional branch propagates with an average rupture speed of 2.2 km/s. The rupture on the dilatational branch propagate for only 30 km, with an average rupture speed of about 0.4 km/s.

The results show that a lower frictional coefficient makes it easier for the rupture to branch into fault plane B, not only the compressional branch. The difference between the sequences in 5031 yr and 6382 yr when using the same μ^* is due to the shear stress level on the dilatational branch. For example, when μ^*=0.2, the sequence in 5031 yr starts about 108 yr after the dilatational branch ruptured last time. So the accumulated shear stress on the dilatational branch (about 4.3 MPa, Fig. 6.8) is smaller than that of the sequence in 6382 yr, which start about 187 yr after the last event and the accumulated shear stress is about 5.4 MPa. But the initial shear stress on the compressional branch in 5031 yr (8.1 MPa) is larger than that in 6382 yr (7.0 MPa). So the compressional branch start to rupture earlier. The rupture speed in 6382 yr is faster than that in 5031 yr. In the 5031 yr event, the rupture propagates along the strike at a shallow depth ($<$40 km) from 45 s to 70 s. In the event in 6382 yr, the rupture propagates along the lower boundary of the seismogenic zone (at a depth of about 50 km) from 70 to 85 s, where high shear stress is accumulated during interseismic period (Fig. 6.11).
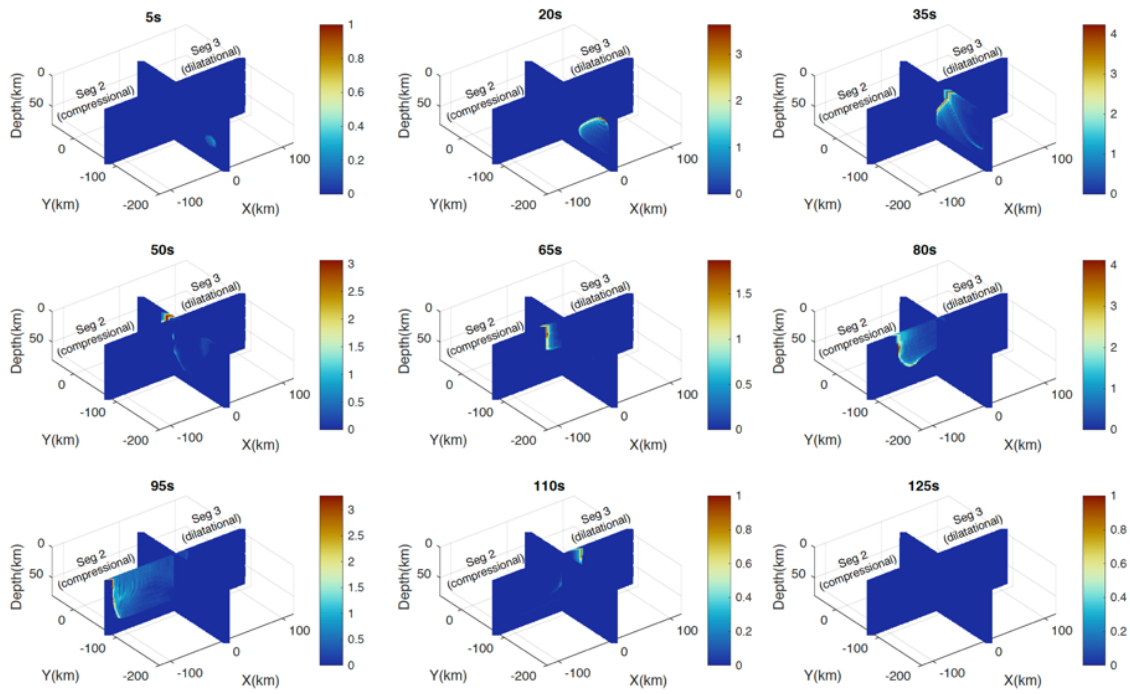
Figure 6.8: The slip rate at different time steps for the sequence in 5031 yr for Test $1(\mu^*{=}0.2)$.
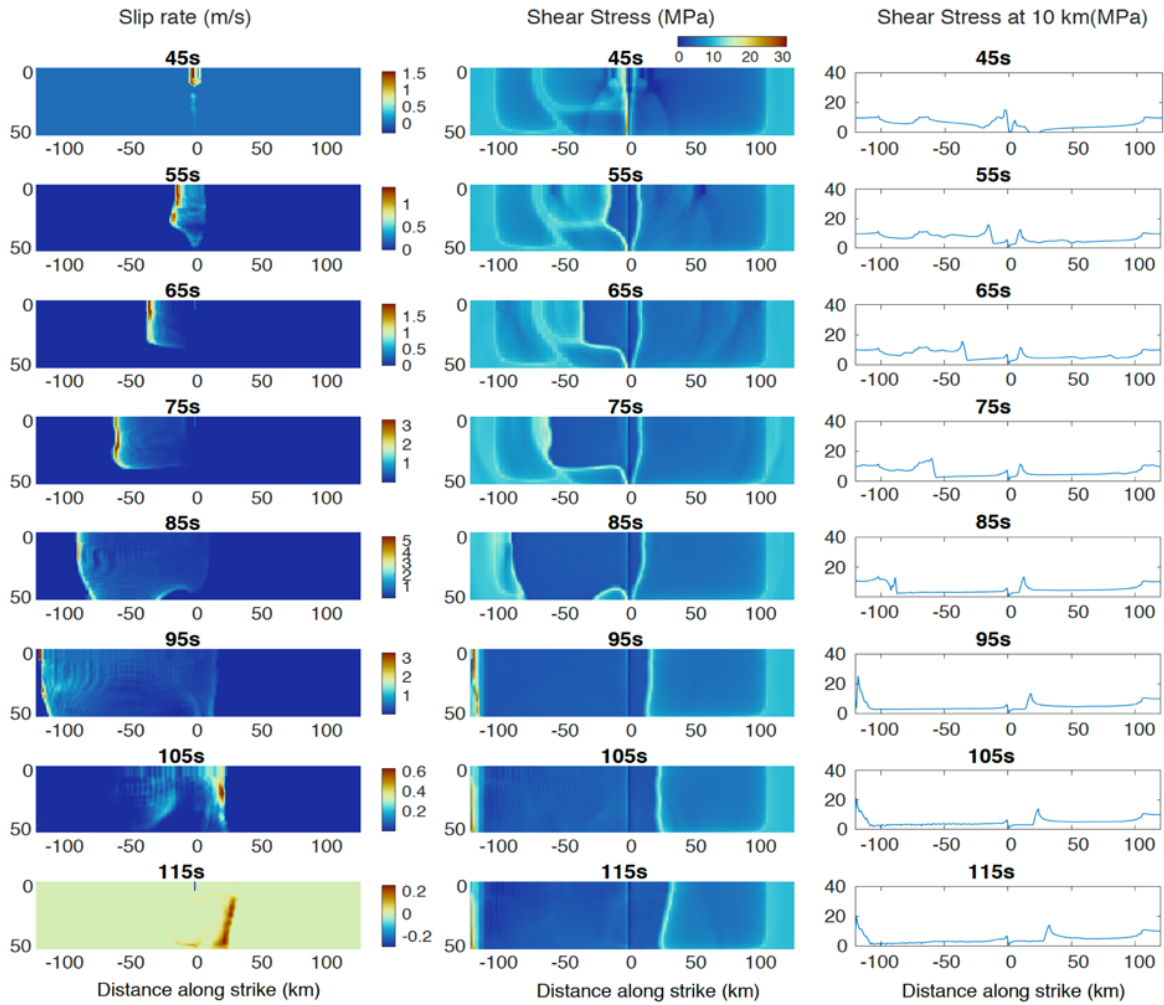
Figure 6.9: The slip rate, shear stress distribution on Fault Plane B and the shear stress profile along the reference line at the depth of 10 km on Fault Plane B at different time steps for the sequence in 5031 yr for Test 1.
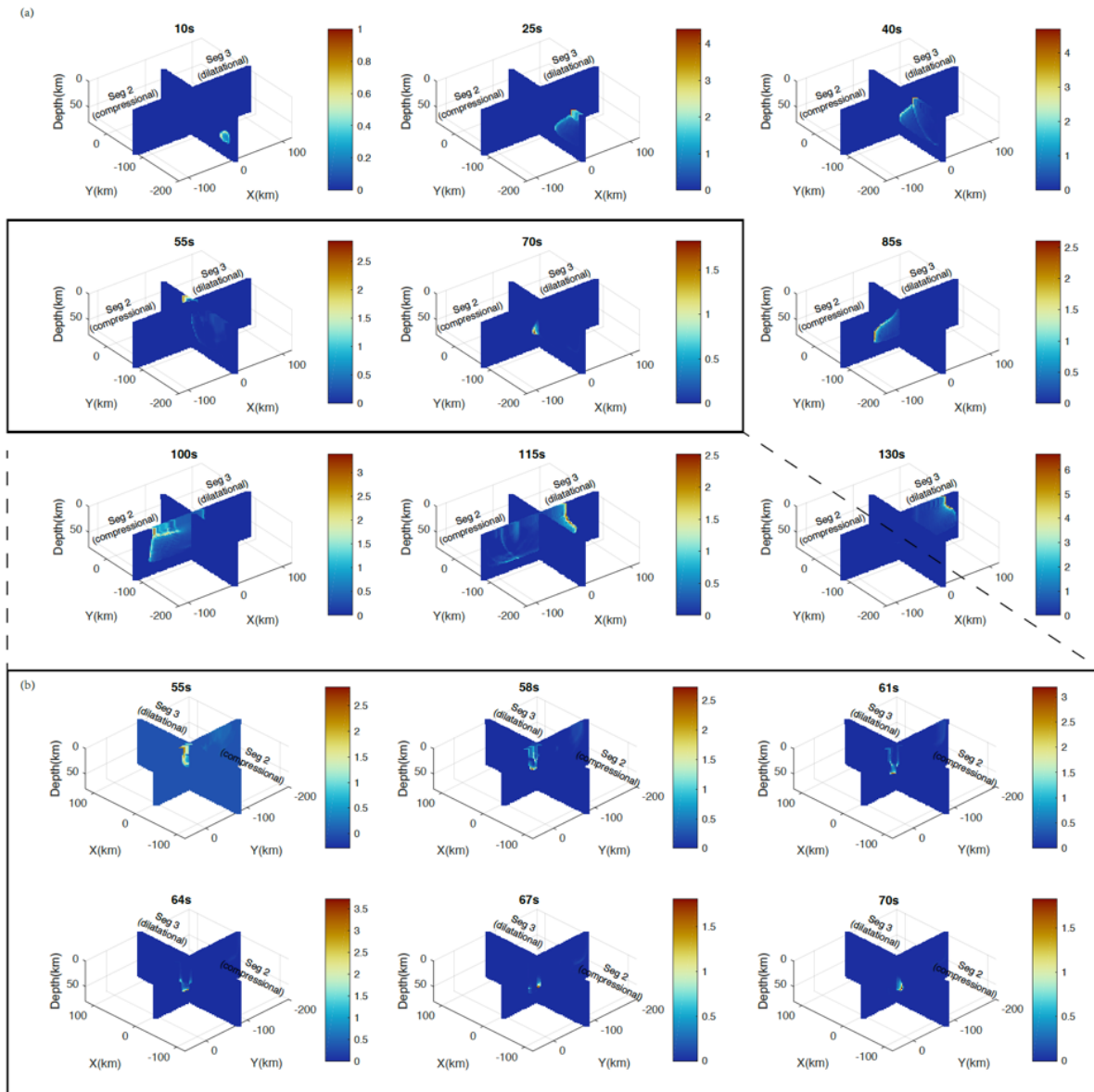
Figure 6.10: The rupture process for the sequence in 6382 yr for Test 2. (a) The slip rate at different time steps. (b) is the slip rate with finer step between 55 and 70 s, during which the reflected rupture front triggers the nucleation on the compressional branch.
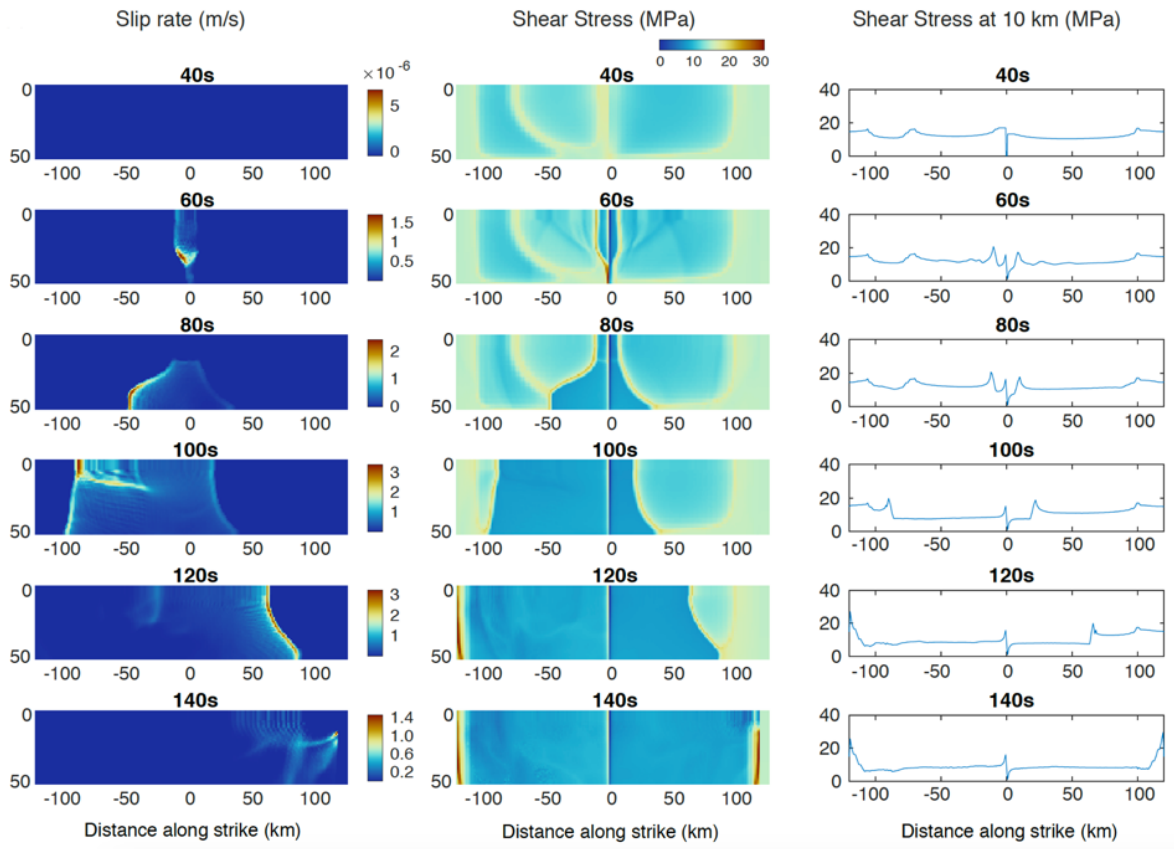
Figure 6.11: The slip rate, shear stress distribution on Fault Plane B and the shear stress profile along the reference line at the depth of 10 km on Fault Plane B at different time steps for the sequence in 6382 yr for Test 2.

111

6.4 Discussion

We reproduce the compressional branching observed during the 2012 off-Sumatra earthquake when we use a frictional coefficient of 0.2 or 0.3 and an heterogeneous initial stress filed generated from earthquake cycle simulation. When the frictional coefficient is 0.2, the compressional branching occurs when the dilatational branch has a lower shear stress due to previous event. When the frictional coefficient is 0.3, the rupture behavior is sensitive to the initial shear stress level, which is related to the slip history. When the shear stress is high, the compressional branching can occur. When the frictional coefficient is 0.4, the rupture propagation on both branches are prohibited. So a low frictional coefficient of 0.2 or 0.3 and the heterogeneous stress field due to irregular rupture behavior provides a possible mechanism to explain the compressional branching of the 2012 off-Sumatra earthquake.

A frictional coefficient of 0.3 is close to the lower bound of the experimental measurement. Hunfeld et al. (2017) performed direct shear experiments at 100 °C, 40 MPa effective normal stress using gouges and found the maximum frictional coefficient is 0.66 (Basal Zechstein) and the minimum is about 0.37 (Ten Boer claystone).

Our earthquake cycle simulation shows that the heterogeneous stress filed with a lower shear stress on the dilatational branch is natural for the orthogonal conjugate fault system. The 4 segments rupture independently even when the faults are planar, which is due to the effect of the intersections and the gaps. In the simulation, the branching behavior is sensitive to the details of the geometry near the intersection. We make small changes to geometry 1 (Fig. 6.2) and run earthquake cycle simulations with the same parameters as Test 1. The changes are either making one or two fault planes continuous, or removing fault segment 4. Our results show that segment 2 and 3 rupture independently only when we use geometry 1 and geometry 7. For geometries 3, 4, 5 and 6, where Fault Plane B is continuous, the earthquake cycle simulation results show peak slip around the intersection, possibly due to stress concentration. For geometry 2, even though Fault Plane 2 is not continuous,

the behavior of two branches are consistent. In nature, the fault is more complicated. The geometries and the heterogeneities of fault properties make the rupture behavior more chaotic.

The interaction between the two fault planes are an important issue. For geometry 3 and 4, the rupture nucleates on fault plane A can propagate to fault plane B occasionally considering only the static stress transfer. In most cases, the behavior of the two faults are independent. But for geometry 2, the two fault planes behave consistently. This may be due to that fault segment 4 does not exists, which favors the rupture propagates to segment 2 and 3 due to stress concentration. For the other geometries, the rupture starting on segment 1 always propagates along fault plane 1 even when a gap exists. Lozos (2022) conduct earthquake dynamic simulations on orthogonal strike-slip fault to investigate the coseismic interaction between the two faults. Lozos also shows the effect of the existence of the discontinuity at the intersection and fault segment 4. He found that rupture jumps from one fault to another if they are mutually discontinuous at the junction, regardless of compression or extension. For the case when the rupture nucleates on fault segment 1, his result shows that the dilatations branch rupture first. But the compressional branch finally rupture when the stopping phase reaches and overcome the compressional stress. He compares the rupture behaviors on T-shaped faults (similar to geometry 2 and 5 in the current research, but without the gap) and +-shaped faults (similar to geometry 4 and 7, but the gap is about 400 m) and found that only when the nucleation fault (the fault on which the earthquake nucleates) ends at the intersection (when the nucleation point is located on segment 1 of the T shape fault in our case) or is discontinuous (when the nucleation point is located on segment 1 and 4 on geometry 4 or segment 2 and 3 of geometry 7 in our case), multiple faults will rupture. In other cases, only the nucleation fault ruptures. We also found that the two fault planes behave more consistently on T-shape faults (geometry 2 and 5). But for geometry 4 and 7, we found very few earthquakes rupture multiple faults in a super cycle when the nucleation fault is discountinous, which is contradictory with the conclusion

113

(a) Geometry2

(b) Geometry3

(c) Geometry4
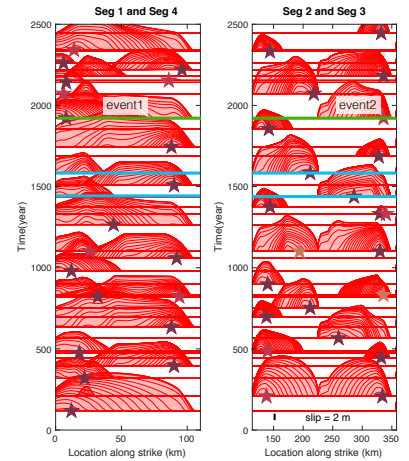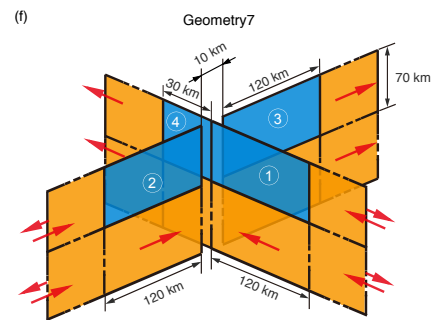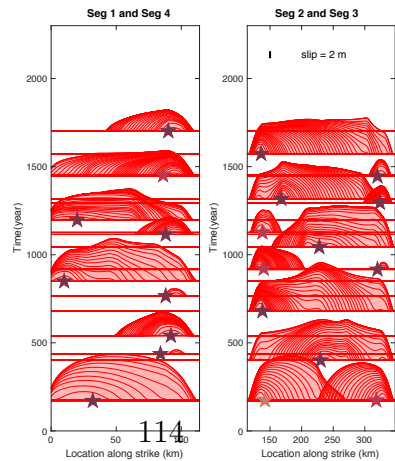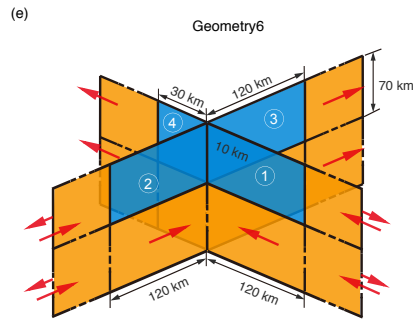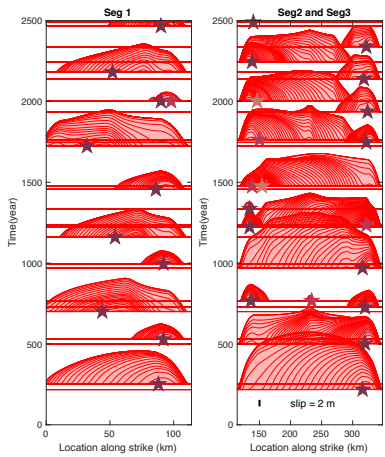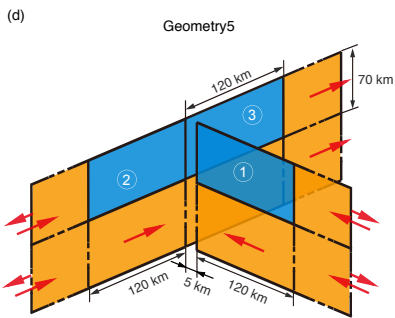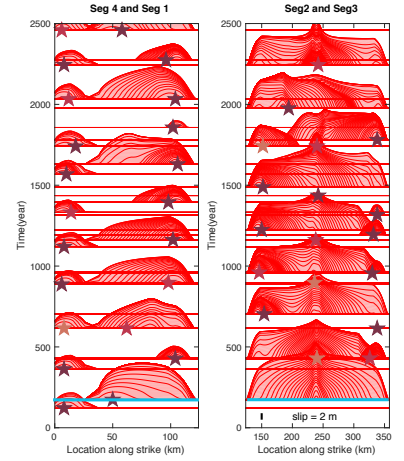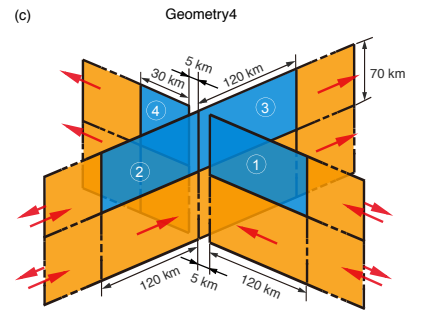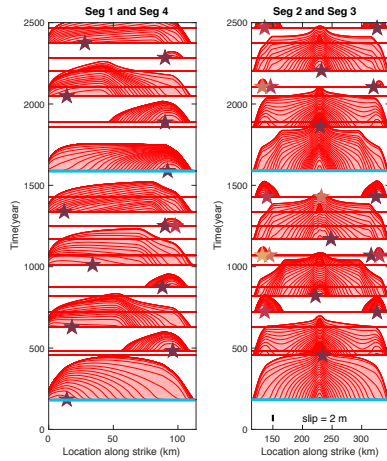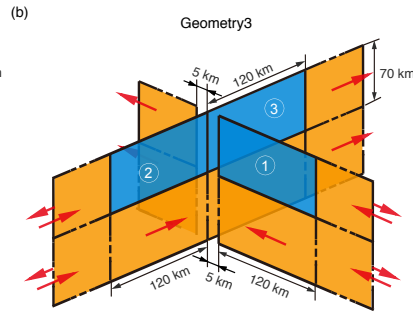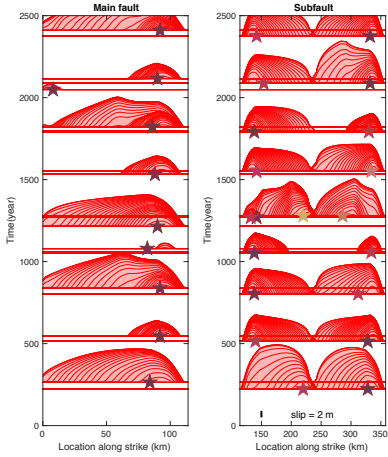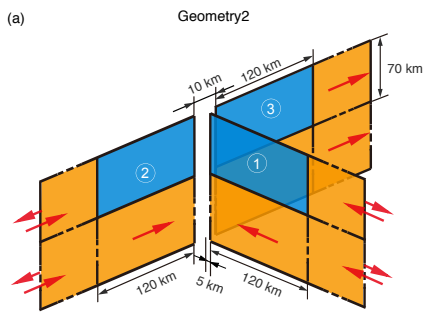
(d) Geometry5

(e) Geometry6

(f) Geometry7

114

(caption of Fig. 6.12)Earthquake cycle simulations with different fault geometries. The upper figure in each panel is the fault geometry for earthquake cycle modeling. The blue regions are the locked zone and the orange regions are stable slipping patches. The lower figure is the spatial and temporal distribution of slip on the fault system. The two panels are corresponding to the two fault planes. The horizontal axis is distance along the fault strike direction and the vertical axis is the time in years. The horizontal line for each event denotes both the time of the event and the zero value of slip. The color filled curves show the slip distribution in each event with a scale bar given on each panel.

made by Lozos (2022). This is probably due to (1) the gap around the intersection in our research is 5 km, which is much larger than that of Lozos (400 m); (2) We did not consider dynamic effect when running earthquake cycle simulations for geometry 2 to 7. Lozos also found that another requirement for the rupture of multiple faults is that the direction of the maximum shear stress is close to 45 degrees from either faults. This is consistent with the observation and theoretical work about the mechanism of the generation of the orthogonal faults due to deep ductile shear localization (Liang, Ampuero, & Pino Muñoz, 2020).

The 2019 Ridgecrest earthquake sequence also occurred on a near-orthogonal strike-slip fault system. The first Mw 6.4 ruptured two orthogonal faults and the Mw 7.1 earthquake nucleated on a positive Coulomb stress region with a delay of about one day, which is similar to the 2 episodes of delayed rupture (one is 2-hr and another is about 15 s) in the dilatational quadrant in the 2012 off-Sumatra earthquake. The delayed earthquake triggering is also reproduced by the earthquake cycle simulation in our research. The earthquake sequence around 1921 yr (highlighted in Fig. 6.12(f)) using geometry 7 shows that the first event starts from segment 4 and propagates to segment 1, without propagating to Fault Plane B. But the first event then triggered the rupture on segment 3 with a delay of 432 days. Fig. 6.13 shows that event 1 increases the shear stress on the nucleation point of event 2 by 4.65e-2 MPa and increase the normal stress by 4e-4 MPa. The shear stress change is much smaller than the static stress triggering threshold. But a slow slip starts immediately after event 1 around the

115

transition zone (Fig. 6.13(c)), where the shear stress concentrates during the interseismic period. The slow slip region finally accelerates to event 2 after 432 days. The slow slip in deep region is considered as one of the possible mechanisms for the delayed triggering of the Mw 7.1 Ridgecrest earthquake based on the analysis of the foreshocks (H. Huang et al., 2020). The effect of pore fluid pressure is another candidate to explain the delayed rupture in the dilatational quadrant for the 2012 off-Sumatra earthquake and the 2019 Ridgecrest earthquake. The fluid buffers the decrease of normal stress on the dilatational branch so that its strength does not decrease immediately. But after the pore fluid pressure diffuses, the pore pressure increases soon and the effectively normal stress decrease, which triggers the slip. Similarly, the high fluid pressure buffers the immediate increase of the effective normal stress on the compressional branch, resulting in an apparent low frictional.

6.5 Conclusion

We propose a possible mechanism to explain the compressional branching during the 2012 off-Sumatra earthquake and reproduce the compressional branching using earthquake simulation with two conditions (a) relatively low pre-stress on dilatational branch and (b) a frictional coefficient no larger than 0.3. We conduct earthquake cycle simulations and dynamic simulations to show that the near-orthogonal conjugate fault system naturally produces uneven stress filed, which provides cases when the shear stress on the dilatational branch is low due to previous event. A frictional coefficient of 0.3 is close to the lower bound of the experimental measurement. We observe delayed triggered earthquake nucleation on the positive Coulomb stress region. The triggering is due to slow slip and static stress transfer and is consistent with the observation of the 2019 Ridgecrest earthquake sequence.
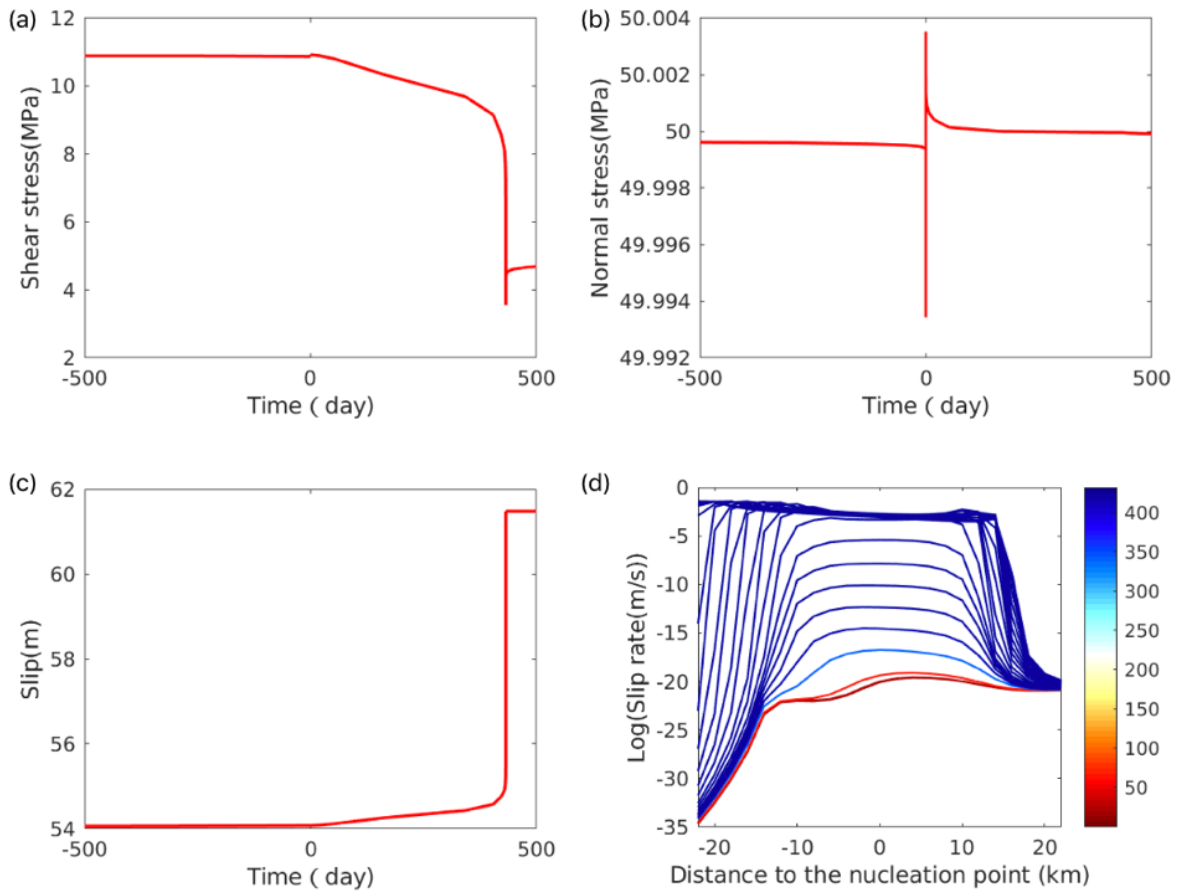
Figure 6.13: The delayed triggering of the nucleation on the dilatational fault by a triggered slow slip. (a) (b) (c) The histories of the shear stress, normal stress and slip on the nucleation point of the triggered event (event 2 highlighted in Fig. 6.12(f)). 0 on the horizontal axis means the origin time of event 1. (d) The distribution of slip rate along strike at the nucleation depth at different times. The color of the lines show the days after event 1.

CHAPTER 7

Adjoint inversion of tsunami source using the S-net system for tsunami early warning

Abstract

Besides using data from seismic arrays on land, we propose to use tsunami recordings to resolve the earthquake and tsunami source for tsunami early warning and earthquake studies. The tsunami recordings potentially provide constraint to resolve more accurate tsunami source, especially for tsunami earthquakes and the cases with triggered submarine landslides, which generate much larger tsunamis than what is expected form the magnitude of the earthquakes. Thus, the tsunami source inferred from tsunami recordings provides important complementary information for tsunami warning. But it was difficult to achieve an accurate tsunami source from tsunami recordings for early warning due to the low density of tsunami stations in the near field.

Recently S-net, a wide and dense array of off-shore ocean bottom pressure gauges are built over the major subduction zone of Japan. Using the S-net data, it is possible to constrain the tsunami source within short time period. We explore the potential of the adjoint-state full waveform tsunami inversion method for tsunami early warning using S-net. The adjoint-state inversion method resolves high resolution result with high efficiency. Compared to finite-fault tsunami source inversions, the method we use does not require as densely gridded Green's functions to obtain a high resolution result, thus reducing computation time. What it does require is a dense instrument network with good azimuthal coverage. The density and

coverage of the S-net pressure gauges fulfill this requirement and reduce the data collection time, thus making it possible to invert the recordings for the tsunami source and issue a timely tsunami warning. We apply our method to synthetic data of a Mw 9.0 earthquake with triggered secondary sources as well as data from the 2016 Off-Fukushima earthquake. The results of the synthetic tests of the Mw 9.0 earthquake show that using the first 5 minutes of the waveforms, the adjoint-state inversion method achieves good performance with an average accuracy of 77%, with the largest error of predicted amplitudes ranging between -5.6 to 1.9 m. The secondary sources are clearly resolved using the first 20 mins of the waveforms. The application to the 2016 Off-Fukushima earthquake shows that the waveforms of the first a few minutes are contaminated with steps due to non-tsunami components such as long-term mechanical drift. However, using the first 25 minutes of the waveforms, the inversion yields a tsunami source that is sufficient for making accurate predictions of arrival times and amplitudes. Assuming a uniformly distributed fault slip, we estimated a stress drop for the latter event to be 4.6 MPa, which is in line with estimations from recent studies.

This is a collaborative work of Saeed Yahya Mohanna, Tong Zhou and me. The manuscript is in preparation. I am the first author to conduct most of the calculations and write the major part of the paper. Saeed's main contribution is to the writing of part of the introduction, method and discussion sections. Tong Zhou mainly provides the ideas including inverting for the coseismic deformation iteratively.

7.1 Introduction

Fast and accurate estimation of tsunami source is essential for tsunami early warning. Compared to the methods of tsunami source estimation based on seismic waves, the methods that utilize tsunami waves are more accurate and are particularly useful in scenarios such as submarine volcanic eruptions and landslides. However, the low density of tsunami stations limit the application of the tsunami observation for tsunami early warning.

After the 2011 Tohoku earthquake, an offshore deep-ocean observation network, S-net (Seafloor Observation Network for Earthquakes and Tsunami) was constructed, which covers the major potential regions of tsunami sources of Japan trench. The high density and large coverage of the S-net pressure gauges shorten the data collecting time, which makes it possible to invert the recordings for the tsunami source and issue a tsunami warning. Several methods based on tsunami recordings have been developed and tested using synthetic waveforms and recordings of S-net pressure gauges (e.g. Aoi et al., 2019; Inoue, Tanioka, & Yamanaka, 2019; Mulia & Satake, 2021; Tanioka, 2020; Tsushima & Yamamoto, 2020; Y. Wang & Satake, 2021; Yamamoto, Aoi, et al., 2016; Yamamoto, Hirata, et al., 2016).

The problem with using traditional finite-fault tsunami source inversion methods is that to attain a high resolution, one needs densely-gridded Green's functions, which is not always possible to implement in the immediate aftermath of a tsunami. Pre-calculated Green's functions can curtail this issue. However, covering a large expanse of the ocean requires a coarse grid or a large amount of spacing within the Green's functions, leading to a heavy computational burden. For example, if we mesh the entire north-eastern Pacific Ocean from the Aleutian Islands to the coast of the State of Washington with a 1 arc-minute spacing, the total number of grids will be about 2000000, which requires several months or even years to calculate the Green's functions with hundreds of CPU cores. On the other hand, the adjoint-state tsunami inversion is suitable for real-time application because it recovers accurate initial water elevation in only a few iterations (Zhou et al., 2019). So, the adjoint-state full-waveform inversion of the tsunami source has two major benefits compared to the traditional finite-fault tsunami source inversion method: high computational efficiency and high resolution. This allows the tsunami source image to be used quickly and directly in forward tsunami simulation, producing accurate forecasts of tsunami height and arrival time.

However, an ideal adjoint state inversion needs dense stations with uniform azimuthal coverage, which makes it difficult to be applied to early warning in most subduction zones. S-net (Fig. 7.1) fits the requirement of the adjoint state inversion method very well and

provides an opportunity to test the performance of the method to be used for early warning. The large coverage and near-equal spacing of the S-net stations guarantees the uniform azimuthal coverage within a short time (within about 15 min). Moreover, the offshore ocean bottom pressure gauges (OBPGs) are preferred for the adjoint state method compared to tide gauges for three main reasons: (1) ocean-bottom pressure gauges do not get affected by wave reflections off the coast as much as tide gauges; (2) wave speeds are not as affected by the resolution of bathymetry data as tide gauges; (3) the nonlinear effect is neglected since the OBPGs are located at large depths.

We give a description of our method in the next section and report the source and pre-processing of our data. Then we report the results of applying our adjoint method to synthetic waveforms of the 2011 Mw 9.0 Tohoku earthquake and recorded tsunami waveforms of the 2016 Mw 6.9 Off-Fukushima earthquake to test whether the adjoint method with S-net can provide a fast and accurate prediction of a tsunami wave for tsunami warnings. We finally discuss our results and their implications.

7.2 Method and workflow of the adjoint-method-based tsunami early warning approach

The adjoint-state tsunami source inversion method we use was developed by Zhou et al. (2019) and is inspired by the full waveform inversion methods in exploration seismology, which take advantage of the rich information embedded in the full wave field. Extensive synthetic tests conducted in exploration geophysics show that the adjoint-state method improves the resolution and balances the spatially unevenly distributed recordings (Virieux & Operto, 2009; Feng & Schuster, 2017; Sun, Xue, Zhu, Fomel, & Nakata, 2016).

The method takes in observed waveforms and performs time-reversal on them to get a starting model that is forward propagated to obtain predicted data. This data is subtracted from the observations to obtain residuals whose misfits are compared to an assigned threshold
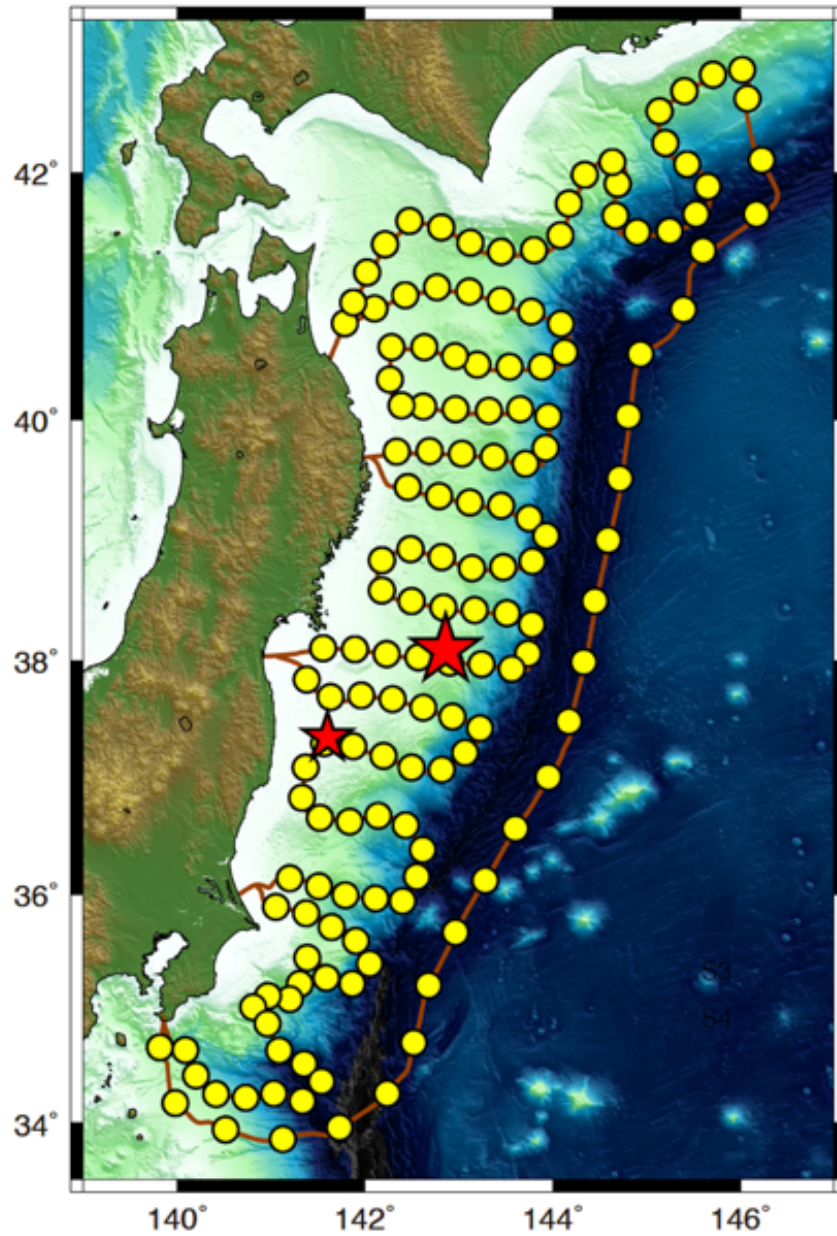
Figure 7.1: Map showing the stations (yellow circles) and the epicenters (red stars) for the synthetic test (large star) and the 2016 off-Fukushima earthquake (smaller star).

value. If the misfit is less than this threshold then the model result is outputted. Otherwise, the residuals are time reversed and then back-propagated again to get the residual wavefield, which is the gradient of the cost function with respect to the model parameters. Then the conjugate direction of the model are calculated and used to update the model vector. The process before back-propagation is then repeated until a suitable model is obtained. This is explained in detail in Zhou et al. (2019).

For the time-reversal and the forward simulations, we use the Parallel Cornell Multi-grid Coupled Tsunami modeling package (PCOMCOT; An et al., 2014, Liu et al., 1998). This package uses finite difference methods to solve the Shallow Water Equations in various coordinate systems. The calculation region (138 °E to 148 °E, 32 °N to 45 °E) is divided into 208,000 grids. We use a calculation grid size of 90 arcseconds, which shortens the calculation time to less than 5 s for 1 forward simulation with 16 CPU cores and yields relatively accurate results in the open sea, which is less sensitive to the bathymetries compared to coastal regions.

7.3 The generating of synthetic waveforms of the 2011 Mw 9.1 Tohoku earthquake

Synthetic tsunami waves are generated at the locations of all currently installed S-net stations. In our first synthetic test, we use a slip model of the 2011 Mw 9.1 Tohoku earthquake (Fig. 7.2) inverted from tsunami waves (Fujii et al., 2011). In the second synthetic test, we add multiple secondary sources representing triggered submarine landslides on the top of the initial water elevation of the first synthetic test. Each secondary source is a square with an amplitude of 20 m and a size of 60 km (Fig. 7.2).
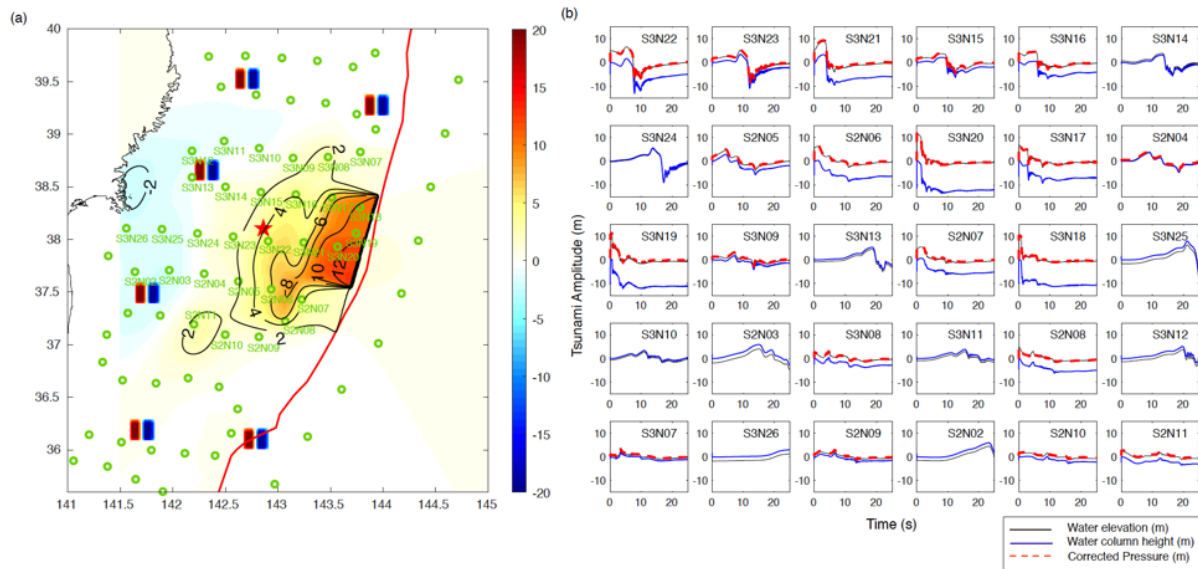
Figure 7.2: The synthetic waveforms of the 2011 Mw 9.1 Tohoku event. (a) The initial water elevation predicted from the slip model of the 2011 Mw 9.0 Tohoku earthquake (Fujii et al., 2011) and the secondary sources. The contours indicate different uplift/subsidence levels due to the Tohoku earthquake. The green circles indicate S-net stations, with the named ones being used in (b). (b) Examples of the waveforms from labeled stations in (a) and the correction for coseismic deformation for the synthetic test without the secondary sources.

7.4 Data preparing

In this study, we applied the adjoint-state inversion method to synthetic data of the 2011 Mw 9.1 Tohoku earthquake and tsunami in addition to S-net data of the 2016 Mw 6.9 Off Fukushima earthquake. These events were chosen because they are located in a region that has had about 10 tsunamis with fatalities of up to about 16000 in the last century and is thus a natural target for tsunami early warning to reduce loss of life.

7.4.1 Station selection

The locations of all currently installed stations that are used for the synthetic test are shown in Fig. 7.1 in addition to the epicenters of the two earthquakes we are studying. The stations located at the outer-rise region were not installed yet in 2016, so we only use 125 stations for the 2016 Mw 6.9 Off Fukushima earthquake.

If using only the close stations, we need a small calculation region which contains only the used station for inversion, which is more efficient. But we find the increasing of stations increases the accuracy of the result a lot, but the cost of the computation does not increase too much. The total calculation time using all of the S-net stations is 1 min and 20 sec using 16 calculation cores. So we choose to use all of the stations, including the stations that only record a small segment of the first peak or trough and the stations that the tsunami waves have not reached. In this way we can examine possible existence of other tsunami sources caused by triggered earthquakes and landslides, which could be far away from the epicenter of the first event. The adjoint-state inversion method is suitable for resolving such secondary sources without increasing too much computational cost. Additionally, for real-time application for early warning, when we only know the epicenter, it is more conservative to consider that the rupture could propagate in all of the directions for 300 km for events like the 2011 Tohoku earthquake. This spatial extent overlaps one third of the whole region covered by S-net stations. For the stations that are not above the source, the waveform

propagates more than 100 km within 10 min along the trench, which could be used to add more constraint to the source. So a station 400 km away from the epicenter should be used. For real-time application, selecting the 'close' stations is subjective and relies on other information including the accuracy of the epicenter, magnitude, rupture direction and slip distribution of an earthquake. We compare the results using only the close stations and all the stations. For the Fukushima earthquake, we found that if using the waveforms of the first 25 min of all of the stations, we could obtain a result that is closer to the result achieved from the waveforms of the first 60 min. So using all of the stations provides more constraints to the source, which could improve the accuracy of the source when the time window is short.

7.4.2 Window selection

We previously proposed to select a window which contains a complete peak and trough so that the artifacts caused by the reflected wave at the tide gauges are avoided (Zhou et al., 2019). We choose to use all of the waveforms (from the origin time to a given point) without selecting a window. This is to account for the automatic application of tsunami early warning. Comparing the results of using selected windows with that of whole waveforms, we found using a selected window does not improve the accuracy of the result. However, for S-net ocean bottom pressure gauges, there are no reflected waves within 15 to 25 min for most of the stations.

7.4.3 Filtering and artifacts removing

One issue with the recordings of S-net ocean bottom pressure gauges is that the initial waveforms of the stations close to the source are contaminated by tsunami-irrelevant steps (Kubota, Saito, & Suzuki, 2020; Kubota et al., 2021; Nakata et al., 2019). These tsunami-irrelevant steps can be caused by tilt due to ground shaking or long-term mechanical drift.

Moreover, the tsunami signal mixes with seismic waves and Earth's tides. In our data processing procedure for the S-net data, the waveform was first low-pass filtered (100 s) to remove the seismic signal following Kubota et al. (2020). Then, the tsunami-irrelevant steps are removed when the time derivative at a particular time was larger than 0.0005 m/s. Finally, a high-pass filter (1000 s) was applied to the data to remove tidal effects. We then perform the correction for the coseismic deformation to get the water elevation from the pressure recordings. This correction is negligible for the Mw 6.9 Off-Fukushima earthquake, possibly because no stations are exactly above the source (this is reasonable since the source is too small) except S2N13, which did not work and showed no recordings of the tsunami waves during the event. The procedure is introduced in detail in the next subsection.

7.4.4   Estimate and add coseismic deformation to the pressure recording

The adjoint-state inversion method uses the result of time reversal imaging as the starting model of the initial water elevation. For conducting time reversal imaging, we need the water elevation incorporating the permanent seafloor deformation and the change of the height of the water column. Given this, we estimated and added the change of water elevation caused by the coseismic deformation to the recording of the pressure gauges for the synthetic test and for the real application. This is essential for the stations that are close to the peak slip regions.

The coseismic deformation can be estimated by calculating the permanent change of equilibrium pressures (Fig. 7.2). When a long enough recording after the earthquake is available, this is not difficult to estimate. However, for warning purposes, we need to estimate the coseismic deformation in a short time (within 5 to 20 min). In this time period, we found it difficult to estimate the coseismic deformation for all of the stations since the arrival time of the tsunami at many stations is 10-25 min, making it challenging to estimate the new equilibrium point for these stations. Luckily, for these stations, the coseismic deformation is relatively small (<2 m) compared to the tsunami height (>5 m). For the stations that
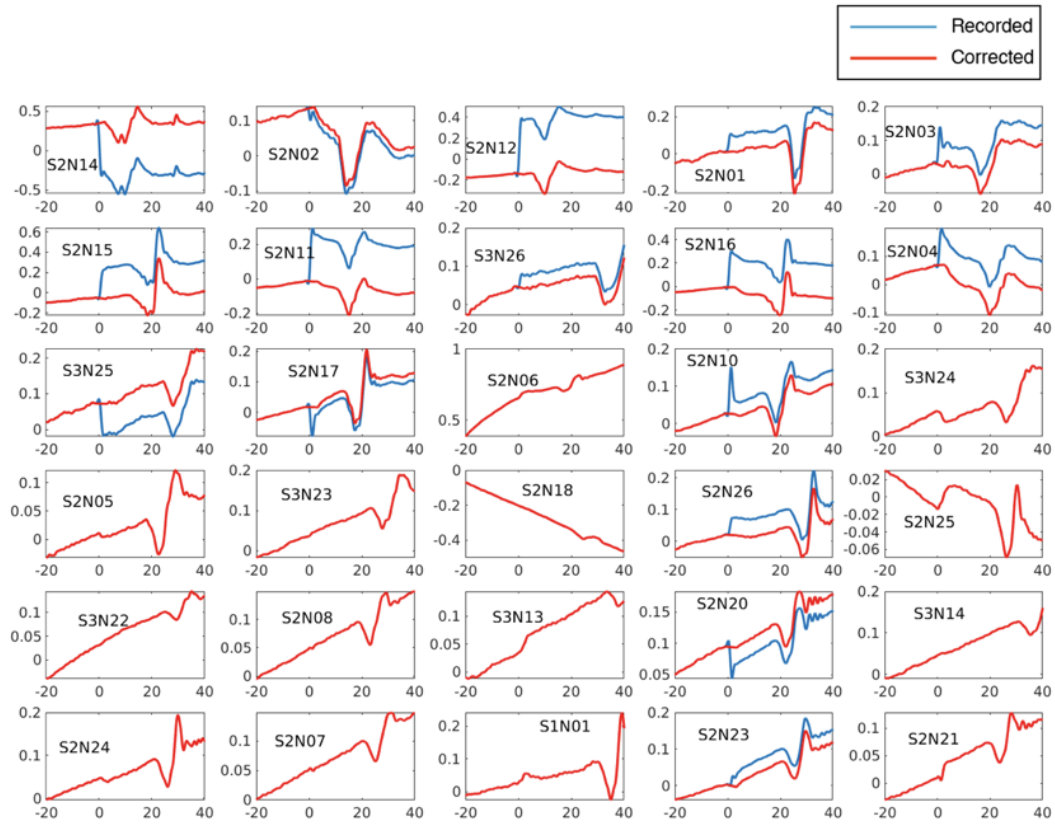
Figure 7.3: Examples of the correction for the tsunami-irrelevant steps. The blue curves are the waveforms after filtering with a passband of >100 s to remove seismic signals. The red lines are the waveform after removing the tsunami-irrelevant steps around the origin time.

are close to the region with large coseismic slip (5 to 10 m) and needing a correction for the coseismic deformation, the water pressure reaches the new equilibrium point relatively quickly (in the first 5 to 10 min). The amplitude of the fluctuation after the waveform reaches the equilibrium point is much smaller compared to the seafloor deformation, so the new equilibrium water elevation can be estimated relatively accurately. As a result, we only estimate the coseismic deformation and add it to the recordings of the pressure data (corresponding to the pressure-related water elevation waveform) for the stations that are 'close' to the peak slip region. We define a station as a 'close' station when its waveforms' peak amplitude in the first 4 min of recording occurs within the first 5 min, when the available waveform is 5 min. We then estimate the equilibrium water elevation by calculating the average recordings of pressure gauges from 4 to 5 min and shift the waveforms so that the new equilibrium water elevation is 0 m. Similarly, if the available waveform is 6 min, we classify a station as a 'close' station when the peak amplitude within the first 6 min is in the first 5 min. We then estimate the ' equilibrium water elevation' by calculating the average recordings of pressure gauges from 5 to 6 min.

The above method is to get the first order approximation of the coseismic deformation, which is used to conduct time reversal imaging to get a starting model of the inversion. We then invert for the coseismic deformation iteratively according to the inversion result of the initial water elevation. We correct the pressure recording and calculate data residual for the next iteration based on the inverted initial water elevation of the last iteration:

$$\delta d_i = d - (d_{obs} + c_{i-1}), \tag{7.1}$$

where δd_i is the data residue at the i th iteration for a station. d is the predicted waveform, which contains the coseismic deformation. d_{obs} is the observed waveform, which does not contain the coseismic deformation. c_{i-1} is the coseismic deformation of the $i-1$ th iteration at the station, which is assumed to be the same as the inverted initial water elevation of the $i-1$ th iteration at the location of this station. c_0 is estimated from the last minute of the

available waveforms, as we introduced. In this way, the initial water elevation, which is also the coseismic deformation, converges iteratively.

7.5   Result

7.5.1   The application to the synthetic test of the 2011 Mw 9.0 Tohoku earthquake

For the synthetic test without the secondary sources, Fig. 7.4 shows that using the waveforms of the first 5 min, we can obtain an accurate tsunami source that is close to the input model after 5 iterations. The amplitude and the pattern of the tsunami source converge quickly in the first 5 iterations and change less from iteration 5 to 50. Fig. 7.10 also shows that the variance reduction and residual change steeply within the first 5 iterations and become nearly constant after 5 iterations. So we propose to use the inversion result after 5 iterations for early warning.

The pattern and amplitudes of the tsunami sources after 5 iterations resolved using waveforms of different lengths (no shorter than 5 min) are very similar, all of which reproduce the input model pretty well. The major difference is that artifacts in the outer trench disapper gradually with the increasing of available time. These artifats are probably caused by the bad azimuthal coverage of stations there. The shape of the source also becomes sharper with longer waveforms. Fig. 7.5 shows the data fitting when the first 5 min waveforms are available.

For the synthetic test with the secondary sources, Fig. 7.6 shows that 4 of 6 secondary sources are clearly resolved when 20 min waveforms are available. The minimum and maximum amplitudes are -16.32 and 16.37 m after 5 iterations, which are relatively accurate compared to the amplitude of the input model, 20 m. The minimum and maximum amplitudes are -14.66 and 12.85 m after 5 iterations using the first 15 min, with only 2 input sources being resolved relatively clearly. The two sources near the trench are not resolved
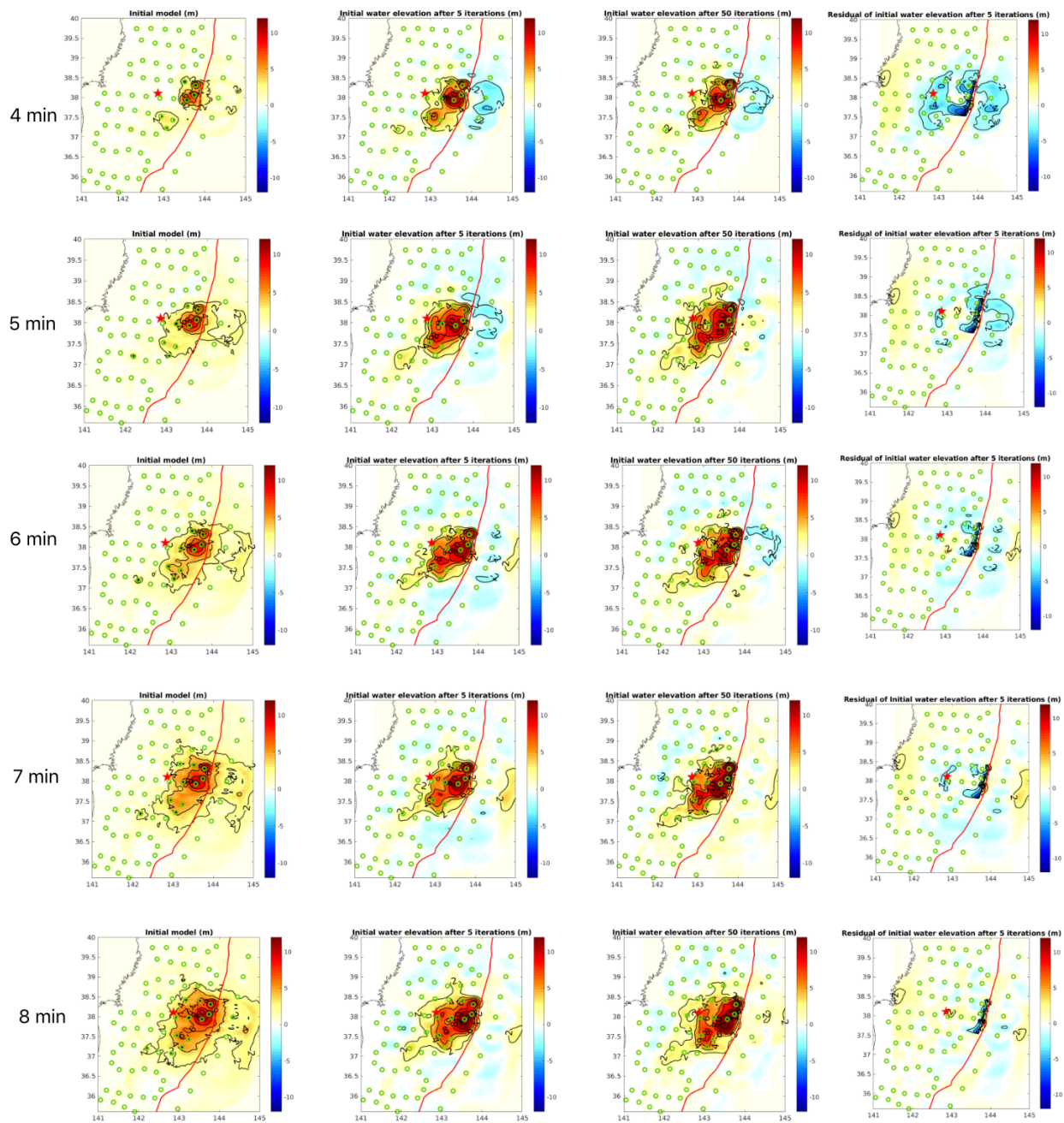
Figure 7.4: The results of the synthetic tests using the stations available within 4, 5, 6, 7 and 8 min from the first row to the fourth row, respectively. The first, second, third and fourth columns are the initial model, the results after 5 iterations, the results after 50 iterations, the misfit between the inverted and input model after 5 iterations.

Figure 7.5: Data fitting of the synthetic tests without secondary sources using available waveforms within 5 min after 5 iterations.

very well even using the first 25 min, possibly due to the reflected effect of the trench, lower station density and bad azimuthal coverage of stations. Fig. 7.7 shows the data fitting when the first 20 min waveforms are available.

7.5.2 The application to the data of the 2016 Mw 6.9 Fukushima earthquake

Fig. 7.8 shows that using the waveforms of the first 15 min, the inversion results of the 2016 Off-Fukushima earthquake show much smaller amplitudes and are very scattered compared to the result when we use longer waveforms. Only three stations contain the first peak if only 15 min is available (Fig. 7.9). Besides, the signals of the three stations are still noisy due to the incomplete removing of the contamination from the step at the closest stations. The data fitting using only the first 15 min is much worse than that of 25 min, where more than 8 stations with complete first peaks with amplitude larger than 0.05 m are available, with less stations affected by the contamination of the step.

It's worth noting that the synthetic test with secondary sources also requires waveforms of the first about 20 minutes to get a clear result (Fig. 7.6). This is different from the synthetic test which only includes the Mw 9.0 Tohoku earthquake, when an accurate result is achieved within 5 min. This is possibly due to the fact that in the application of the synthetic test of the Mw 9.0 Tohoku earthquake, several stations are located above the major slip region. The propagation of the earthquake rupture is faster than tsunami waves. if a station is directly above the rupture zone of the earthquake, the tsunami signal mainly reflects the coseismic displacement. This means that the major pattern of the tsunami source can be constrained by the coseismic deformation recorded by the stations, which can be estimated from the tsunami waves of the first 5 min using our proposed method. However, for a smaller earthquake with magnitude of 6.9, the source size is smaller than 50 km, which is close to the interstation distance of S-net array. As a result, it is reasonable that no stations are just above the peak slip point, as in this case of the Off-Fukushima earthquake. So, we have to wait for the tsunami wave to reach enough stations. Other conclusions of the synthetic
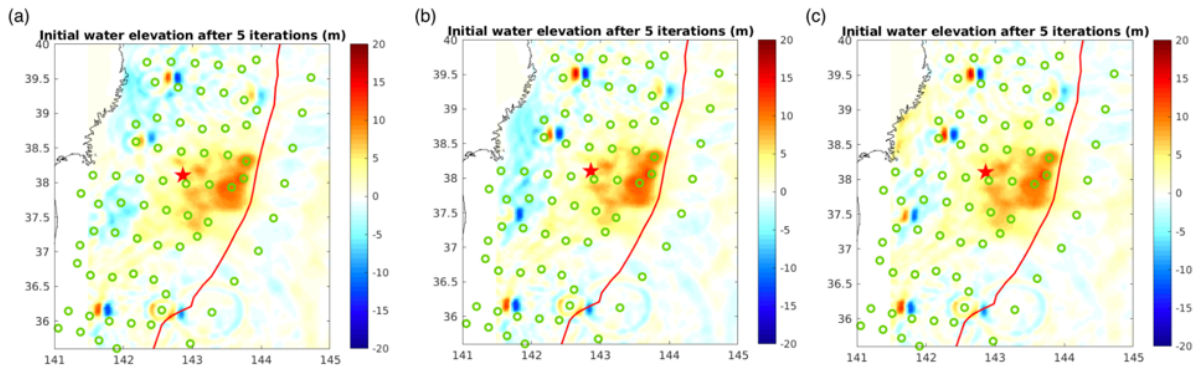
Figure 7.6: The results of the synthetic tests with multiple secondary sources using the stations available within 15 min (a), 20 min (b), and 25 min (c) after 5 iterations.

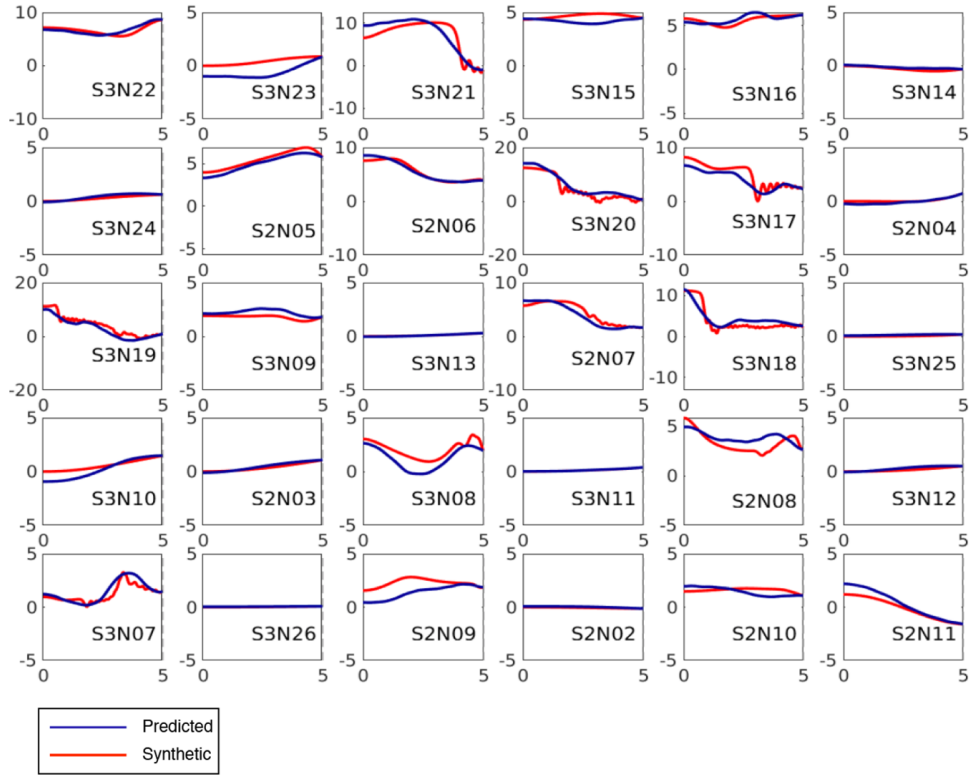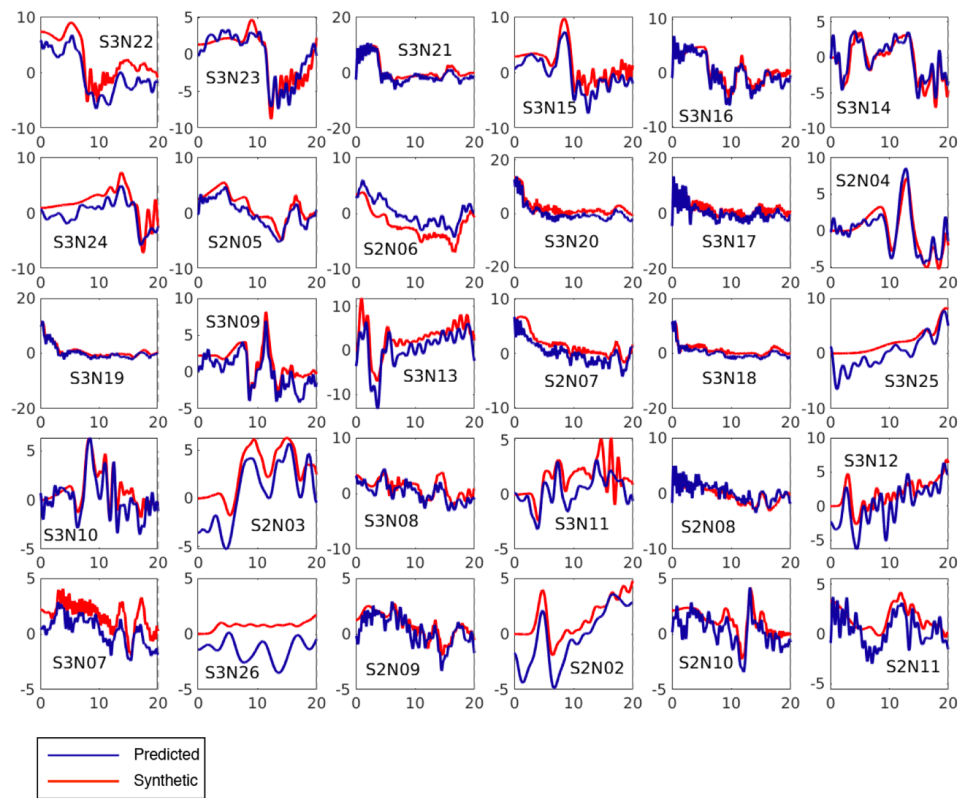Figure 7.7: Data fitting of the synthetic tests with secondary sources using available waveforms within 20 min after 5 iterations.
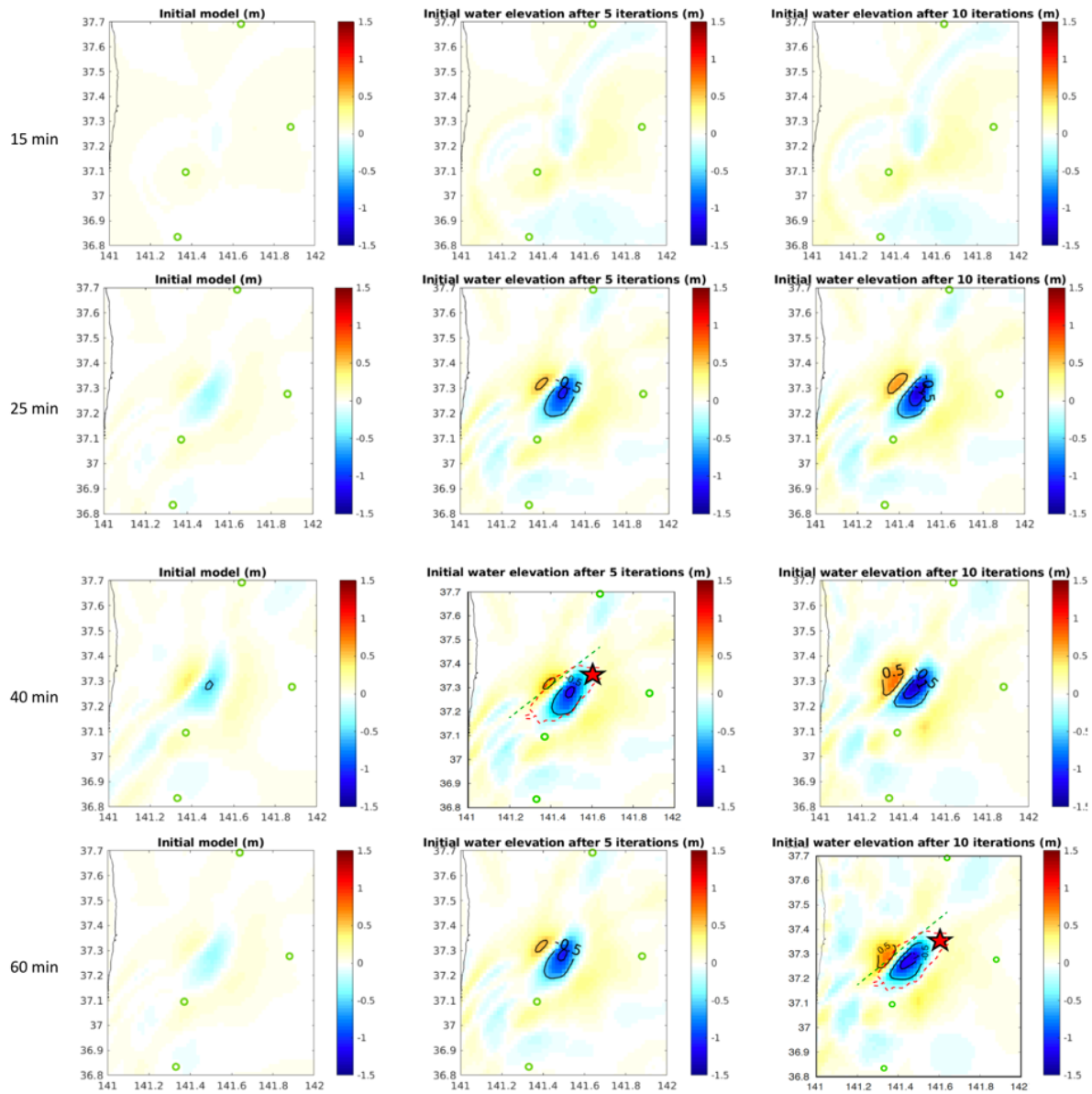
Figure 7.8: The results of the Mw 6.9 Fukushima earthquake using the stations available within 15, 25, 40, and 60 min. The left, middle and right columns are the initial model, the results after 5 and 10 iterations, respectively. The red dashed lines indicate the major subsidence region with amplitude larger than 0.2 m, resolved by Kubota et al. (2021) using S-net data. The green dashed lines indicate the boundary between the subsided and uplifted regions predicted from the finite slip model of JMA inverted from seismic waves.
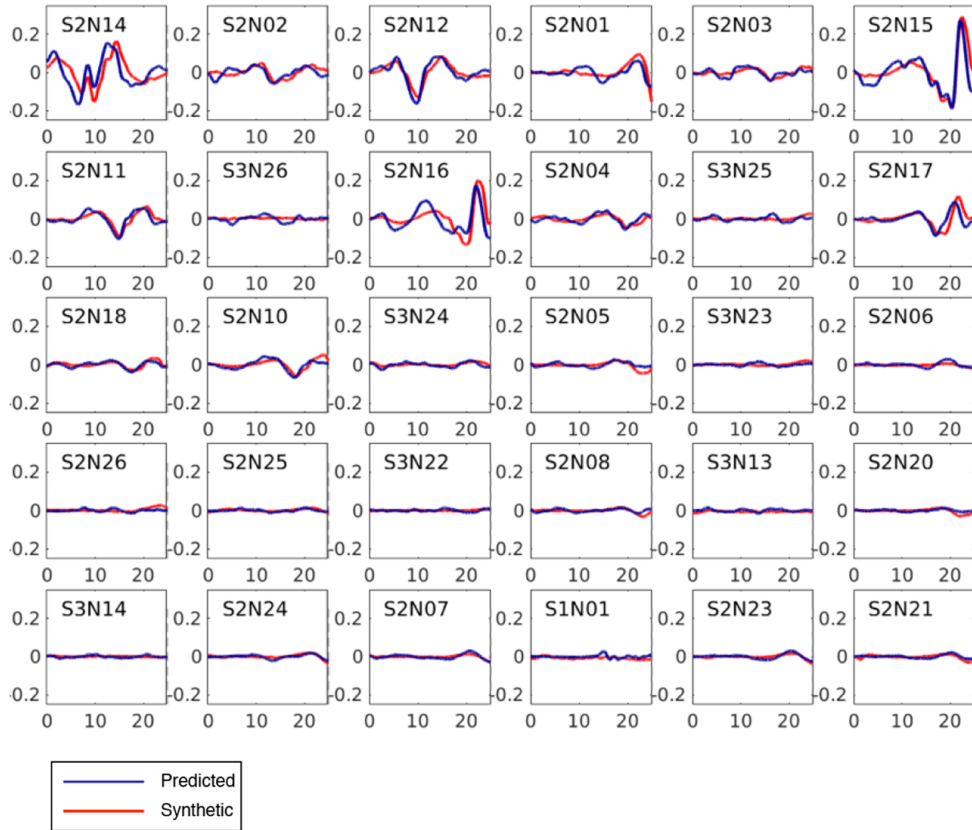
Figure 7.9: Data fitting of Mw 6.9 Fukushima earthquake using available waveforms within 25 min after 5 iterations.

tests are consistent with the application of the 2016 Off-Fukushima earthquake. Namely, the amplitude of the tsunami source increases a lot in the first 5 iterations and converges after 5 iterations. As a result, we used the 5-iteration result as our final one for tsunami warning.

7.6   Discussion

7.6.1   Potential for tsunami early warning

Ideally, the data preparation is automatic and could be done instantly after the data is collected. So the first reliable inversion results can be obtained using the waveforms within the first 25 min for small scaled sources like the M 6.9 Fukushima earthquake and secondary sources (with a size of 60 km) and first 5 min for large earthquake like the Tohoku earthquake. For real-time application, the inversion using the waveforms within 5, 6, 7, 8, 10, 20, 25, and 30 min could be calculated as soon as the data is collected, which yields consistently-updating results that could be integrated into the current tsunami warning system.

The inversion takes about 1 min and 20 s to run using 16 CPU cores (AMD 3990 X @ 2.9 GHz) if we use the waveforms within the first 25 min for all of the S-net stations and stop the inversion after 5 iterations. This time has the potential to be shortened with more cores and GPU. Assuming the final forward simulation that is used to predict the arrival times and amplitudes takes about 40 seconds, the total time for issuing the warning is about 7 min for large earthquakes like the 2011 Mw 9.0 Tohoku earthquake and about 27 min for smaller earthquakes. For extreme events like the 2011 Tohoku earthquake, the first tsunami wave arrival is at about 23 min (Muhari et al., 2012), indicating a lack of a blind zone along the coast. The shortest warning time (the difference between the tsunami wave arrival and the time for issuing the warning) is about 16 min.

To evaluate the accuracy of the predicted waveforms for early warning, we run a forward simulation using the initial water elevation model after 5 iterations, and then compare the predicted and recorded amplitudes and arrival times (the amplitude and time of the first

137

peak) at tide gauges and GPS buoys (Fig. 7.11). The simulation result shows that for the synthetic test, if using the waveforms available within 5 min, the errors of the amplitudes range between –5.55 and 1.93 m. The average accuracy of the amplitude is 77%. If using the waveforms available within 8 min, the average accuracy of the amplitude is 86%. The errors of the amplitudes range between –1.92 and 1.35 m. For the Fukushima earthquake, the errors of the amplitudes range between –0.20 and 0.22 m using the first 25 min waveforms. The errors of the arrival times range between -9.11 and 14.61 min, which are small enough for warning purposes.

7.6.2 Comparison of the Mw 6.9 earthquake result with previous results

The tsunami source distribution of the Mw 6.9 Fukushima earthquake (using the waveforms of the first 60 min, after 10 iterations) shows a major subsidence region with a peak of about 1.3 m and a region of uplift with a peak of about 0.65 m. The location and range of the subsidence is consistent with the initial water elevation inferred from S-net data by Kubota et al. (2021), which resolves the subsidence region with a peak of about 2.0 m. The region of uplift is not clear in Kubota et al. (2021)'s result. However, the finite fault slip model (JMA) inverted from seismic waves shows a region of uplift. The sharp boundary between the subsidence region (with a peak of about 2.4 m) and an uplifted region (with a peak of about 0.5 m) is very close to the location and strike of the boundary between the subsidence and uplifting regions resolved by our method (Fig. 7.8).

7.6.3 Inversion for source parameters of the Mw 6.9 earthquake

Assuming a fault with uniform slip distribution, we searched for the fault parameters based on the initial water elevation achieved using 60 min waveforms after 10 iterations. We performed a grid search for 5 parameters: the longitude, latitude and the depth of the center of the fault, the slip, and the fault width. The best fitting model is located at 141.537 E,

37.243 N, with a centroid depth of 8 km. The average slip for a model at this location is 2 m, with a width of 12 km (Fig. 7.12).

The fault length was then estimated to be 23 km given a moment of 2.484e19 N.m and a rigidity of 30 GPa. With these parameters, the stress drop was estimated to be 4.6 MPa using:

$$\Delta\sigma = c\frac{M_0}{(LW)^{1.5}}, \tag{7.2}$$

where $\Delta\sigma$ is the stress drop, c is a constant ($=8/3pi$, when Poisson's ratio is 0.25)(Kanamori & Anderson, 1975). Our estimation of the stress drop is very close to Kubota et al. (2021)'s estimation of 4.2 MPa. According to Kubota et al. (2021), the shear stress change caused by the 2011 Tohoku earthquake at the epicenter of the 2016 Fukushima event is about 2 MPa, which is much smaller than the stress drop of the 2016 Fukushima event, which is a normal faulting event. Thus, our estimation confirms Kubota's conclusion that the extensional stress was concentrated in the shallow region of the crust near the 2016 Fukushima event prior to the 2011 Tohoku earthquake. This is possibly related to the bending of the overriding plate (Kubota et al., 2021).

7.7   Conclusion

In this study, we evaluated the potential of the application of the adjoint-state full waveform tsunami inversion method for tsunami early warning using S-net. We use an algorithm to remove the tsunami-irrelevant signal at ocean-bottom pressure gauge stations and an automatic algorithm to extract and invert for the coseismic deformation for the stations close to the source. We apply this approach to synthetic waveforms of the 2011 Mw 9.0 Tohoku earthquake and the recording of the 2016 Mw 6.9 Fukushima earthquake. Using all of the stations, our result shows that the Mw 6.9 earthquake can be accurately resolved within 27 min and the Mw 9.0 earthquake can be accurately resolved within 7 min. These results

benefit from the fast estimation of the coseismic deformation beneath the closest stations. The predicted waveforms have errors of -2.71 to 2.3 m for amplitude, which is acceptable for early warning purposes.
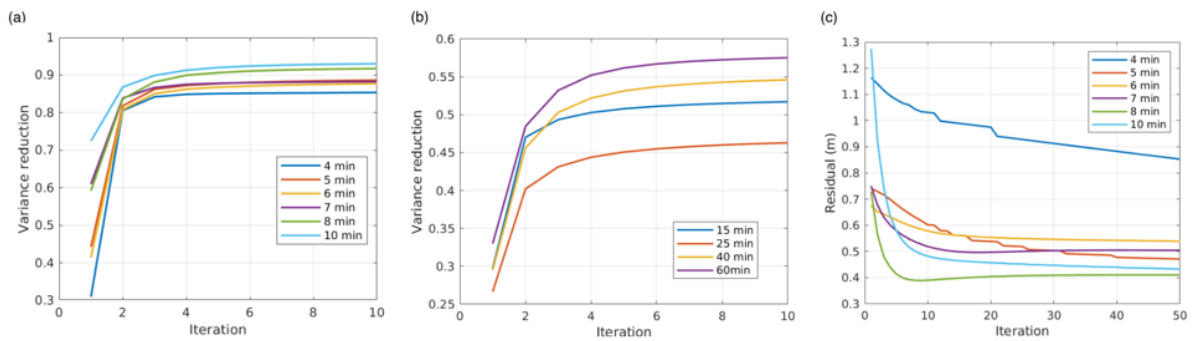
Figure 7.10: The change of variance reduction with each iteration for (a) the synthetic test and (b) the Fukushima earthquake.(c) The change of residual (the model misfit between the inverted and input model).
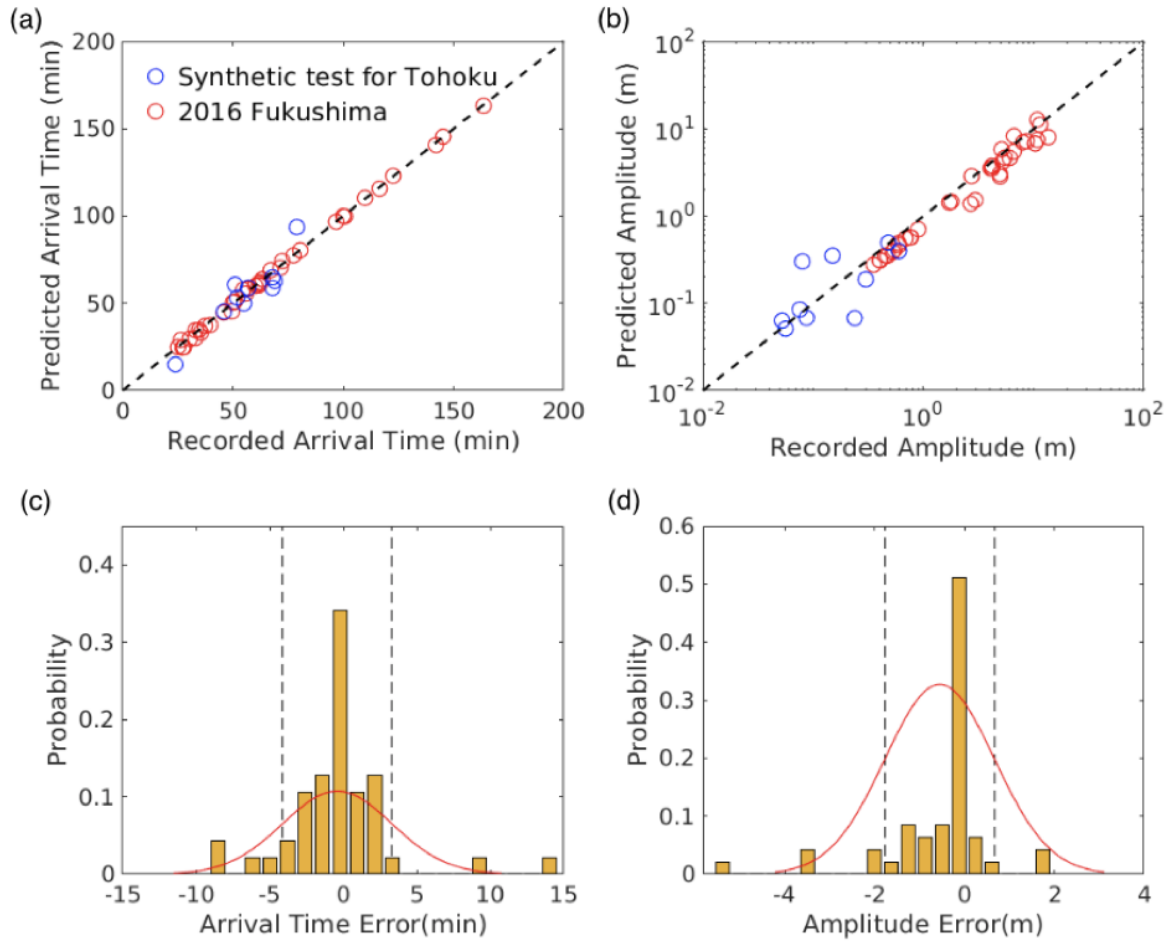
Figure 7.11: The accuracy of the predicted arrival time and amplitudes at tide gauges and GPS buoys. For the synthetic test of the Tohoku earthquake, we use the source model resovled from the first 5 min waveforms. For the Fukushima earthquake, we use the source model resovled from the first 25 min waveforms. (a) Correlation between predicted and recorded arrival times of the first peak for the two applications. (b) Correlation between the predicted and recorded amplitude of the first peak for the two applications. (c) The error distribution of the arrival time. The red curve is the fitted Gaussian distribution. The dashed lines are the standard deviations. (d) The error distribution of the amplitude.
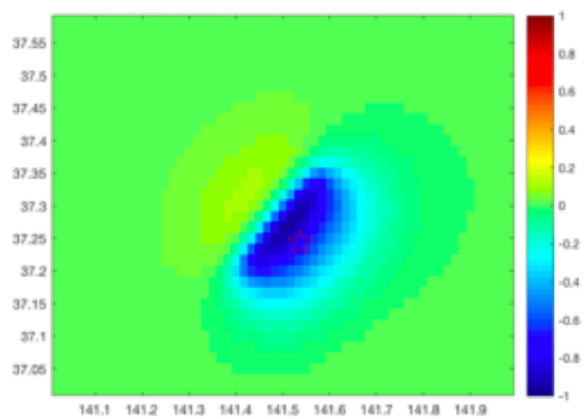
Figure 7.12: The seafloor displacement predicted from the best uniform slip fault model.

CHAPTER 8

Conclusion

The main goal of my research is to develop an improved local back-projection method: MLBP (multiple array local back-projection) to get more accurate source parameters within shorter time. We used a series of strategies and applied the improved method to M 6 to M 9 earthquakes. The combination of multiple sources improve the accuracy and stability of lcoal back-projection result. For the M 8 and 9 earthquakes in Japan, we use low frequency signal (about 0.06 Hz) to characterize the major slip region for forcasting tsunami. We demonstrate that the tsunami warning approach based on this method is potential for the major subduction zone in the world, except for the region with low station density like Sumatra. For the M 6 and 7 Ridgecrest earthquakes, we are using a higher frequency band (about 1 Hz) of a dominant crustal phase, an automatic grouping method based on waveform coherence and an empirical static calibration of the back-aizmuth to get higher reoslution and accuracy. The result shows complicated bilateral rupture on multiple faults for the two earthquakes.

We then apply similar multiple array method to teleseismic arrays and show its ability to improve the 3D spacial resolution and stability of BP result. The application to the 2021 Mw 7.3 East Cape, New Zealand earthquake shows rupture on multiple faults at different depths. The rutpure on the shallow fault is probably triggered by a combined effect of static and dynamic stress.

We also conduct fault simulation to reproduce complicated rutpure process on orthogonal strike-slip fault system, including the delayed triggering of the M 7.1 Rigecrest earthquake

by the M6 event and the compressional branching observed in the 2012 Mw 8.6 off-Sumatra earthquake.

The last project is related to another tsunami warning method based on recordings of arrays of ocean bottom pressure gauges. We show that this method could get accurate result (86% accuracy) within short time (8 min). The triggered secondary sources, which are potential to cause tsunami greater than what is expected from the earthquake magnitude, could be accurately resovled within 20 min.

In the future, we could apply the MLBP method to steeply increasing data, including the DAS (Distributed Acoustic Sensor) data. DAS has potential to be a powerful technology in future research due to its advantages, e.g. high density, low cost and availability in ocean bottom. The growing data and its spatial continuity also provide an opportunity to further improve the MLBP, including the evaluation and mitigation of the waveform incoherence, back-azimuth bias and the effects of multi-phases. The applications of MLBP to these data sets could achieve more source parameters with high resolution. The application of MLBP to DAS arrays is potential for early warning of earthquakes and tsunamis. We can also apply the MLBP method to the seismic signal recorded by S-net, which is potential to be faster than using the hinet and K-Net stations for early warning of tsunami.

Besides, I also want to explore the application of machine learning for imaging large earthquakes using the recording of local seismic stations. The new techniques in the field of machine learning has potential to solve the remaining problems of MLBP automatically, including better algorithms for station grouping, the seperation of multiple phases and the slowness calibration.

Bibliography

Allen, R. M. (2007). The elarms earthquake early warning methodology and application across california. In *Earthquake early warning systems* (pp. 21–43). Springer.

Allen, R. M., & Ziv, A. (2011). Application of real-time gps to earthquake early warning. *Geophysical Research Letters*, *38*(16).

Allmann, B. P., & Shearer, P. M. (2007). A high-frequency secondary event during the 2004 parkfield earthquake. *Science*, *318*(5854), 1279–1283.

An, C., Liu, H., Ren, Z., & Yuan, Y. (2018). Prediction of tsunami waves by uniform slip models. *Journal of Geophysical Research: Oceans*, *123*(11), 8366–8382.

An, C., & Meng, L. (2016). Application of array backprojection to tsunami prediction and early warning. *Geophysical Research Letters*, *43*(8), 3677–3685.

An, C., Sepúlveda, I., & Liu, P. L.-F. (2014). Tsunami source and its validation of the 2014 iquique, chile, earthquake. *Geophysical Research Letters*, *41*(11), 3988–3994.

Aoi, S., Suzuki, W., Chikasada, N. Y., Miyoshi, T., Arikawa, T., & Seki, K. (2019). Development and utilization of real-time tsunami inundation forecast system using s-net data. *Journal of Disaster Research*, *14*(2), 212–224.

Barnhart, W. D., Hayes, G. P., & Gold, R. D. (2019). The july 2019 ridgecrest, california, earthquake sequence: Kinematics of slip and stressing in cross-fault ruptures. *Geophysical Research Letters*, *46*(21), 11859–11867.

Bhat, H. S., Olives, M., Dmowska, R., & Rice, J. R. (2007). Role of fault branches in earthquake rupture dynamics. *Journal of Geophysical Research: Solid Earth*, *112*(B11).

Borcea, L., Papanicolaou, G., Tsogka, C., & Berryman, J. (2002). Imaging and time reversal in random media. *Inverse Problems*, *18*(5), 1247.

Brodsky, E. E. (2006). Long-range triggered earthquakes that continue after the wave train passes. *Geophysical Research Letters*, *33*(15).

Brodsky, E. E., & Prejean, S. G. (2005). New constraints on mechanisms of remotely

triggered seismicity at long valley caldera. *Journal of Geophysical Research: Solid Earth*, *110*(B4).

Center, E. (2013). Southern california earthquake center. *Caltech. Dataset*.

Chen, K., Avouac, J.-P., Aati, S., Milliner, C., Zheng, F., & Shi, C. (2020). Cascading and pulse-like ruptures during the 2019 ridgecrest earthquakes in the eastern california shear zone. *Nature communications*, *11*(1), 1–8.

Chen, Y., Meng, L., Zhang, A., & Wen, L. (2018). Source complexity of the 2015 mw 7.9 bonin earthquake. *Geochemistry, Geophysics, Geosystems*, *19*(7), 2109–2120.

Collot, J.-Y., & Davy, B. (1998). Forearc structures and tectonic regimes at the oblique subduction zone between the hikurangi plateau and the southern kermadec margin. *Journal of Geophysical Research: Solid Earth*, *103*(B1), 623–650.

D'Amico, S., Koper, K. D., Herrmann, R. B., Akinci, A., & Malagnini, L. (2010). Imaging the rupture of the mw 6.3 april 6, 2009 l'aquila, italy earthquake using back-projection of teleseismic p-waves. *Geophysical Research Letters*, *37*(3).

Delescluse, M., & Chamot-Rooke, N. (2007). Instantaneous deformation and kinematics of the india–australia plate. *Geophysical Journal International*, *168*(2), 818–842.

Dieterich, J. H. (1979). Modeling of rock friction: 1. experimental results and constitutive equations. *Journal of Geophysical Research: Solid Earth*, *84*(B5), 2161–2168.

Doser, D. I., & Webb, T. H. (2003). Source parameters of large historical (1917–1961) earthquakes, north island, new zealand. *Geophysical journal international*, *152*(3), 795–832.

Duan, B. (2012). Dynamic rupture of the 2011 mw 9.0 tohoku-oki earthquake: Roles of a possible subducting seamount. *Journal of Geophysical Research: Solid Earth*, *117*(B5).

Duan, B., Liu, Z., & Elliott, A. J. (2019). Multicycle dynamics of the aksay bend along the altyn tagh fault in northwest china: 2. the realistically complex fault geometry. *Tectonics*, *38*(3), 1120–1137.

Duan, B., & Oglesby, D. D. (2007). Nonuniform prestress from prior earthquakes and the effect on dynamics of branched fault systems. *Journal of Geophysical Research: Solid Earth*, *112*(B5).

Duba, A. G., Durham, W. B., Heard, H. C., Handin, J., & Wang, H. (1990). *The brittle-ductile transition in rocks: The heard volume.* American Geophysical Union.

Duputel, Z., Kanamori, H., Tsai, V. C., Rivera, L., Meng, L., Ampuero, J.-P., & Stock, J. M. (2012). The 2012 sumatra great earthquake sequence. *Earth and Planetary Science Letters*, *351*, 247–257.

Dziewonski, A. M., Chou, T.-A., & Woodhouse, J. H. (1981). Determination of earthquake source parameters from waveform data for studies of global and regional seismicity. *Journal of Geophysical Research: Solid Earth*, *86*(B4), 2825–2852.

Eberhart-Phillips, D., & Bannister, S. (2015). 3-d imaging of the northern hikurangi subduction zone, new zealand: variations in subducted sediment, slab fluids and slow slip. *Geophysical Journal International*, *201*(2), 838–855.

Ekström, G., Nettles, M., & Dziewoński, A. (2012). The global cmt project 2004–2010: Centroid-moment tensors for 13,017 earthquakes. *Physics of the Earth and Planetary Interiors*, *200*, 1–9.

Evangelidis, C., & Kao, H. (2014). High-frequency source imaging of the 2011 october 23 van (eastern turkey) earthquake by backprojection of strong motion waveforms. *Geophysical Journal International*, *196*(2), 1060–1072.

Faccenda, M., Gerya, T. V., & Burlini, L. (2009). Deep slab hydration induced by bending-related variations in tectonic pressure. *Nature Geoscience*, *2*(11), 790–793.

Fan, W., de Groot-Hedlin, C. D., Hedlin, M. A., & Ma, Z. (2018). Using surface waves recorded by a large mesh of three-element arrays to detect and locate disparate seismic sources. *Geophysical Journal International*, *215*(2), 942–958.

Feng, Z., & Schuster, G. T. (2017). Elastic least-squares reverse time migration. *Geophysics*, *82*(2), S143–S157.

Fillerup, M. A., Knapp, J. H., Knapp, C. C., & Raileanu, V. (2010). Mantle earthquakes in the absence of subduction? continental delamination in the romanian carpathians. *Lithosphere*, *2*(5), 333–340.

Fletcher, J. B., Spudich, P., & Baker, L. M. (2006). Rupture propagation of the 2004 parkfield, california, earthquake from observations at the upsar. *Bulletin of the Seismological Society of America*, *96*(4B), S129–S142.

Fletcher, J. B., Spudich, P., & Baker, L. M. (2007). Rupture propagation of the 2004 parkfield, california, earthquake from observations at the upsar array. *Bulletin of the Seismological Society of America*, *97*(1B), 355.

Fliss, S., Bhat, H. S., Dmowska, R., & Rice, J. R. (2005). Fault branching and rupture directivity. *Journal of Geophysical Research: Solid Earth*, *110*(B6).

Frankel, A. (1991). High-frequency spectral falloff of earthquakes, fractal dimension of complex rupture, b value, and the scaling of strength on faults. *Journal of Geophysical Research: Solid Earth*, *96*(B4), 6291–6302.

Fujii, Y., & Satake, K. (2007). Tsunami source of the 2004 sumatra–andaman earthquake inferred from tide gauge and satellite data. *Bulletin of the Seismological Society of America*, *97*(1A), S192–S207.

Fujii, Y., & Satake, K. (2013). Slip distribution and seismic moment of the 2010 and 1960 chilean earthquakes inferred from tsunami waveforms and coastal geodetic data. *Pure and Applied Geophysics*, *170*(9), 1493–1509.

Fujii, Y., Satake, K., Sakai, S., Shinohara, M., & Kanazawa, T. (2011). Tsunami source of the 2011 off the pacific coast of tohoku earthquake. *Earth, planets and space*, *63*(7), 815–820.

Fukahata, Y., Yagi, Y., & Rivera, L. (2014). Theoretical relationship between backprojection imaging and classical linear inverse solutions. *Geophysical Journal International*, *196*(1), 552–559.

Galvez, P., Ampuero, J.-P., Dalguer, L. A., Somala, S. N., & Nissen-Meyer, T. (2014). Dy-

namic earthquake rupture modelled with an unstructured 3-d spectral element method applied to the 2011 m 9 tohoku earthquake. *Geophysical Journal International*, *198*(2), 1222–1240.

Goldberg, D. E., Melgar, D., Sahakian, V., Thomas, A., Xu, X., Crowell, B., & Geng, J. (2020). Complex rupture of an immature fault zone: A simultaneous kinematic model of the 2019 ridgecrest, ca earthquakes. *Geophysical Research Letters*, *47*(3), e2019GL086382.

Hadley, D., & Kanamori, H. (1977). Seismic structure of the transverse ranges, california. *Geological Society of America Bulletin*, *88*(10), 1469–1478.

Halpaap, F., Rondenay, S., Perrin, A., Goes, S., Ottemöller, L., Austrheim, H., . . . Eeken, T. (2019). Earthquakes track subduction fluids from slab source to mantle wedge sink. *Science Advances*, *5*(4), eaav7369.

Hananto, N., Boudarine, A., Carton, H., Singh, S. C., Avianto, P., Dyment, J., . . . others (2018). Evidence of pervasive trans-tensional deformation in the northwestern wharton basin in the 2012 earthquakes rupture area. *Earth and Planetary Science Letters*, *502*, 174–186.

Hayes, G. P., Wald, D. J., & Johnson, R. L. (2012). Slab1. 0: A three-dimensional model of global subduction zone geometries. *Journal of Geophysical Research: Solid Earth*, *117*(B1).

Honda, R., & Aoi, S. (2009). Array back-projection imaging of the 2007 niigataken chuetsu-oki earthquake striking the world's largest nuclear power plant. *Bulletin of the Seismological Society of America*, *99*(1), 141–147.

Honda, R., Aoi, S., Sekiguchi, H., & Fujiwara, H. (2008). Imaging an asperity of the 2003 tokachi-oki earthquake using a dense strong-motion seismograph network. *Geophysical Journal International*, *172*(3), 1104–1116.

Honda, R., Yukutake, Y., Ito, H., Harada, M., Aketagawa, T., Yoshida, A., . . . others (2011). A complex rupture image of the 2011 off the pacific coast of tohoku earthquake revealed

by the meso-net. *Earth, planets and space*, *63*(7), 583–588.

Hoshiba, M., Iwakiri, K., Hayashimoto, N., Shimoyama, T., Hirano, K., Yamada, Y., ... Kikuta, H. (2011). Outline of the 2011 off the pacific coast of tohoku earthquake (mw 9.0)—earthquake early warning and observed seismic intensity—. *Earth, planets and space*, *63*(7), 547–551.

Hoshiba, M., Kamigaichi, O., Saito, M., Tsukada, S., & Hamada, N. (2008). Earthquake early warning starts nationwide in japan. *EOS, Transactions American geophysical union*, *89*(8), 73–74.

Hoshiba, M., & Ozaki, T. (2014). Earthquake early warning and tsunami warning of the japan meteorological agency, and their performance in the 2011 off the pacific coast of tohoku earthquake (mw9.0). In *Early warning for geological disasters* (pp. 1–28). Springer.

Huang, H., Meng, L., Bürgmann, R., Wang, W., & Wang, K. (2020). Spatio-temporal foreshock evolution of the 2019 m 6.4 and m 7.1 ridgecrest, california earthquakes. *Earth and Planetary Science Letters*, *551*, 116582.

Huang, Y., Meng, L., & Ampuero, J.-P. (2012). A dynamic model of the frequency-dependent rupture process of the 2011 tohoku-oki earthquake. *Earth, planets and space*, *64*(12), 1061–1066.

Hunfeld, L., Niemeijer, A., & Spiers, C. (2017). Frictional properties of simulated fault gouges from the seismogenic groningen gas field under in situ p–t-chemical conditions. *Journal of Geophysical Research: Solid Earth*, *122*(11), 8969–8989.

Ide, S., Baltay, A., & Beroza, G. C. (2011). Shallow dynamic overshoot and energetic deep rupture in the 2011 m w 9.0 tohoku-oki earthquake. *Science*, *332*(6036), 1426–1429.

Inoue, M., Tanioka, Y., & Yamanaka, Y. (2019). Method for near-real time estimation of tsunami sources using ocean bottom pressure sensor network (s-net). *Geosciences*, *9*(7), 310.

Ishii, M. (2011). High-frequency rupture properties of the mw 9.0 off the pacific coast of

tohoku earthquake. *Earth, planets and space*, *63*(7), 609–614.

Ishii, M., Shearer, P. M., Houston, H., & Vidale, J. E. (2005). Extent, duration and speed of the 2004 sumatra–andaman earthquake imaged by the hi-net array. *Nature*, *435*(7044), 933–936.

Ishii, M., Shearer, P. M., Houston, H., & Vidale, J. E. (2007). Teleseismic p wave imaging of the 26 december 2004 sumatra-andaman and 28 march 2005 sumatra earthquake ruptures using the hi-net array. *Journal of Geophysical Research: Solid Earth*, *112*(B11).

Jaeger, J. C., Cook, N. G., & Zimmerman, R. (2009). *Fundamentals of rock mechanics*. John Wiley & Sons.

Jia, Z., Wang, X., & Zhan, Z. (2020). Multifault models of the 2019 ridgecrest sequence highlight complementary slip and fault junction instability. *Geophysical Research Letters*, *47*(17), e2020GL089802.

Jin, Z., & Fialko, Y. (2020). Finite slip models of the 2019 ridgecrest earthquake sequence constrained by space geodetic data and aftershock locations. *Bulletin of the Seismological Society of America*, *110*(4), 1660–1679.

Johnson, J. M., & Satake, K. (1999). Asperity distribution of the 1952 great kamchatka earthquake and its relation to future earthquake potential in kamchatka. In *Seismogenic and tsunamigenic processes in shallow subduction zones* (pp. 541–553). Springer.

Johnson, J. M., Satake, K., Holdahl, S. R., & Sauber, J. (1996). The 1964 prince william sound earthquake: Joint inversion of tsunami and geodetic data. *Journal of Geophysical Research: Solid Earth*, *101*(B1), 523–532.

Johnson, J. M., Tanioka, Y., Ruff, L. J., Satake, K., Kanamori, H., & Sykes, L. R. (1994). The 1957 great aleutian earthquake. In *Shallow subduction zones: Seismicity, mechanics and seismic potential* (pp. 3–28). Springer.

Kame, N., Rice, J. R., & Dmowska, R. (2003). Effects of prestress state and rupture velocity on dynamic fault branching. *Journal of Geophysical Research: Solid Earth*, *108*(B5).

Kanamori, H., & Anderson, D. L. (1975). Theoretical basis of some empirical relations in

seismology. *Bulletin of the seismological society of America*, *65*(5), 1073–1095.

Kanamori, H., & Rivera, L. (2008). Source inversion ofwphase: speeding up seismic tsunami warning. *Geophysical Journal International*, *175*(1), 222–238.

Kaneko, Y., Ito, Y., Chow, B., Wallace, L. M., Tape, C., Grapenthin, R., ... Hino, R. (2019). Ultra-long duration of seismic ground motion arising from a thick, low-velocity sedimentary wedge. *Journal of Geophysical Research: Solid Earth*, *124*(10), 10347–10359.

Kato, A., & Igarashi, T. (2012). Regional extent of the large coseismic slip zone of the 2011 mw 9.0 tohoku-oki earthquake delineated by on-fault aftershocks. *Geophysical research letters*, *39*(15).

Kato, N., & Yoshida, S. (2011). A shallow strong patch model for the 2011 great tohoku-oki earthquake: A numerical simulation. *Geophysical Research Letters*, *38*(7).

Kelemen, P. B., & Hirth, G. (2007). A periodic shear-heating mechanism for intermediate-depth earthquakes in the mantle. *Nature*, *446*(7137), 787–790.

Kennett, B., & Engdahl, E. (1991). Traveltimes for global earthquake location and phase identification. *Geophysical Journal International*, *105*(2), 429–465.

Kiser, E., & Ishii, M. (2012). The march 11, 2011 tohoku-oki earthquake and cascading failure of the plate interface. *Geophysical Research Letters*, *39*(7).

Kiser, E., Ishii, M., Langmuir, C. H., Shearer, P., & Hirose, H. (2011). Insights into the mechanism of intermediate-depth earthquakes from source properties as imaged by back projection of multiple seismic phases. *Journal of Geophysical Research: Solid Earth*, *116*(B6).

Komatitsch, D., & Tromp, J. (2002). Spectral-element simulations of global seismic wave propagation—i. validation. *Geophysical Journal International*, *149*(2), 390–412.

Koper, K., Hutko, A., & Lay, T. (2011). Along-dip variation of teleseismic short-period radiation from the 11 march 2011 tohoku earthquake (mw 9.0). *Geophysical research letters*, *38*(21).

Kozdon, J. E., Dunham, E. M., & Nordström, J. (2012). Interaction of waves with frictional interfaces using summation-by-parts difference operators: Weak enforcement of nonlinear boundary conditions. *Journal of Scientific Computing*, *50*(2), 341–367.

Kubota, T., Kubo, H., Yoshida, K., Chikasada, N. Y., Suzuki, W., Nakamura, T., & Tsushima, H. (2021). Improving the constraint on the mw 7.1 2016 off-fukushima shallow normal-faulting earthquake with the high azimuthal coverage tsunami data from the s-net wide and dense network: Implication for the stress regime in the tohoku overriding plate. *Journal of Geophysical Research: Solid Earth*, *126*(10), e2021JB022223.

Kubota, T., Saito, T., & Suzuki, W. (2020). Millimeter-scale tsunami detected by a wide and dense observation array in the deep ocean: Fault modeling of an mw 6.0 interplate earthquake off sanriku, ne japan. *Geophysical Research Letters*, *47*(4), e2019GL085842.

Lay, T., Yue, H., Brodsky, E. E., & An, C. (2014). The 1 april 2014 iquique, chile, mw 8.1 earthquake rupture sequence. *Geophysical Research Letters*, *41*(11), 3818–3825.

Liang, C., Ampuero, J.-P., & Pino Muñoz, D. (2020). Deep ductile shear localization facilitates near-orthogonal strike-slip faulting in a thin brittle lithosphere.

Lin, G., Thurber, C. H., Zhang, H., Hauksson, E., Shearer, P. M., Waldhauser, F., . . . Hardebeck, J. (2010). A california statewide three-dimensional seismic velocity model from both absolute and differential times. *Bulletin of the Seismological Society of America*, *100*(1), 225–240.

Lin, J., & Stein, R. S. (2004). Stress triggering in thrust and subduction earthquakes and stress interaction between the southern san andreas and nearby thrust and strike-slip faults. *Journal of Geophysical Research: Solid Earth*, *109*(B2).

Lipson, A., Lipson, S. G., & Lipson, H. (2010). *Optical physics*. Cambridge University Press.

Liu, C., Lay, T., Brodsky, E. E., Dascher-Cousineau, K., & Xiong, X. (2019). Coseismic rupture process of the large 2019 ridgecrest earthquakes from joint inversion of geodetic

and seismological observations. *Geophysical Research Letters*, *46*(21), 11820–11829.

Liu, D., Duan, B., Prush, V. B., Oskin, M. E., & Liu-Zeng, J. (2021). Observation-constrained multicycle dynamic models of the pingding shan earthquake gate along the altyn tagh fault. *Tectonophysics*, *814*, 228948.

Liu, Z., Song, C., Meng, L., Ge, Z., Huang, Q., & Wu, Q. (2017). Utilizing a 3d global p-wave tomography model to improve backprojection imaging: A case study of the 2015 nepal earthquake. *Bulletin of the Seismological Society of America*, *107*(5), 2459–2466.

Lozos, J. (2022). Dynamic rupture modeling of coseismic interactions on orthogonal strike-slip faults. *Geophysical Research Letters*, *49*(5), e2021GL097585.

Luo, Y., & Ampuero, J. (2011). Numerical simulation of tremor migration triggered by slow slip and rapid tremor reversals. In *Agu fall meeting abstracts* (Vol. 2011, pp. S33C–02).

Luo, Y., & Ampuero, J. (2012). Simulation of complex tremor migration patterns. In *Agu fall meeting abstracts* (Vol. 2012, pp. S44B–02).

Ma, S. (2012). A self-consistent mechanism for slow dynamic deformation and tsunami generation for earthquakes in the shallow subduction zone. *Geophysical Research Letters*, *39*(11).

Madariaga, R. (1983). High frequency radiation from dynamic earthquake. *Ann. Geophys*, *1*, 17.

Maercklin, N., Festa, G., Colombelli, S., & Zollo, A. (2012). Twin ruptures grew to build up the giant 2011 tohoku, japan, earthquake. *Scientific reports*, *2*(1), 1–7.

Magen, Y., Ziv, A., Inbal, A., Baer, G., & Hollingsworth, J. (2020). Fault rerupture during the july 2019 ridgecrest earthquake pair from joint slip inversion of insar, optical imagery, and gps. *Bulletin of the Seismological Society of America*, *110*(4), 1627–1643.

Manighetti, I., Campillo, M., Bouley, S., & Cotton, F. (2007). Earthquake scaling, fault segmentation, and structural maturity. *Earth and Planetary Science Letters*, *253*(3-4), 429–438.

Masson, D. (1991). Fault patterns at outer trench walls. *Marine Geophysical Researches*,

$13(3)$, 209–225.

McGuire, J. J., & Beroza, G. C. (2012). A rogue earthquake off sumatra. *Science*, *336*(6085), 1118–1119.

Melgar, D., Allen, R. M., Riquelme, S., Geng, J., Bravo, F., Baez, J. C., ... others (2016). Local tsunami warnings: Perspectives from recent large events. *Geophysical Research Letters*, *43*(3), 1109–1117.

Melgar, D., & Bock, Y. (2013). Near-field tsunami models with rapid earthquake source inversions from land-and ocean-based observations: The potential for forecast and warning. *Journal of Geophysical Research: Solid Earth*, *118*(11), 5939–5955.

Melgar, D., & Bock, Y. (2015). Kinematic earthquake source inversion and tsunami runup prediction with regional geophysical data. *Journal of Geophysical Research: Solid Earth*, *120*(5), 3324–3349.

Meng, L., Allen, R., & Ampuero, J.-P. (2014). Application of seismic array processing to earthquake early warning. *Bulletin of the Seismological Society of America*, *104*(5), 2553–2561.

Meng, L., Ampuero, J.-P., Sladen, A., & Rendon, H. (2012). High-resolution backprojection at regional distance: Application to the haiti m7. 0 earthquake and comparisons with finite source studies. *Journal of Geophysical Research: Solid Earth*, *117*(B4).

Meng, L., Ampuero, J.-P., Stock, J., Duputel, Z., Luo, Y., & Tsai, V. (2012). Earthquake in a maze: Compressional rupture branching during the 2012 m w 8.6 sumatra earthquake. *science*, *337*(6095), 724–726.

Meng, L., Huang, H., Bürgmann, R., Ampuero, J. P., & Strader, A. (2015). Dual megathrust slip behaviors of the 2014 iquique earthquake sequence. *Earth and Planetary Science Letters*, *411*, 177–187.

Meng, L., Huang, H., Xie, Y., Bao, H., & Dominguez, L. A. (2019). Nucleation and kinematic rupture of the 2017 mw 8.2 tehuantepec earthquake. *Geophysical Research Letters*, *46*(7), 3745–3754.

Meng, L., Inbal, A., & Ampuero, J.-P. (2011). A window into the complexity of the dynamic rupture of the 2011 mw 9 tohoku-oki earthquake. *Geophysical Research Letters*, *38*(7).

Meng, L., Zhang, A., & Yagi, Y. (2016). Improving back projection imaging with a novel physics-based aftershock calibration approach: A case study of the 2015 gorkha earthquake. *Geophysical Research Letters*, *43*(2), 628–636.

Mesimeri, M., Zhang, H., & Pankow, K. L. (2021). Backprojection imaging of the 2020 mw 5.5 magna, utah, earthquake using a local dense strong-motion network. *Seismological Research Letters*, *92*(2A), 640–646.

Milliner, C., & Donnellan, A. (2020). Using daily observations from planet labs satellite imagery to separate the surface deformation between the 4 july mw 6.4 foreshock and 5 july mw 7.1 mainshock during the 2019 ridgecrest earthquake sequence. *Seismological Research Letters*, *91*(4), 1986–1997.

Mori, N., Takahashi, T., Yasuda, T., & Yanagisawa, H. (2011). Survey of 2011 tohoku earthquake tsunami inundation and run-up. *Geophysical research letters*, *38*(7).

Muhari, A., Imamura, F., Suppasri, A., & Mas, E. (2012). Tsunami arrival time characteristics of the 2011 east japan tsunami obtained from eyewitness accounts, evidence and numerical simulation. *Journal of Natural Disaster Science*, *34*(1), 91–104.

Mulia, I. E., & Satake, K. (2021). Synthetic analysis of the efficacy of the s-net system in tsunami forecasting. *Earth, Planets and Space*, *73*(1), 1–11.

Murotani, S., Satake, K., & Fujii, Y. (2013). Scaling relations of seismic moment, rupture area, average slip, and asperity size for m~ 9 subduction-zone earthquakes. *Geophysical Research Letters*, *40*(19), 5070–5074.

Nakata, K., Hayashi, Y., Tsushima, H., Fujita, K., Yoshida, Y., & Katsumata, A. (2019). Performance of uniform and heterogeneous slip distributions for the modeling of the november 2016 off fukushima earthquake and tsunami, japan. *Earth, Planets and Space*, *71*(1), 1–12.

NCEDC. (2014). Northern california earthquake data center. uc berkeley seismological

laboratory. dataset.

Oglesby, D. D. (2005). The dynamics of strike-slip step-overs with linking dip-slip faults. *Bulletin of the Seismological Society of America*, *95*(5), 1604–1622.

Okuwaki, R., Hicks, S. P., Craig, T. J., Fan, W., Goes, S., Wright, T. J., & Yagi, Y. (2021). Illuminating a contorted slab with a complex intraslab rupture evolution during the 2021 mw 7.3 east cape, new zealand earthquake. *Geophysical Research Letters*, e2021GL095117.

Oskin, M., & Iriondo, A. (2004). Large-magnitude transient strain accumulation on the blackwater fault, eastern california shear zone. *Geology*, *32*(4), 313–316.

Ozawa, S., Nishimura, T., Suito, H., Kobayashi, T., Tobita, M., & Imakiire, T. (2011). Coseismic and postseismic slip of the 2011 magnitude-9 tohoku-oki earthquake. *Nature*, *475*(7356), 373–376.

Parsons, T. (2005). A hypothesis for delayed dynamic earthquake triggering. *Geophysical Research Letters*, *32*(4).

Peltzer, G., Crampé, F., Hensley, S., & Rosen, P. (2001). Transient strain accumulation and fault interaction in the eastern california shear zone. *Geology*, *29*(11), 975–978.

Perrin, C., Manighetti, I., Ampuero, J.-P., Cappa, F., & Gaudemer, Y. (2016). Location of largest earthquake slip and fast rupture controlled by along-strike change in fault structural maturity due to fault growth. *Journal of Geophysical Research: Solid Earth*, *121*(5), 3666–3685.

Poliakov, A. N., Dmowska, R., & Rice, J. R. (2002). Dynamic shear rupture interactions with fault bends and off-axis secondary faulting. *Journal of Geophysical Research: Solid Earth*, *107*(B11), ESE–6.

Ranero, C. R., Phipps Morgan, J., McIntosh, K., & Reichert, C. (2003). Bending-related faulting and mantle serpentinization at the middle america trench. *Nature*, *425*(6956), 367–373.

Reif, C., Masters, G., Shearer, P., & Laske, G. (2002). Cluster analysis of long-period

waveforms: Implications for global tomography. *EOS, Trans. Am. geophys. Un*, *83*(47), 954.

Romano, F., Piatanesi, A., Lorito, S., & Hirata, K. (2010). Slip distribution of the 2003 tokachi-oki mw 8.1 earthquake from joint inversion of tsunami waveforms and geodetic data. *Journal of Geophysical Research: Solid Earth*, *115*(B11).

Ross, Z. E., Idini, B., Jia, Z., Stephenson, O. L., Zhong, M., Wang, X., . . . others (2019). Hierarchical interlocked orthogonal faulting in the 2019 ridgecrest earthquake sequence. *Science*, *366*(6463), 346–351.

Rost, S., & Thomas, C. (2002). Array seismology: Methods and applications. *Reviews of geophysics*, *40*(3), 2–1.

Roten, D., Miyake, H., & Koketsu, K. (2012). A rayleigh wave back-projection method applied to the 2011 tohoku earthquake. *Geophysical Research Letters*, *39*(2).

Ruina, A. (1983). Slip instability and state variable friction laws. *Journal of Geophysical Research: Solid Earth*, *88*(B12), 10359–10370.

Satake, K., Fujii, Y., Harada, T., & Namegaya, Y. (2013). Time and space distribution of coseismic slip of the 2011 tohoku earthquake as inferred from tsunami waveform data. *Bulletin of the seismological society of America*, *103*(2B), 1473–1492.

Shelly, D. R., Peng, Z., Hill, D. P., & Aiken, C. (2011). Triggered creep as a possible mechanism for delayed dynamic triggering of tremor and earthquakes. *Nature Geoscience*, *4*(6), 384–388.

Shimozono, T., Sato, S., Okayasu, A., Tajima, Y., Fritz, H. M., Liu, H., & Takagawa, T. (2012). Propagation and inundation characteristics of the 2011 tohoku tsunami on the central sanriku coast. *Coastal engineering journal*, *54*(01), 1250004.

Simons, M., Minson, S. E., Sladen, A., Ortega, F., Jiang, J., Owen, S. E., . . . others (2011). The 2011 magnitude 9.0 tohoku-oki earthquake: Mosaicking the megathrust from seconds to centuries. *science*, *332*(6036), 1421–1425.

Singh, S. C., Hananto, N., Qin, Y., Leclerc, F., Avianto, P., Tapponnier, P. E., . . . others

(2017). The discovery of a conjugate system of faults in the wharton basin intraplate deformation zone. *Science Advances*, *3*(1), e1601689.

Somala, S. N., Ampuero, J.-P., & Lapusta, N. (2018). Finite-fault source inversion using adjoint methods in 3-d heterogeneous media. *Geophysical Journal International*, *214*(1), 402–420.

Spudich, P., & Cranswick, E. (1984). Direct observation of rupture propagation during the 1979 imperial valley earthquake using a short baseline accelerometer array. *Bulletin of the Seismological Society of America*, *74*(6), 2083–2114.

Stuart, W. D., & Tullis, T. E. (1995). Fault model for preseismic deformation at parkfield, california. *Journal of Geophysical Research: Solid Earth*, *100*(B12), 24079–24099.

Sun, J., Xue, Z., Zhu, T., Fomel, S., & Nakata, N. (2016). Full-waveform inversion of passive seismic data for sources and velocities. In *Seg technical program expanded abstracts 2016* (pp. 1405–1410). Society of Exploration Geophysicists.

Suppasri, A., Latcharote, P., Bricker, J. D., Leelawat, N., Hayashi, A., Yamashita, K., ... Imamura, F. (2016). Improvement of tsunami countermeasures based on lessons from the 2011 great east japan earthquake and tsunami—situation after five years. *Coastal Engineering Journal*, *58*(4), 1640011–1.

Sylvester, A. (1988). Strike-slip faults: Geological society of america bulle-tin, v. 100. *doi*, *10*, 0016–7606.

Tanioka, Y. (2020). Improvement of near-field tsunami forecasting method using ocean-bottom pressure sensor network (s-net). *Earth, Planets and Space*, *72*(1), 1–10.

Tanioka, Y., Nishimura, Y., Hirakawa, K., Imamura, F., Abe, I., Abe, Y., ... others (2004). Tsunami run-up heights of the 2003 tokachi-oki earthquake. *Earth, planets and space*, *56*(3), 359–365.

Taylor, M., & Yin, A. (2009). Active structures of the himalayan-tibetan orogen and their relationships to earthquake distribution, contemporary strain field, and cenozoic volcanism. *Geosphere*, *5*(3), 199–214.

Tsushima, H., & Yamamoto, T. (2020). *Operational use of tsunami source inversion in near-field tsunami warning by jma [conference presentation]. jpgu-agu joint meeting 2020 virtual, online.*

Virieux, J., & Operto, S. (2009). An overview of full-waveform inversion in exploration geophysics. *Geophysics*, *74*(6), WCC1–WCC26.

Walker, K. T., Ishii, M., & Shearer, P. M. (2005). Rupture details of the 28 march 2005 sumatra mw 8.6 earthquake imaged with teleseismic p waves. *Geophysical Research Letters*, *32*(24).

Wallace, L. M., & Beavan, J. (2010). Diverse slow slip behavior at the hikurangi subduction margin, new zealand. *Journal of Geophysical Research: Solid Earth*, *115*(B12).

Wallace, L. M., Beavan, J., McCaffrey, R., & Darby, D. (2004). Subduction zone coupling and tectonic block rotations in the north island, new zealand. *Journal of Geophysical Research: Solid Earth*, *109*(B12).

Wallace, L. M., Kaneko, Y., Hreinsdóttir, S., Hamling, I., Peng, Z., Bartlow, N., ... Fry, B. (2017). Large-scale dynamic triggering of shallow slow slip enhanced by overlying sedimentary wedge. *Nature Geoscience*, *10*(10), 765–770.

Wan, K., Lin, J., Xia, S., Sun, J., Xu, M., Yang, H., ... Xu, H. (2019). Deep seismic structure across the southernmost mariana trench: Implications for arc rifting and plate hydration. *Journal of Geophysical Research: Solid Earth*, *124*(5), 4710–4727.

Wang, D., Becker, N. C., Walsh, D., Fryer, G. J., Weinstein, S. A., McCreery, C. S., ... others (2012). Real-time forecasting of the april 11, 2012 sumatra tsunami. *Geophysical Research Letters*, *39*(19).

Wang, D., & Mori, J. (2011). Rupture process of the 2011 off the pacific coast of tohoku earthquake (m w 9.0) as imaged with back-projection of teleseismic p-waves. *Earth, planets and space*, *63*(7), 603–607.

Wang, D., Takeuchi, N., Kawakatsu, H., & Mori, J. (2016). Estimating high frequency energy radiation of large earthquakes by image deconvolution back-projection. *Earth*

and *Planetary Science Letters*, *449*, 155–163.

Wang, K., & Bilek, S. L. (2011). Do subducting seamounts generate or stop large earthquakes? *Geology*, *39*(9), 819–822.

Wang, K., Dreger, D. S., Tinti, E., Bürgmann, R., & Taira, T. (2020). Rupture process of the 2019 ridgecrest, california m w 6.4 foreshock and m w 7.1 earthquake constrained by seismic and geodetic data. *Bulletin of the Seismological Society of America*, *110*(4), 1603–1626.

Wang, R. (1999). A simple orthonormalization method for stable and efficient computation of green's functions. *Bulletin of the Seismological Society of America*, *89*(3), 733–741.

Wang, X., & Liu, P. L.-F. (2006). An analysis of 2004 sumatra earthquake fault plane mechanisms and indian ocean tsunami. *Journal of Hydraulic Research*, *44*(2), 147–154.

Wang, X., & Liu, P. L.-F. (2007). Numerical simulations of the 2004 indian ocean tsunamis—coastal effects. *Journal of Earthquake and Tsunami*, *1*(03), 273–297.

Wang, Y., & Satake, K. (2021). Real-time tsunami data assimilation of s-net pressure gauge records during the 2016 fukushima earthquake. *Seismological Society of America*, *92*(4), 2145–2155.

Wei, S., Helmberger, D., & Avouac, J.-P. (2013). Modeling the 2012 wharton basin earthquakes off-sumatra: Complete lithospheric failure. *Journal of Geophysical Research: Solid Earth*, *118*(7), 3592–3609.

Wells, D. L., & Coppersmith, K. J. (1994). New empirical relationships among magnitude, rupture length, rupture width, rupture area, and surface displacement. *Bulletin of the seismological Society of America*, *84*(4), 974–1002.

Xie, Y., Bao, H., & Meng, L. (2021). Source imaging with a multi-array local back-projection and its application to the 2019 mw 6.4 and mw 7.1 ridgecrest earthquakes. *Journal of Geophysical Research: Solid Earth*, *126*(10), e2020JB021396.

Xie, Y., & Meng, L. (2020). A multi-array back-projection approach for tsunami warning.

Geophysical Research Letters, *47*(14), e2019GL085763.

Xu, X., Sandwell, D. T., & Smith-Konter, B. (2020). Coseismic displacements and surface fractures from sentinel-1 insar: 2019 ridgecrest earthquakes. *Seismological Research Letters*, *91*(4), 1979–1985.

Xu, Y., Koper, K. D., Sufri, O., Zhu, L., & Hutko, A. R. (2009). Rupture imaging of the mw 7.9 12 may 2008 wenchuan earthquake from back projection of teleseismic p waves. *Geochemistry, Geophysics, Geosystems*, *10*(4).

Yagi, Y. (2004). Source rupture process of the 2003 tokachi-oki earthquake determined by joint inversion of teleseismic body wave and strong ground motion data. *Earth, planets and space*, *56*(3), 311–316.

Yagi, Y., Nakao, A., & Kasahara, A. (2012). Smooth and rapid slip near the japan trench during the 2011 tohoku-oki earthquake revealed by a hybrid back-projection method. *Earth and Planetary Science Letters*, *355*, 94–101.

Yamamoto, N., Aoi, S., Hirata, K., Suzuki, W., Kunugi, T., & Nakamura, H. (2016). Multi-index method using offshore ocean-bottom pressure data for real-time tsunami forecast. *Earth, Planets and Space*, *68*(1), 1–14.

Yamamoto, N., Hirata, K., Aoi, S., Suzuki, W., Nakamura, H., & Kunugi, T. (2016). Rapid estimation of tsunami source centroid location using a dense offshore observation network. *Geophysical Research Letters*, *43*(9), 4263–4269.

Yamanaka, Y., & Kikuchi, M. (2003). Source process of the recurrent tokachi-oki earthquake on september 26, 2003, inferred from teleseismic body waves. *Earth, Planets and Space*, *55*(12), e21–e24.

Yang, J., Zhu, H., & Lumley, D. (2020). Time-lapse imaging of coseismic ruptures for the 2019 ridgecrest earthquakes using multiazimuth backprojection with regional seismic data and a 3-d crustal velocity model. *Geophysical Research Letters*, *47*(9), e2020GL087181.

Ye, L., Lay, T., Kanamori, H., & Rivera, L. (2016). Rupture characteristics of major

and great (mw 7.0+) megathrust earthquakes from 1990 to 2015: 1. source parameter scaling relationships. *Journal of Geophysical Research: Solid Earth*, *121*(2), 826–844.

Yin, J., & Denolle, M. A. (2019). Relating teleseismic backprojection images to earthquake kinematics. *Geophysical Journal International*, *217*(2), 729–747.

Yong, A., Thompson, E. M., Wald, D. J., Knudsen, K. L., Odum, J. K., Stephenson, W. J., & Haefner, S. (2016). *Compilation of v s30 data for the united states* (Tech. Rep.). US Geological Survey.

Yu, H., Liu, Y., Yang, H., & Ning, J. (2018). Modeling earthquake sequences along the manila subduction zone: Effects of three-dimensional fault geometry. *Tectonophysics*, *733*, 73–84.

Yue, H., Lay, T., & Koper, K. D. (2012). En échelon and orthogonal fault ruptures of the 11 april 2012 great intraplate earthquakes. *Nature*, *490*(7419), 245–249.

Yue, H., Sun, J., Wang, M., Shen, Z., Li, M., Xue, L., ... Lay, T. (2021). The 2019 ridgecrest, california earthquake sequence: Evolution of seismic and aseismic slip on an orthogonal fault system. *Earth and Planetary Science Letters*, *570*, 117066.

Zhao, X., Duputel, Z., & Yao, Z. (2017). Regional w-phase source inversion for moderate to large earthquakes in china and neighboring areas. *Journal of Geophysical Research: Solid Earth*, *122*(12), 10–052.

Zhou, T., Meng, L., Xie, Y., & Han, J. (2019). An adjoint-state full-waveform tsunami source inversion method and its application to the 2014 chile-iquique tsunami event. *Journal of Geophysical Research: Solid Earth*, *124*(7), 6737–6750.

Zhu, W., Allison, K. L., Dunham, E. M., & Yang, Y. (2020). Fault valving and pore pressure evolution in simulations of earthquake sequences and aseismic slip. *Nature communications*, *11*(1), 1–11.